Optical identification of sea-mines - Gated viewing three-dimensional laser radar

Busck, Jens

Publication date:
2005

Document Version
Publisher's PDF, also known as Version of record

Optical identification of sea-mines

Gated viewing three-dimensional laser radar

Ph.-D. Thesis

by

JENS BUSCK

Danish Defence Research Establishment

and

Ørsted•DTU, Technical University of Denmark

2005

Abstract

A gated viewing high accuracy mono-static laser radar has been developed for the purpose of improving the optical underwater sea-mine identification handled by the Navy. In the final stage of the sea-mine detection, classification and identification process the Navy applies a remote operated vehicle for optical identification of the bottom sea-mine. The experimental results of the thesis indicate that replacing the conventional optical video and spotlight system applied by the Navy with the gated viewing two- and three-dimensional laser radar can improve the underwater optical sea-mine identification. The laser radar has also a number of applications on land, for example, face recognition at several hundred meters range.

The main components of the laser radar system are a green pulsed laser and a fast gating intensified CCD camera. The laser radar system innovation is a combination of the short laser pulses (0.5 ns), the high laser pulse repetition rate (32.4 kHz), the fast gating camera (0.2 ns), the short camera delay steps (0.1 ns), the applied optical single mode fiber, and the applied algorithm for three-dimensional imaging. The gated viewing laser radar system configuration is an innovative variation of other gated viewing laser radar systems applying a pulsed laser and a range gated CCD camera, among which the Canadians do not make three-dimensional images, (e.g. [Fournier et al. 1993]), and the Swedes do not apply an optical fiber, (e.g. [Steinvall et al. 2003]), for example. The innovative gated viewing laser radar system configuration provides a previous unseen high accuracy in the three-dimensional non-scanning laser radar images. The high accuracy of the presented three-dimensional images is unprecedented among the existing gated viewing mono-static laser radar systems. Underwater three-dimensional images recorded with the gated viewing three-dimensional laser radar have never been reported. The underwater images of a low contrast target are recorded at 4-5 m range. The presented underwater images compare well with the best of the reported three-dimensional underwater optical images recorded with alternative laser radar techniques, among which the most promising is the streak tube imaging laser radar developed in United States. A variety of gated viewing three-dimensional laser radar experiments are presented, where the gated viewing three-dimensional laser radar performance is tested at short, medium, and long range. The performance is also tested in low contrast conditions in the air and underwater. It is shown that three-dimensional imaging has an advantage over two-dimensional imaging, when the objects have low contrast. Compared to the performance in air the performance underwater is deteriorated by the exponential absorption and scattering.

Two new lines of approach have been taken to improve underwater optical sea-mine identification by digital image enhancement and by knowledge of the optical properties of water. The first approach is taken with a Canadian scattering phase function model and an underwater optical data set. The second approach is to determine the line spread function of water from recorded slit images.

A gated viewing three-dimensional laser radar digital simulation tool has been developed to gain knowledge and deeper insight into the laser radar performance in air and underwater.

Resumé

Et monostatisk laser radarsystem til at optage to- og tredimensionelle billeder med høj afstandsnøjagtighed ved hjælp af "gated viewing" teknikken er udviklet med det formål at forbedre Søværnets muligheder for optisk identifikation af søminer placeret på havbunden. Søværnet anvender en lille, fjernstyret og ubemandet undervandsbåd til optisk identifikation af søminer. Den optiske identifikation af søminen er sidste led i en længere detektions-, klassifikations- og identifikationsproces. De eksperimentelle resultater fremlagt i denne afhandling indikerer, at det nuværende videosystem kan erstattes af det nyudviklede laser radarsystem og dermed forbedre mulighederne for to- og tredimensionel optisk identifikation af søminer og andre objekter. Det nyudviklede laser radarsystem har dog også en række anvendelser i luft, for eksempel ansigtsgenkendelse over flere hundrede meters afstand.

Laser radarsystemets hovedkomponenter består af grøn pulset laser og et forstærket og hurtigt CCD kamera. Det nye ved laser radarsystemet er en kombination af anvendelsen af korte laserpulser (0.5 ns), en høj frekvens af laserpulser (32.4 kHz), det hurtige kamera (0.2 ns), de velkontrollerede og korte trinvise kameraforsinkelser (0.1 ns), den optiske fiber (single mode) og den udviklede algoritme til hurtig tredimensionel billedkonstruktion. Laser radarsystemet er en ny variant af eksisterende laser radar-systemer, der også anvender en pulset laser og et CCD kamera. For eksempel optager canadierne ikke tredimensionelle billeder med deres system, og svenskerne anvender ikke en optisk fiber. Det nyudviklede laser radarsystem har vist sig at kunne optage tredimensionelle billeder med en afstandsnøjagtighed, der ikke er set før blandt monostatiske laser radarsystemer. Tredimensionelle undervandsbilleder optaget med et gated viewing laser radarsystem er ikke rapporteret i litteraturen. I denne afhandling præsenteres tredimensionelle undervandsbilleder af en miniature sømineattrap camoufleret med sand for at give en lav kontrast. Undervandsbillederne er optaget på 4-5 m afstand. Undervandsbillederne kan sammenlignes med de bedste tredimensionelle undervandsbilleder, optaget med alternative laser radarsystemer. Iblandt de alternative laser radarsystemer er amerikanernes "streak tube imaging laser radar" den mest lovende.

I afhandlingen er flere forskellige eksperimenter præsenteret, hvor det nyudviklede laser radarsystems ydeevne er testet på korte, mellem og lange afstande. Ydeevnen er testet både i vand og i luft med objekter med lav kontrast. Det viser sig, at tredimensionel billeddannelse har en fordel frem for todimensionel billeddannelse, når objekterne har lav kontrast. Sammenlignet med ydeevnen i luft er ydeevnen i vand forringet på grund af, at vandet spreder og absorberer laserlyset eksponentielt.

To nye indfaldsvinkler er fremført med henblik på at forbedre undervandsoptisk sømine identifikation ved hjælp af digital billedbehandling og indsigt i vands optiske egenskaber. For det første er der anvendt en canadisk spredningsfunktionsmodel, og for det andet er vandets "line spread function" bestemt ud fra to billeder af en optisk slit optaget i luft og i vand.

Der er udviklet en digital simulation af laser radarsystemet for at få et større indblik i systemets ydeevne i luft og i vand.

Acknowledgements

Thanks to the helpful people at the Danish Defence Research Establishment without whom this thesis would not have been possible. Thanks to Anders Villum Clausen, Stig von Platen, Henrik Fürst, and Joachim Faucon Andersen being creative and helpful with Labview programming, data acquisition and practical solutions. Thanks to the helpful people from DTU-COM for their help with the alignment of the optical fiber. Thanks for the hospitality I met in Canada, thanks to Luc Forand and Madeleine Forand. Thanks to co-supervisors Henning Heiselberg, Mogens Caspersen, Danish Defence Research Establishment, and supervisor Helge B.D. Sørensen, Ørsted•DTU, Technical University of Denmark. Thanks to my fellow sports-divers for good recreation in the times off work. Thanks to my family for their general support.

Preface

The thesis is completed through cooperation with the Danish Defence Research Establishment and Ørsted•DTU, Technical University of Denmark. The project is funded by the Danish Defence Research Establishment for a period of three years. All the underwater three-dimensional images were recorded at the Electro-optical section at the Danish Defence Research Establishment.
The idea behind the thesis is founded in the Danish Navy's need for high resolution underwater images in their search for sea-mines and unexploded ordnance. Initial inspiration is found in the underwater gated viewing optical imaging research at the Defense Research & Development Canada (DRDC). As part of the work three instructive months have been spend with the Defense Research & Development Canada, Quebec, Canada. The field trip to Nova Scotia gave a deep insight, how to carry out comprehensive field trials.

There are four articles included in the thesis:

- J. Busck and H. Heiselberg, "Gated viewing and high-accuracy three-dimensional laser radar", *Appl. Opt.*, **43**, 4705-4710, 2004.

- J. Busck and H. Heiselberg, "High-accuracy 3D laser radar", Proc. SPIE, **5412**, 257-263, 2004.

- J. Busck, "Simulation of gated viewing mono-static three-dimensional laser radar", (submitted to Opt. Eng. Dec. 2004).

- J. F. Andersen, J. Busck, and H. Heiselberg, "Long distance high accuracy 3-D laser radar and person identification", (submitted to SPIE Defense & Security Symposium, Orlando, USA, 2005).

Contents

1 Introduction

After a brief introduction to the Navy's potential use of the gated viewing laser radar in Sec. 1.1, an overview of the underwater optical laser radars is presented in Chap. 2. In Chap. 3 the gated viewing laser radar and the two-dimensional applications is described. The three-dimensional gated viewing high-accuracy laser radar imaging is treated in Chap. 4 with interesting examples of applications in Chap. 5. The trials of underwater gated viewing three-dimensional laser radar imaging are presented in Chap. 6. Three months of oversea work with the scattering phase function model and the underwater optical data set developed and collected by the Defense Research & Development Canada is presented in Chap. 7. Line spread function determination is described in Chap. 8. An introduction to the digital simulation of the gated viewing laser radar is given in Chap.9. The conclusion and summary is given in Chap. 10. The text is supported by four appendices and four articles.

1.1 Mine sweeping by the Danish Navy

The Danish Navy sweeps sea-mines and underwater unexploded ordnance, Fig. 1-1. A manned ship controls an unmanned surface ship. The unmanned ship is used to scan the sea bottom with sonar. If a mine-like object is detected a small remote operated vehicle (ROV) is applied to take a closer look at the object, Fig. 1-2. At ranges above 10-20 m the remote operated vehicle locates the object with sonar and within about 10 m the video camera and a strong spotlight is applied to get high resolution images. It is in this final stage of the location and optical identification of the sea-mine that the questions arise for the high resolution imaging system to answer. What kind of sea mine are dealt with? In what shape is the mine? Is it safe to let the diver place the detonation explosive? To give proper answers to the questions, an improved imaging system is needed. Though the applied video camera and spotlight system works reasonably well an answer is required for the question: Can an optical laser radar system do the job better?

The underwater optics and laser radar research is concentrated on finding a better solution for the present day camera and spotlight. This thesis presents a gated viewing high accuracy three-dimensional laser radar system that gets around some of the challenges of underwater optical imaging, (Chap. 3-6). The system exploits the narrow optical window of the water and avoids the backscatter by the state of the art technology of fast gating intensified CCD cameras. Whether the presented gated viewing laser radar system will end up in a new configuration with a remote operated vehicle in the future is an open question and beyond the scope of the thesis to answer, but the initial steps of research has been taken and the results are described in the following pages.

Three-dimensional imaging adds a new dimension to the standard two-dimensional contrast images. The solution for the Navy's operator of the remote operated vehicle could be a switching capability between two- and three-dimensional images acquired by the gated viewing two- and three-dimensional laser radar.

An underwater image of two sports-divers recorded in Øresund, the Sound between Denmark and Sweden, is shown in Fig. 1-3. The image is recorded with an amateur underwater digital camera. Notice the monochromatic green background of sunlight

filtered by the water. In general the image is blurred, un-sharp and with low contrast. The white spots in the image are small scattering particles called “marine snow”.

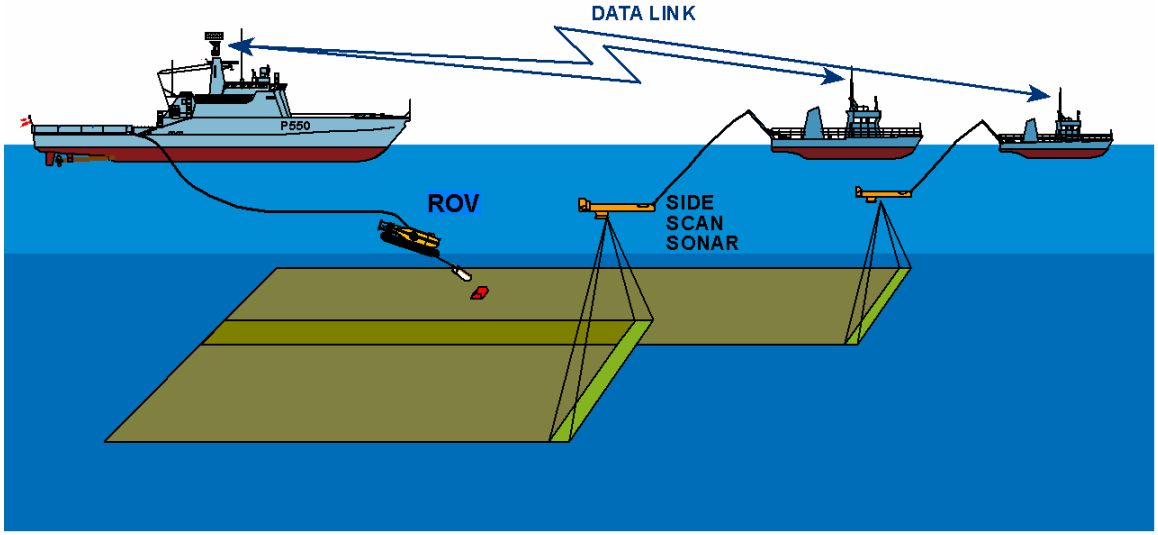

Fig. 1-1. Illustration of the mine sweeping by the Danish Navy. In the upper left is the manned mother-ship and control center. To the right are two unmanned surface ships towing one side-scan-sonar each. The underwater remote operated vehicle (ROV) is employed for sea-mine identification.

Fig. 1-2. The underwater remote operated vehicle employed for sea-mine identification by the Danish Navy. (Reference: A. Clausen, Danish Defence Research Establishment).

Fig. 1-3. Digital underwater image of two sports-divers in Øresund between Denmark and Sweden. Note the green background, the backscattering from the flash, and the large reflecting particles called marine-snow, (Personal photo recorded in Øresund, Denmark, 2003).

When a sea mine is swept the sweeping process goes through several phases. The first three phases can be categorized as detection, classification, and identification of the sea mine. The detection phase is to find any objects on the sea bottom or in the water column. The Danish Navy uses sonar in the detection phase. A large area is scanned with poor resolution compared to optical imaging. The second phase is classification of the object as mine-like or not mine-like. Mine-like objects are marked in the computer system for further investigation and identification. The optical identification is done by a remote operated vehicle equipped with a real time optical video imaging system. Sonar cannot deliver an image showing text and figures on the sea mine combined with high accuracy three-dimensional images. During the optical identification process it is crucial that the thrusters of the remote operated vehicle do not stir up the fine particles deposited on the bottom, because of immediate disturbance of the underwater visibility. Thus, if the image recording range can be increased it is of great value for the optical identification process of the sea mine. In this thesis a gated viewing technique is presented that will enable the image recording range to be increased.

The general scope of the thesis is outlined below:

- To develop an underwater laser radar, that applies the method of gated viewing for improved optical identification of sea-mines and objects on the sea bottom.
- To develop an algorithm that can be applied by the gated viewing laser radar for three-dimensional imaging, and to test and evaluate the algorithm acquiring knowledge of its advantages and disadvantages.

- To carry out stationary experiments with the laser radar under various conditions, starting in the laboratory and then in the open at successively longer ranges, to gain knowledge of the gated viewing three-dimensional imaging capabilities.
- To carry out experiments with objects submerged in water to gain knowledge of the gated viewing three-dimensional laser imaging performance in water.
- To study the water as an optical medium, by a model scattering phase function and an underwater optical data set, for the purpose of image enhancement and improved laser radar performance.
- To develop a digital simulation of the underwater gated viewing laser radar, to get a deeper understanding of the variables of the gated viewing laser radar system and the environment that influences the performance.

2 Underwater laser radar systems

This chapter presents a brief overview of the alternative laser radar systems and their employed principles. The systems are meant to be alternatives to the gated viewing three-dimensional laser radar system described in Chap. 3-6.

In short, all the underwater laser radar systems are developed to satisfy the purpose of reducing backscatter from the water column. The backscattering is the laser light which is scattered back towards the receiver and contains no useful information about the target which is imaged. The strong absorption of light (and electromagnetic waves in general) is a major limiting factor on the range performance of the underwater imaging laser radar systems. The challenge of the strong exponential absorption can hardly be overcome by other means than applying stronger lasers and a technique that waste as little of the laser power as possible.

2.1 Streak tube imaging lidar (STIL)

Lidar is the abbreviation for: “light detection and ranging”. The streak tube imaging lidar uses a pulsed optical laser and a streak tube, Fig. 2-1 and Fig. 2-2. The laser pulses are spread out in a fan beam transversal to the scan direction. The principle of operation of the streak tube is that all the received photons are converted into photoelectrons by a photo cathode. The electrons are then accelerated within a fast varying electrical field between the sweep plates and converted to photons again by a phosphor anode and finally absorbed by a charge couple device (CCD). For each pulse the CCD captures a two-dimensional sweep-image of the water column including the backscattered light. The result is that the backscattered light is swept onto different pixels from that of the reflected light of the object. The three-dimensional image is made by processing a sequence of sweep-images like the one illustrated in Fig. 2-2, (right). An example of a three-dimensional streak tube imaging lidar image is shown in Fig. 2-3. While the transversal- and the range coordinates are contained in the two-dimensional sweep-image, the third coordinate is obtained by scanning the fan beam across the object. This can be done by moving the system platform. The resolution in the scan direction is determined by the scan rate. Angular image resolution of the transversal direction is the width of the fan beam in units of radians divided by the number of transversal pixels on the CCD detector.

An advantage of the streak tube imaging lidar is that two- and three-dimensional images can be extracted from the same data.

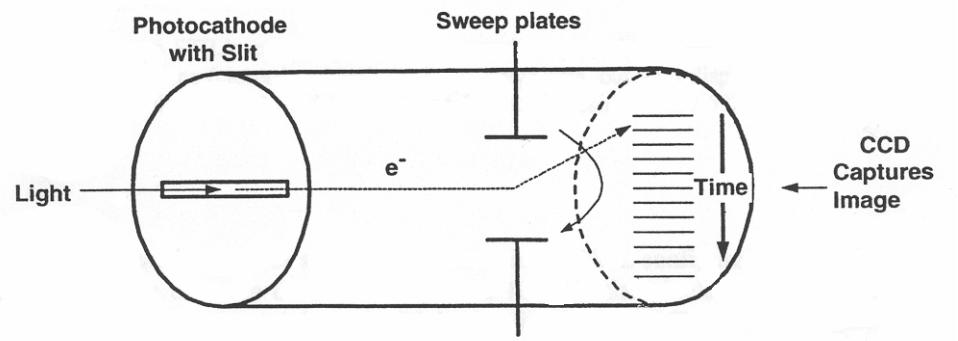

Fig. 2-1. Principle of the streak tube imaging lidar (STIL), [Gleckler et al. 2001].

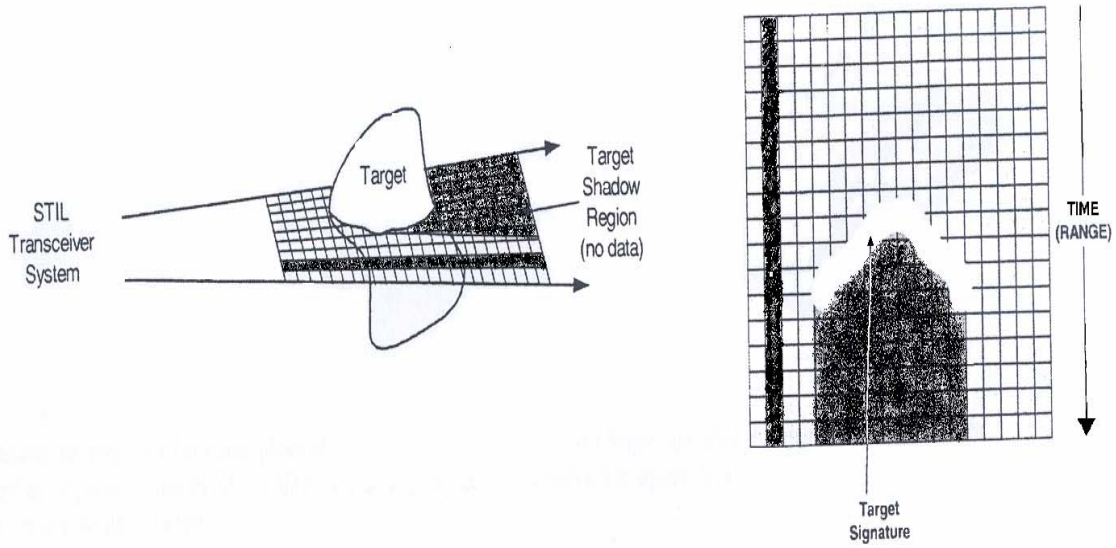

Fig. 2-2. Principle of the streak tube imaging lidar (STIL), [Gleckler et al. 2001].

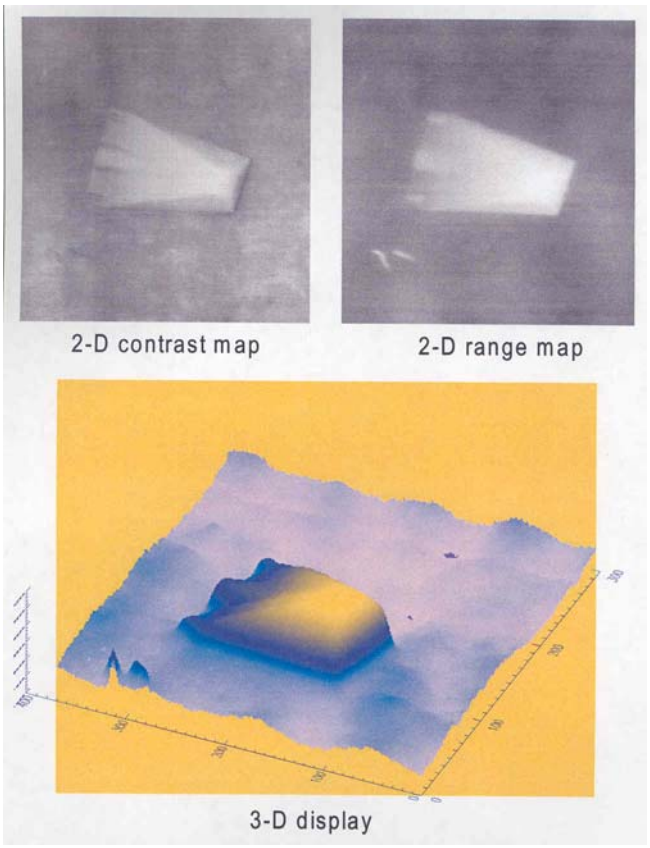

Fig. 2-3. Streak tube imaging lidar images of contrast, range, and three-dimensional representation of a sea-mine, [Nevis et al. 2002].

2.2 Laser line scanner

The laser line scanner scans the bottom by a continuous wave (cw) laser pencil beam and a photo multiplier tube with a narrow field of view. A photo multiplier tube is a single channel, but very sensitive light detector. The laser and the photo multiplier tube are separated, and the field of view is kept as narrow as possible to reduce water backscatter into the photo multiplier tube. The laser beam and the field of view of the photo multiplier tube are scanned in a line across the bottom by mirrors that are mechanically coupled and rotating, Fig. 2-4, [Saade et al. 1994]. The mirrors are faceted, with three or four facets. Moving the system platform perpendicular to the scanned line a two-dimensional image can be retrieved. The platform speed can be as high as 6 knots limited by the maximum rotation speed of the mirrors of 4000 rpm. The platform speed, the mirror rotation speed, and the sampling rate of the reflected laser light, should be adjusted to give a proper image resolution. An example of a laser line scanner image can be seen in Fig. 2-5. Triangulation can be exploited for three-dimensional image construction with the laser line scanner. To my knowledge the literature contains no reports on underwater three-dimensional images of bottom sea-mines recorded by a continuous wave (cw) laser line scanner. There exist other laser scanners applying a pulsed laser beam. In underwater object recognition the reflected laser pulse radiant energy is sampled in time and the object reflection is separated from the sea surface reflection and the backscatter from the water column. The object range is determined by measuring the two-way travel time of

the laser pulse object reflection. The scan angle, a differential global positioning system, and an inertial reference system are needed to locate the points of reflection correctly. The Swedish "Hawk Eye" system is an example of a pulsed laser line scanner, [Steinvall et al. 2004]. For example, the Hawk Eye has been applied from a helicopter to record an underwater three-dimensional image, with a resolution about a few meters, of a large ship wreck lying in 26 m of water.

The continuous wave laser line scanner has a disadvantage if the bottom conditions changes rapidly. The object may fall out of the intersection volume of the laser pencil beam and the field of view of the photo multiplier tube. An advantage of the laser line scanner is that it can be used for high resolution imaging over large areas, while the system is towed behind a ship.

Laser line scanners with several photo multiplier tubes used for fluorescence measurements are reported in the literature, [Strand, 2001; Coles et al. 1998].

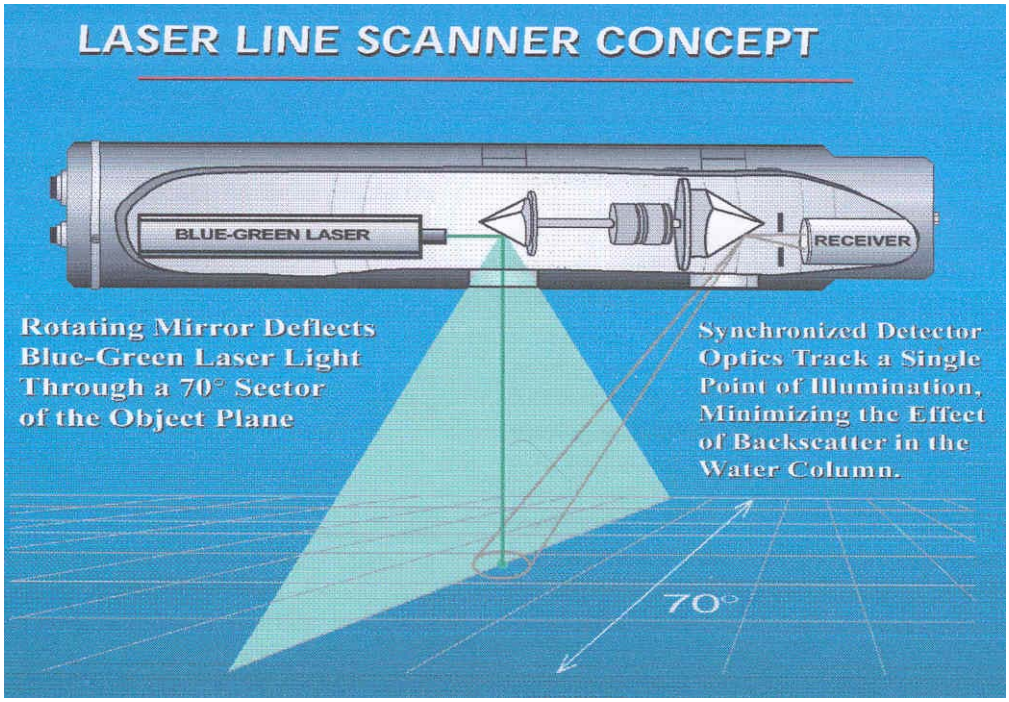

Fig. 2-4. Principle of a laser line scanner, [Saade et al. 1994].

Fig. 2-5. Laser line scanner image of wrecked airplane P-38 wing. The range to the airplane is not given, but a good estimate is 10 m in clear water, [Saade et al. 1994].

Since the 1990'ties a modulation technique has been under development for laser line scan systems and other laser radar systems. The technique is a spectral discrimination technique (Chap. 2.3 below), where the optical laser pencil beam is modulated with a radio frequency. The principle is that the scattered signal looses the modulation information, while the reflected target signal contains the modulation information. Contrast enhancement can be achieved by band-pass filtering the return signal. [Mullen et al. 2004, 1999]. Radio frequency modulation has been applied to pulsed laser radar systems. It has been experimentally verified that the modulation technique can improve the underwater target detection. [Pellen et al. 2002; Mullen et al. 2000].

A mono-static modulated three-dimensional real time (10 Hz) imaging system that uses light emitting diodes (LED's) instead of laser light has been reported, [Lange et al. 2000]. The illumination source consists of 160 LEDs, modulated at 20 MHz, with a total optical power of 0.8 W. The resolution in x, y, and z is some centimeters. The detector has only 25×64 elements. However, the method has not been applied underwater.

As the laser radar technology and especially the underwater laser radar technology is still relatively young it is too early to say which laser radar technique will be the best in the long run. Dedicated trials are needed before the question can be answered. In future the laser radar techniques and technologies can turn out to be complementary dependent on the application. Several different backscatter reduction techniques are applied by individual systems and more will be added in the future.

Within the last few years ”smart pixel” detector arrays are coming forward. ”Smart pixel” means that each detector element individually records the reflected laser pulse radiant energy in time and determines the range from the sampled waveform, [Dries et al. 2004; Stettner et al. 2004]. Yet these detectors have the disadvantage of few detector elements (128×128) and relative poor range resolution and transversal resolution of some centimeters. The detectors have not been applied underwater yet. Linear frequency modulation (“Chirp”) is yet another example of a three-dimensional laser radars technique, (has not been applied underwater), [Aliberti et al. 2004; Redman et al. 2004].
In atmospheric applications the laser radars commonly utilize the near-infrared laser wavelengths, because of availability, covertness, and eye-safety.

2.3 Reduction of backscatter in general

This section highlights some of the techniques that meet the challenge of underwater two- and three-dimensional imaging by separation of the object image bearing light from the backscattered light. Several of the backscatter reduction techniques can be applied by a single laser radar system. The reduction of the backscattered light is an improvement of the recorded images with regard to image contrast and range performance of the laser radar systems. Improved image contrast and range performance is an advantage for the optical identification of sea mines and other underwater objects. By analogy to the general experience of being blinded, when turning the strong head lights on, when driving a car on a foggy day, it does not help increasing the laser power to overcome the underwater backscattering.

A way to reduce the backscattered light in the laser radar receiver’s field of view the common volume of the laser illumination and the receiver field of view can be minimized, Fig. 2-6. The common volume can be reduced by separation of laser and receiver and by narrowing the laser beam and the receiver field of view. Here the reduction of the common volume is called spatial discrimination of backscattered light. The laser line scanner is an example of a laser radar system that utilizes this technique.

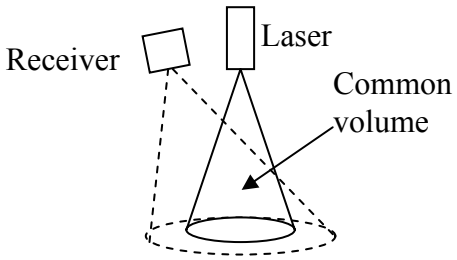

Fig. 2-6. Sketch of the common volume of the laser beam and receiver field of view. Reducing the common volume reduces the backscattered light into the receiver.

Spectral discrimination of scattered light can be a frequency band pass filter that eliminates all other frequencies than the laser frequency. Spectral discrimination is useful in applications, where diffuse sunlight is disturbing the image recording. Cameras can be equipped with a narrow optical band-pass filter. Optical band-pass filters 1 nm broad are available.

Signal modulation within the field of underwater optical laser radar systems is done by radio-frequency modulation. Modulation frequency band pass filtering of the reflected target signal reduces the backscatter. Experiments with modulation frequencies of 10-100 MHz and 1.5 GHz have resulted in improved target contrast. Future research will determine the optimal modulation frequency. A disadvantage of the radio frequency modulation method is that its practical application is limited by the speed of the available technology, [Pellen et al. 2002; Mullen et al. 2000].

The principle of polarization discrimination is that the image bearing photons have a different state of polarization than the backscattered photons. In practice the best choice of polarization filter may depend on the polarization characteristics of the target, [Swartz et al. 1991].

Gated viewing or equivalently range gating is time- or range discrimination. The principle of time- or range discrimination is to avoid all but the reflected target signal by fine control of the receiver recording time and by use of a pulsed laser. Delaying the receiver recording period from the emission of the laser pulse effectively discriminates the backscattered signal. The technique is called gated viewing and it is the laser radar technique applied for two- and three-dimensional imaging throughout the thesis, [Busck sub.2004; Busck et al. 2004a-b]. The gated viewing laser radar system configuration applied in the thesis is an innovative variation of other gated viewing laser radar configurations applying a pulsed laser and a range gated CCD camera, among which the Canadians do not have an algorithm for three-dimensional imaging and the Swedes do not apply an optical fiber, for example. An underwater gated viewing two-dimensional live mode video imaging system has been developed early in the 1990'ties by the Defense Research & Development Canada (DRDC), [Fournier et al. 1993]. Application of underwater gated viewing laser radar to Caisson positioning work has been reported, [Sakai et al. 1998]. Atmospheric long range gated viewing three-dimensional imaging has been done by the Swedes, [Klasen et al. 2004; Steinvall et al. 2003].

For more general information on active electro-optical systems see the literature, e.g. [Fox, 1996].

3 Gated viewing laser radar

This chapter describes in detail the laser radar applying the method of gated viewing. The chapter is closely related to Chap. 2 above and could be regarded as a detailed subsection of Chap. 2. The gated viewing laser radar is developed and the laser radar system components are described, i.e. the laser, the CCD camera and the optical fiber. The reason why the gated viewing laser radar system is an improvement compared with the conventional underwater imaging system applied for optical sea-mine identification is the effectively discrimination of the backscattered light and the additional range information given by the camera delay. At the end of the chapter the system is tested in air for its ability to eliminate the backscattering in volume between the laser radar and the target. In the laboratory the test is performed by hanging a (camouflage) net in front of the target. In the open air the gated viewing laser radar is tested in a coastal area with dense fog encapsulating the target. The experiment in the dense fog is an analog simulation of the underwater environment with much less absorption. The fine results of the laboratory test and the test performed in dense fog are presented in Sec. 3.4 below.

3.1 Gated viewing with a pulsed laser and a fast gating CCD camera

The principle of laser pulse range gating is to keep the camera closed and wait until the reflected photons from the target return to the camera.

The laser pulse is emitted by the laser. When the laser pulse is emitted the trigger pulse from the laser to the camera onsets the camera delay. The camera delay determines when the camera gate opens for recording of the reflected laser pulse, Fig. 3-1. The typical camera gate time is equal to the laser pulse time. The camera records the reflected laser pulse radiant energy from the range gate. The depth of the range gate depends on camera gate time and laser pulse time, Sec. 3.3, [Busck, sub.2004].

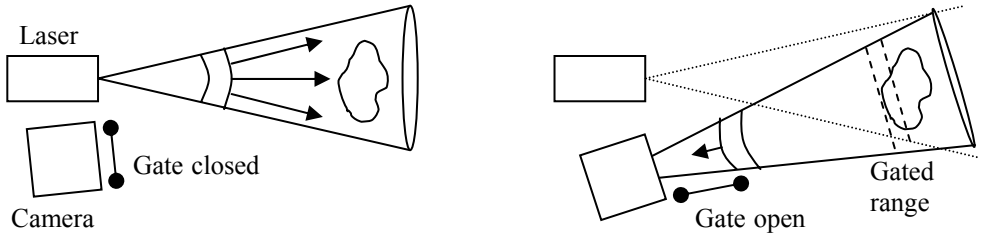

Fig. 3-1. Principle of the gated viewing laser radar. Left: The laser emits a short pulse that undergoes scattering while propagating towards the target. The camera is closed to avoid the backscattered light. Right: The target has reflected the pulse and the camera gates the reflected pulse.

3.2 System specifications and description

Throughout the thesis several applications of the gated viewing laser radar system are presented. The laser radar system set-up varies according to the application. The system

has been set-up for three applications: Short range (10 m) high accuracy three-dimensional imaging in the laboratory, medium to long range (200-1000 m) telescopic three-dimensional imaging, Fig. 3-2, and short range underwater three-dimensional imaging. The long range three-dimensional imaging could be interesting for airborne shallow water sea-mine identification and object recognition in general. The common parts for all the set-ups of the laser radar system are the pulsed laser, the laser driver, the fast gating intensified CCD camera, an ordinary computer, the 8-bit frame-grabber card, two software programs, the cables, and the power supply for the camera. The use of an 8-bit frame-grabber instead of a higher bit frame-grabber is justified by the image noise, which is well beyond the 8-bit resolution and approximately proportional to the square-root of the image pixel value.

Fig. 3-2. Telescopic gated viewing high-accuracy three-dimensional laser radar. The fast CCD camera and the telescope are mounted on a tripod in the middle of the image. The laser is to the right of the telescope mounted on an optical bar. The image recording and analysis is done by the computer. The laser radar is set-up at the Danish Defence Research Establishment for three-dimensional imaging of an antenna cluster, (Sec. 5.3 below).

The laser is passively Q-switched and outputs laser pulses with a pulse repetition rate of 32.4 kHz. The time between each pulse emission is 31 μs. In air the laser pulses travel at the speed of light of 2.99×10^8 m/s. The range between successive laser pulses is 9.3 km. The laser pulses have to travel to and from the object, so the maximum range of the gated viewing laser radar system is 4.65 km. Thus the laser repetition rate determines the maximum range of performance for the system. Above the maximum range ambiguity can occur between the reflected signals of two successive laser pulses.

The laser wavelength of 532 nm is chosen for optimal transmission in water. The measured spectrum of the laser is shown in Fig. 3-3. The standard deviation of 0.03 nm can be used for computation of the power loss in optical fibers, [Saleh et al. 1991].
They laser is delivered with no manually adjustable buttons, screws or switches. Operation of the laser and the laser driver is simply plugging in the power cable and turn the power key. The simple operation of the laser makes the operation of the whole laser radar system the more simple. The laser specifications are summarized in Table 3-1. Safety goggles are a requirement for safe operation of the laser radar system. Even with safety goggles it is advised not to look straight into the laser beam.

Brand	Nanolaser
Wavelength	532 nm
Pulse repetition frequency (PRF)	32.4 kHz
Pulse energy	4.3 µJ
Pulse time	0.5 ns
Peak power	8.6 kW
Average power	140 mW
Power consumption	≈ 250 W
Operating temperature	15-35 Deg.C
Beam divergence	1.5 mrad

Table 3-1. Laser specifications

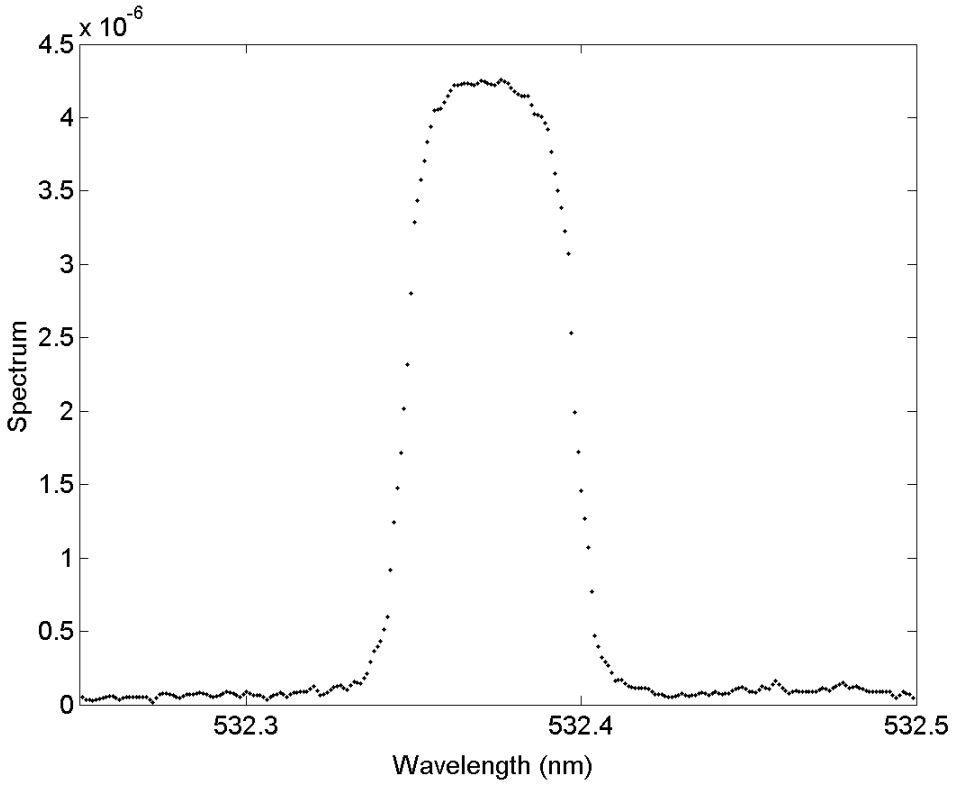

Fig. 3-3. Laser spectrum with center wavelength of 532.37 nm and standard deviation of 0.03 nm. The resolution is 0.05 nm. (Measured with a spectrometer at DTU-COM, Technical University of Denmark, 2004).

The principle of the fast gating intensified CCD camera is sketched in Fig. 3-4 and described in details below. The specifications of the camera are summarized in Table 3-2. The photo-cathode converts the incident radiant energy to photo-electrons with an efficiency given by the photo-cathode's spectral quantum efficiency QE. The photo-cathode material S20Q has a quantum efficiency of about 20 % at the visible wavelength of 532 nm. The quantum efficiency drops to 3 % in the ultraviolet 150 nm and 0.3 % in the near-infrared 820 nm. The photo-electrons are amplified by a set of narrow avalanche photo-multiplier-tubes in the micro-channel-plate (MCP), which control the gain of the camera. The gain is changed by varying a potential across the MCP. The gain is experimentally determined to be an exponential function of the gain-voltage with an exponent of 10 fitting well within 3 % by linear regression, see App. A. The MCP gate time is activated by application of a negative voltage of 120 V. The duration of which determines the opening time of the gate. The gate contains a jitter of 20 ps, which is 10 % of the shortest gate time of 200 ps. The minimum gate time is about 25 times shorter than the current range gated systems in 1991, [Strand, 1991]. The amplified secondary electrons are converted to photons by the phosphor screen. The secondary and intensified photons are detected by the 752×582 CCD elements. To avoid damage of the intensifier unit and CCD the gate time should be shortened before adjustment of the MCP gain-voltage.

The analog output image from the camera is digitized by an 8 bit frame-grabber (National Instrument: NI-1408). The frame-grabber has adjustable black and white levels, which is set to 0.0 V and 0.8 V, respectively, throughout the majority of experimental data presented in the thesis. The black and white levels tell the frame-grabber to make an 8 bit digitization from 0.0 V to 0.8 V. For example a signal of 0.4 V input to the frame-grabber gives an output value of $(2^8 \times 0.4/0.8)-1 = 127$. When the signal is above the pre-defined white level or below the black level the values assigned are the minimum and the maximum values, i.e. 0 or 255, respectively. In general, an image pixel is said to be saturated when the pixel has the maximum value of the frame-grabber digitization, which is 255 for the eight bit frame-grabber (0-255). It should be noted that a saturated image pixel is not necessary equivalent to a saturated detector element and vice versa, dependent on the setting of frame-grabber black and white levels. It has been found experimentally that there is a dark noise input to the frame-grabber corresponding to 0.1 V. This background noise level was determined by recording images with the cap in front of the optics and varying the frame-grabber white level until the background images became saturated (i.e. value of 255). A change of black and white level can be done to enhance weak signals in an image or disregard the background noise, for example.

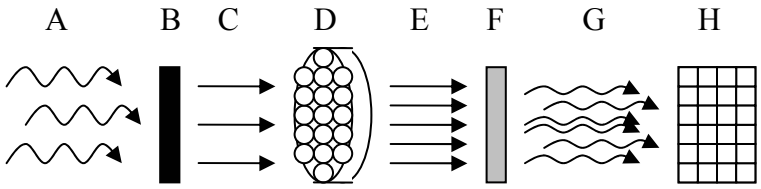

Fig. 3-4. Sketch of the intensified CCD camera. A: Photons incident on the camera optics, B: Photo-cathode converts photons to photo-electrons, C: Photo-electrons, D: Micro-channel plate (MCP) with multiple narrow electron avalanche channels, E: Multiplied or amplified electrons, F: Phosphor screen converts electrons to photons, G: Amplified photons, and H: Charge-coupled device (CCD) detector.

Brand	Standford 4PICOS
Detector	Intensified CCD
Detector size	752 x 582 pixels
Gate time	≥ 200 ps
Delay step	≥ 100 ps
Internal electronic delay	≈ 85 ns
Delay drift (cold system)	≈ 500 ps
Delay drift (warm system)	< 50 ps
Jitter in gate time	≈ 20 ps
Power consumption	30 W
Operating temperature	10-30 Deg.C

Table 3-2. Fast gating intensified CCD camera specifications.

The internal electronics of the camera cause an unavoidable delay of about 85 ns. It has been observed that the magnitude of the internal delay changes over time. Short time variation occurs when the laser radar system is cold. It takes about half an hour for the system to stabilize. Variation has been observed over months. Ideally the laser radar system needs to be calibrated with respect to the internal electronic camera delay before usage. In practice it is not always possible to calibrate. The calibration may be ignored depending on the application. By an internal electronic camera delay of 85 ns, the laser pulse travels 25.5 m in air before the camera is ready to gate. The laser radar minimum range corresponding to the internal delay of 85 ns is 12.75 m. For laser radar imaging below this minimum range the laser pulses have to be delayed in some way. Imaging has been done in the laboratory by delaying the laser pulses by two mirrors separated several meters apart. Laser pulse delay by mirrors has several disadvantages. First, it is an impracticable solution for imaging in the field with several meters between the mirrors. Second, the shorter distance between the mirrors requires more reflections and increase loss of pulse power, and mirrors with high reflection coefficients that are big enough for the purpose are difficult to get or expensive. Subsequently, the mirrors are replaced by an optical fiber.

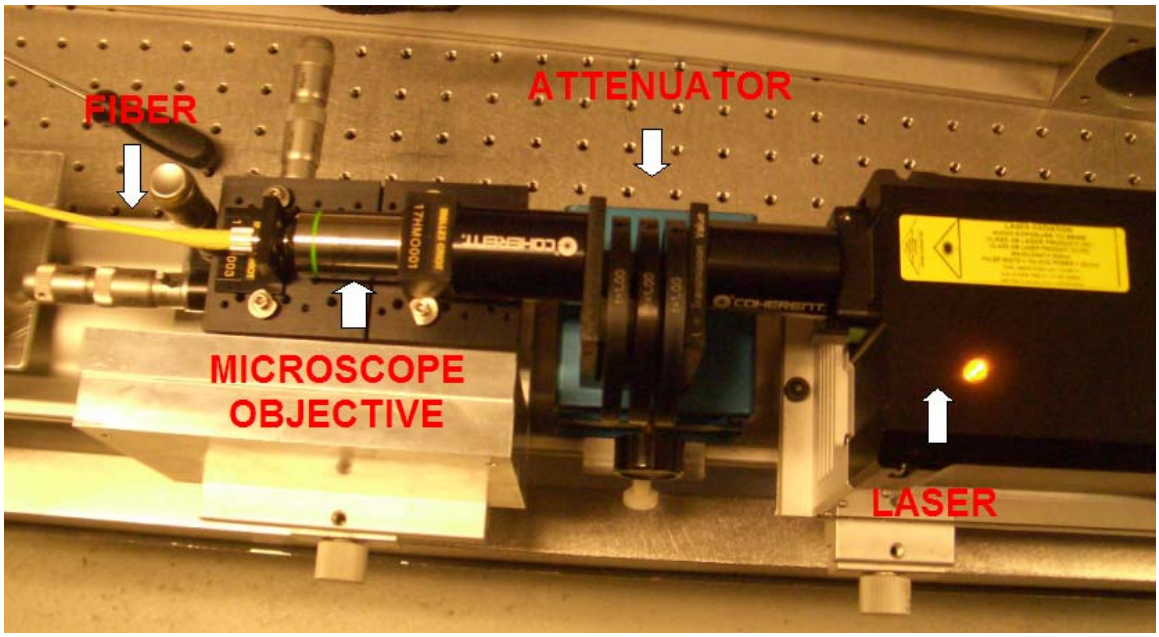

Fig. 3-5. The set-up for the optical fiber coupling. The optical fiber end and the microscope objective are mounted on a xyz-micrometer alignment unit.

The optical fiber is applied as optical delay to match the internal electronic camera delay. The single mode fiber is used for the short range underwater application. The optical fiber has several advantages. First, the optical fiber is flexible and can be rolled up into a small space. Second, for future underwater imaging campaigns the fiber allows for the laser and driver to be placed at the sea surface, while the fiber is linked to the underwater camera. The drawback of the fiber is the coupling of the laser pulses into the fiber. The laser pulses are focused into the optical fiber by the 20× microscope objective. The fiber is 30 m long with a collimating lens at the output. The diameter of the fiber core is 3.5 µm and the in-coupling power loss is about 80 % of the laser output power. The power is attenuated in the fiber by a factor of 1.4. In near future the fiber will be replaced by a crystal fiber with 15 µm core diameter which will reduce the in-coupling power loss. The high peak power of 8.6 kW of the laser stimulates Raman scattering in the fiber. The stimulated Raman scattering is a nonlinear optical phenomenon, [Agrawal, 2001; Stolen et al. 1984]. The Raman scattering makes it difficult to determine the water attenuation coefficient in practice, Sec. 6.3 below. In near future the Raman scattering will be much reduced when the crystal fiber is applied. The crystal fiber has two disadvantages: the crystal fiber has a larger bend-radius and larger internal attenuation.

The set-up for the optical fiber coupling is shown in Fig. 3-5. The image acquisition program interface used to record the range gated image is shown in Fig. 3-6. The acquisition software is programmed in Labview and controls the camera settings of gate time, delay, delay step interval, gain voltage, and the number of images, [Labview, 2003]. The program can either run in live range gated mode or in range gated image acquisition mode. In live mode the camera gate time, the camera delay, and the gain voltage can be changed in steps. A general manual procedure for the right range adjustment is to start out with a longer gate time and shorter delay than intended for the image acquisition. The long gate time gives a deeper range gate and makes it is easier to find the target of

interest. With the short start delay and long gate the delay is manually stepped up in large steps until the target is within the range gate, then the range can be adjusted by smaller delay steps and finally the gate is decreased.
The camera gate time, the camera delay, and the gain voltage can be automatically increased or decreased in steps in the image acquisition mode. The delay has to be either increased or decreased for three-dimensional imaging, see Chap. 4 below. The gain voltage can be increased to match the environmental attenuation in range, for example.
The user interface is equipped with the histogram panel showing the histogram of the 8-bit live image grey values, or by choice a line profile panel showing the image values of the line defined by the operator in the live image. The line profile can be used to focus the camera optics on the target.
If an image sequence is acquired it is stored in the default directory or the directory defined by the operator. Depressing the analysis button causes the analysis program to automatically analyze the recorded image sequence. See Sec. 4.4 below, for a description of the analysis program.

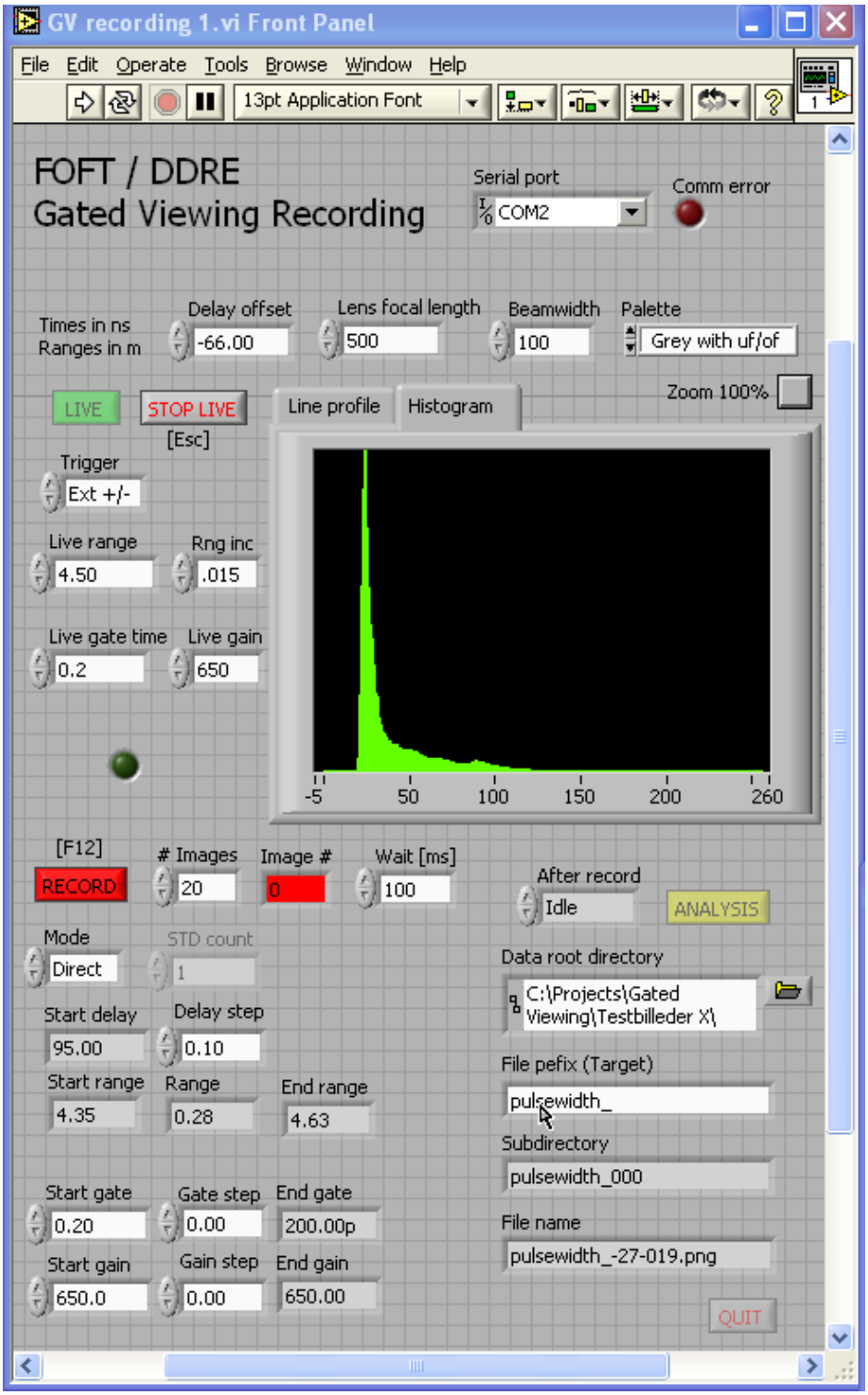

Fig. 3-6. User interface of the gated viewing laser radar image acquisition program. Only a few of the controls are interesting, that being the *live* and *stop live*, which allows for real-time gated viewing video imaging, the *live range*, the *live gate time*, the camera *gain*, which is actually the camera gain voltage setting and not the camera gain, (see App. A), the number of *images*, the camera *delay step*, which determines the delay step time between the recorded images in an image sequence, and the *record* button, which starts the image sequence recording. (The histogram displays the grayscale of the live mode image. The live mode image is not shown here).

3.3 Range gating

Gated viewing is the viewing of the image of the recorded laser pulse radiant energy reflected at the points within the range gate and then merged into the two-dimensional CCD detector array in the camera.

Consider the timeline at the laser radar system with the camera gate and the reflected laser pulse, Fig. 3-7. The timeline zero is equal to the emission of the laser pulse and the onset of the camera delay. For simulation the time for the emission of the laser pulse can be considered as the time for emission of the center of the laser pulse, for example, [Busck, sub.2004]. The image pixel value depends on the amount of reflected laser pulse radiant energy received during the camera gate time. The image pixel receives only the radiant energy which is reflected within the field of view of the pixel. The reflectivity, the shape, and the orientation of the reflection points within the pixel's field of view are among the factors that determine the image pixel value.

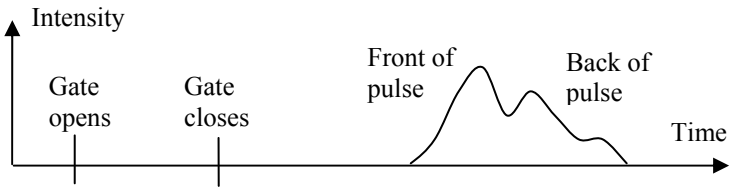

Fig. 3-7. Timeline at the laser radar system with the camera gate time and the reflected laser pulse.

The camera gate time and the laser pulse time determine the depth of the range gate, [Busck, sub.2004]. The gated range is the range interval from which the laser pulse radiant energy has been reflected and detected by the camera. Given the camera delay the farthest point in the gated range is illuminated by the front of the laser pulse and detected by the end of the camera gate time. Thus the farthest point reached in the gated range is dependent on camera gate time and laser pulse time. The closest point in the gated range is illuminated by the end of the laser pulse and detected at the start of the camera gate time. Thus the closest point in the range gate is not dependent on camera gate time. The depth of the range gate is dependent on the camera gate time, the laser pulse time, and the speed on light. The depth of the range gate is approximately the camera gate time plus the laser pulse time times half the speed of light. For example, camera gate time 0.5 ns and laser pulse time 0.5 ns gives the depth of the range gate 15 cm. Note that underwater the same range gate is 15 cm/1.33 = 11 cm, where the refractive index of water is 1.33.

In the simulation of the gated viewing laser radar it is assumed that the camera delay is triggered when the center of the laser pulse leaves the laser, [Busck, sub.2004]. Thus the absolute range to the center of the range gate depends on the laser pulse time, the camera gate time, the camera delay setting, and the refractive index of the medium. In practice, delay in the trigger cable and electronic delay in the camera need to be considered.

There is not a single laser radar equation that describes all laser radar systems. Each laser radar system can have unique features that require a unique laser radar equation, (e.g. [Busck, sub.2004; Pellen et al. 2002; Lagaye et al. 1997; Acharekar, 1997; Fournier et al. 1993; Austin et al. 1991; Bjarnar et al. 1991]. In general the laser radar equation describes the characteristics of the system and the attenuation characteristics of the radiation transfer of the environment. A laser radar equation for the gated viewing three-

dimensional laser radar imaging in air and underwater has been exploited for digital simulation, [Busck, sub.2004].

3.4 Applications of two-dimensional gated viewing

In April 2003 trials were conducted at the coastal area of Oksbøl, which is located in the south-western part of Denmark facing the North Sea. The experiments were done at night-time at freezing temperature and with the icy bone-chilling mist and fog coming in straight from the North Sea. Though the conditions were harsh it is an excellent opportunity to document some of the strengths of the gated viewing laser radar. The UN-vehicle engulfed in fog recorded at 100 m range is shown in Fig. 3-8, with a long camera gate time (left) and a short gate time (right).

An important advantage of the gated viewing laser radar is the ability to see through obscurations. For example the obscurants can be vegetation or a camouflage net. The ability to see through a net was tested at the Danish Defence Research Establishment. The chosen target is a small toy jeep made of wood, Fig. 3-9 (left). The size of the jeep is 20 cm. The range to the jeep is 7 m. The net is placed about 6 cm from the jeep and the camera is focused on the net, Fig. 3-9 (middle). The camera gate is shortened and the range gate is fixed on the jeep behind the net, Fig. 3-9 (right). The shadow of the net is projected onto the jeep.

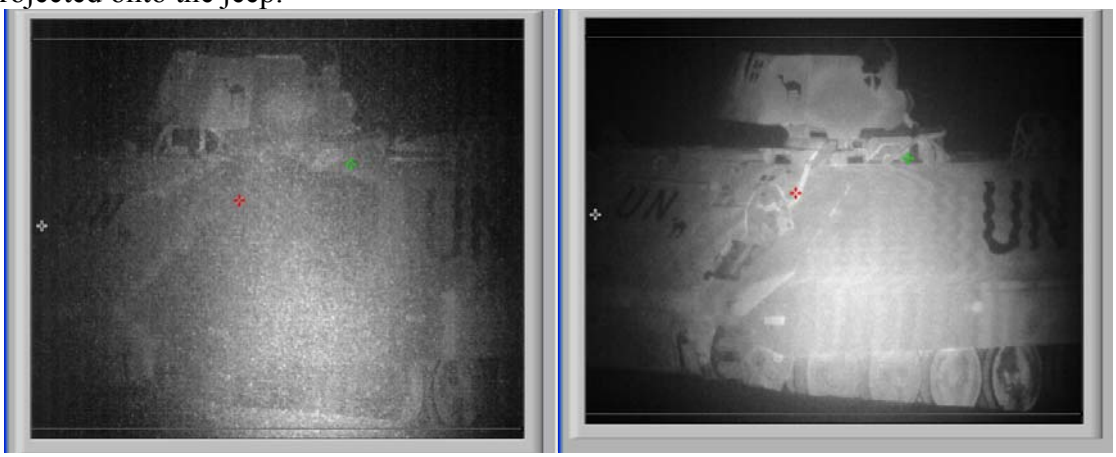

Fig. 3-8. Gated viewing laser radar imaging trial at nighttime in the coastal area of Oksbøl, Denmark, 2003. Left: White UN-vehicle engulfed in fog and illuminated by the laser and with a long camera gate time. Right: Fine control of the camera delay and a short camera gate time effectively removes the backscatter from the intervening fog.

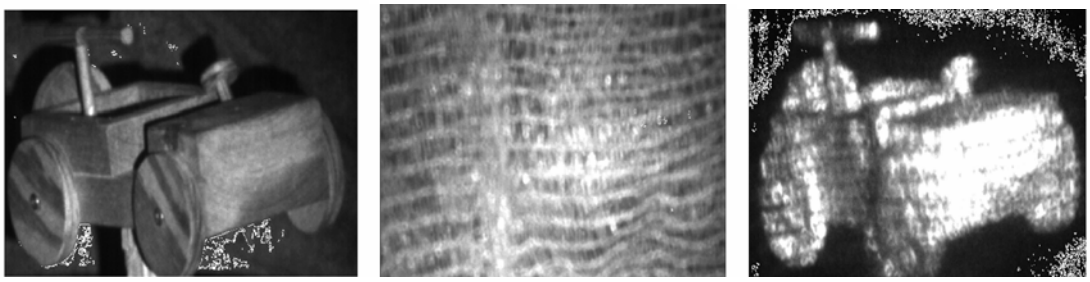

Fig. 3-9. Gated viewing laser radar imaging. Left: The target is a small jeep of size 15 cm placed at 7 m range. Middle: A net is placed about 6 cm in front of the jeep. Right: The range gated image of the jeep, where the net in front of the jeep is gated away. The shadow of the net is projected onto the jeep.

Range gated images highlight the reflection points within the gated range. If an object is further away than the farthest possible reflection point in the gated range it is not detected by the image recording system. If an object is closer to the laser radar system than the closest range gated point the shadow of the object is detected in the image. The technique can be utilized for object recognition, [Steinvall et al. 2003].

Two-dimensional gated viewing images can be exploited for object range determination by the approximate range r to the object

$$r = \frac{cT_{delay}}{2n}, \tag{3.1}$$

where c is speed of light, T_{delay} is the camera delay, and n is the refractive index of the medium, i.e. n = 1.0 in air, n = 1.33 in water, and n = 1.4 in the optical fiber.
The expression Eq. 3.1 is the more accurate the shorter the camera's gate time and the laser pulse time, because of the depth of the range gate, (Sec. 3.3 above).

3.5 Summary and conclusion

The laser, the camera and the optical fiber have been described. The principle of range gating has been discussed. The maximum range of the gated viewing laser radar system of 4.65 km is determined by the laser pulse repetition frequency. Above the maximum range ambiguity may occur between the reflections from two successive laser pulses. Application of gated viewing laser radar in dense fog is presented. Object recognition by range gated shadow is discussed and can be used for detection and classification, but for object identification more information is needed.
It is concluded that the method of range gating can eliminate severe backscattering in no time, which is a major advantage and one of the strengths of the gated viewing laser radar. The experiment with the UN-tank in the fog, in the coastal area, can be regarded as an analog simulation of the underwater environment with less absorption. The fine results legitimate the underwater experiments presented below.

4 Gated viewing three-dimensional imaging

The capability of three-dimensional imaging is a major advantage for optical sea-mine identification, because the three-dimensional images can be rotated in the computer and the objects in the image can be viewed from different directions. This chapter presents the innovative algorithm of weighted averages for fast three-dimensional image production by the gated viewing laser radar, (see also [Busck et al. 2004a-b]). The Swedes apply another algorithm based on a threshold for gated viewing three-dimensional image formation, [Steinvall et al. 2003]. This chapter contains a detailed discussion of the three-dimensional image formation, based on the proposed algorithm, and the factors that influences the quality of the three-dimensional result. The basic image recording technique is described in Sec. 4.1. The algorithm for three-dimensional image formation is described in Sec. 4.2. Range accuracy and errors are discussed in Sec. 4.3. A short introduction to the acquisition program is given in Sec. 4.4. Summary and conclusion is given in Sec. 4.5.
The applications of gated viewing three-dimensional imaging are postponed to Chap. 5.

4.1 Basic image sequence recording

The Gaussian laser beam is spread out to illuminate the whole target by each laser pulse. The gated viewing laser radar is mono-static, i.e. there are no scanning parts. The laser and the camera are co-located. The high laser pulse repetition rate of 32.4 kHz is exploited for image recording at the image acquisition rate of 50 Hz. For each recorded image 648 laser pulses are integrated on the camera's CCD detector assuming no loss of pulses during image write out from the camera. Within 20 ms the camera delay changes once, the camera gate time and the camera delay are triggered 648 times, and the image is output from the camera. The laser pulses are separated by 31 μs, enough time for the camera electronics to change the camera delay. The high number of pulses increases the signal to noise ratio, which is a major advantage of the laser radar system. The camera delay is increased the predefined delay step and the next image in the sequence is recorded automatically. For example, the camera delay values of an image sequence could be 60.0, 60.1, 60.2, …, 69.9 ns, range gating an object of size $(20\ \text{cm})^3$ at 10 m range, where the range depth of the entire image sequence is about 1.5 m. Typically an image sequence consists of 50-100 images, (Fig. 4-1). It takes 1-2 s to record the image sequence at 50 Hz. The image sequence is stored in a new directory on the computer ready for fast three-dimensional image processing. A laser radar image sequence of 50 range gated images and the corresponding three-dimensional laser radar image is presented in App. D. The three-dimensional image is computed by the algorithm described in Sec. 4.2. The sequence in App. D of 50 images is recorded at 7 m range with camera gate time 0.5 ns and camera delay step 0.1 ns, which are typical values of the camera gate time and the camera delay step.
The gated viewing technique for three-dimensional image formation has a disadvantage. Because of the short range gate not all the laser pulse radiant energy reflected at the target is recorded in the individual images of the image sequence, i.e. some of the laser pulse radiant energy reflected at the target is gated out and lost. The amount of energy lost depends on the depth of the range gate, and the size and shape of the target.

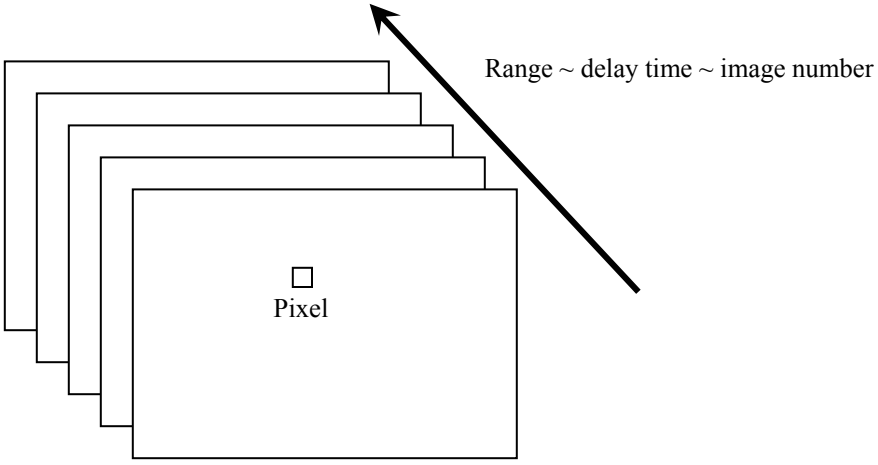

Fig. 4-1 Images are recorded sequentially by automatically changing the camera delay in short steps of one- or two-hundred pico-seconds. For example, the camera delay values of an image sequence could be 60.0, 60.1, 60.2, …, 69.9 ns, range gating an object of size (20 cm)^3 at 10 m range, where the range depth of the entire image sequence is about 1.5 m. The arrow illustrates the relation between increasing range, delay time, and image number.

Consider a single pixel and the pixel values through the image sequence. The image pixel value can be thought of as the collapse of the laser pulse reflections of the three-dimensional space bounded by the field of view of the pixel and the depth of the range gate. The image pixel value can be simulated by a laser radar expression, [Busck, sub. 2004]. The laser pulse time of 0.5 ns, the typical camera gate time 0.5 ns, and the typical camera delay step 0.1 ns cause the range gates of the images in the sequence to overlap. By overlapping the range gates the reflected laser pulse radiant energy is discretely sampled by the fast gating of the camera. The camera delay step and the depth of the range gate determine the number of samples. The single pixel values in 8-bit units through a typical sequence of 50 images are shown in Fig. 4-2. The target is a white-board at about 5 m range. The camera gate time is 0.5 ns and the delay steps are 0.1 ns. In the first 20 images the camera delay time is too short for the gated range to reach the white-board. In the images 29-33 the pixel gets the maximum return of the laser pulse, and in the images 46-50 the camera delay is longer and the gated range lies behind the white-board. The background is about 20 and depends on the setting of the frame-grabber black and white levels. The rising edge corresponds to the front of the laser pulse being gated at the end of the camera gate time. The falling edge corresponds to the end of the laser pulse being gated at the start of the camera gate time, [Busck, sub. 2004].
The variance of the pixel profile for sufficiently small delay steps

$$\sigma^2 = \sigma^2_{pulse} + \sigma^2_{gate}\,, \tag{4.1}$$

where σ^2_{pulse} is the variance of the laser pulse and σ^2_{gate} is the variance of the camera gate time, [Busck et al. 2004a].
The expression Eq. 4.1 is experimentally confirmed by repeating the recording of the gated viewing image sequence of the white board, the camera gate time is increase by 0.1

ns from 0.3 to 1.0 ns in eight image sequences of 35 images, Fig. 4-3. The saturated image sequence profile is recorded with increased camera gain. In contrast to Fig. 4-2, which is a single pixel profile, the profiles in Fig. 4-3 are multiple pixel profiles. Thus each profile value is the average of several pixels. The averaging is done to suppress the noise and make the profile broadening by camera gate time more distinct. In general the width of the pixel profiles corresponds to the depth of the range gate. Thus, the width of the pixel profiles times the speed of light can be compared to the measured depth of the range gate, [He et al. 2004].
In the next section (4.2), it is shown how the pixel range is determined by computing the weighted average of the single pixel values through the image sequence.

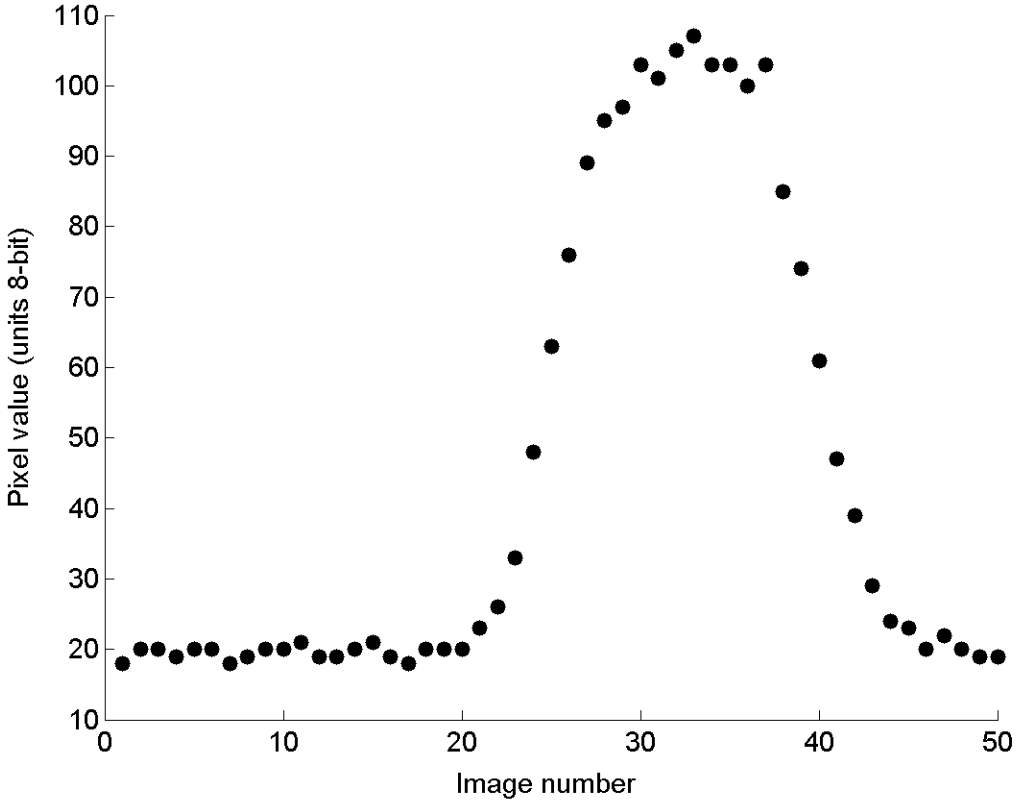

Fig. 4-2 Single-pixel values through the image sequence of 50 images. The target is a white-board at 5 m range. The camera gate time is 0.5 ns and the delay steps are 0.1 ns. In the first 20 images the camera delay time is too short for the gated range to reach the white-board. In the images 29-33 the pixel get the maximum return of the laser pulse, and in the images 46-50 the camera delay is longer and the gated range lies behind the white-board. The background is about 20 and depends on the setting of the frame-grabber black and white levels.

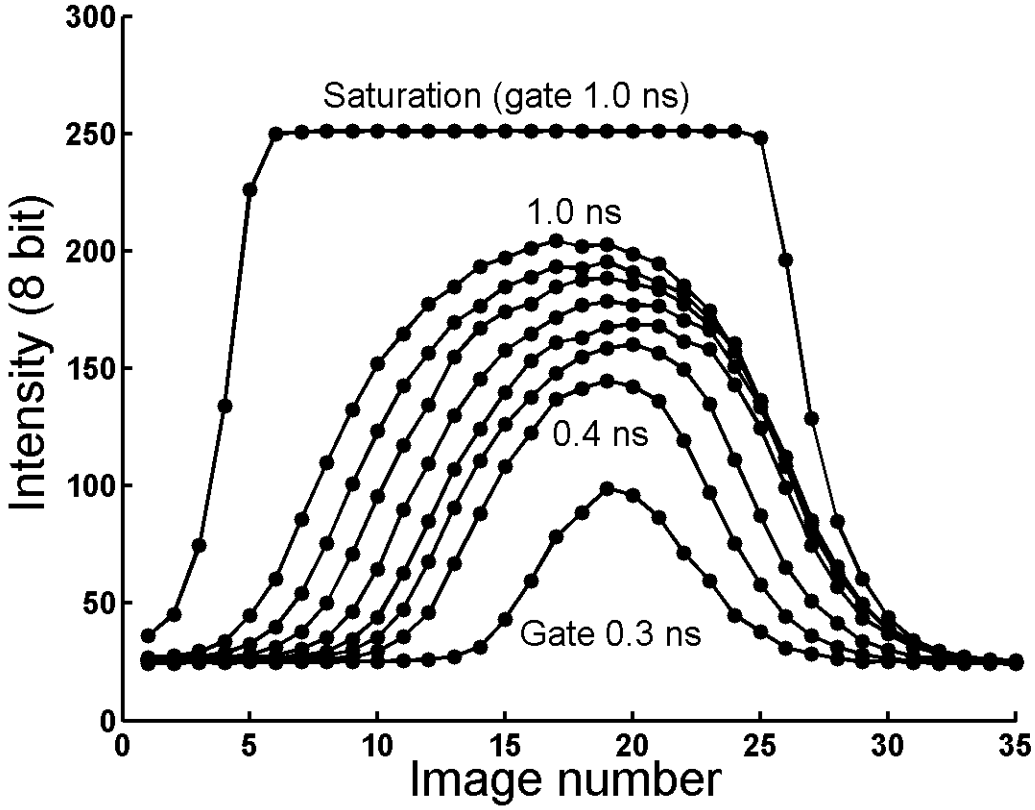

Fig. 4-3. Multiple pixel profiles of repeated image sequence recording of the white board. The longer the camera gate time the larger the variance of the profile. Each profile is the average of many pixels. The camera gain setting of the saturated profile with camera gate time 1.0 ns is higher than the non-saturated profile with camera gate time 1.0 ns.

4.2 Algorithm for three-dimensional image formation

The method of three-dimensional image formation applied in the thesis for range determination of a recorded image sequence is a method that applies the weighted average of the pixel profiles. It is implicitly understood that a three-dimensional image in this context is an image displaying the weighted range to the group of points in the pixel field of view. The proposed method is previously unpublished until August 2004, [Busck et al. 2004a].
The range

$$\langle r \rangle = \frac{c}{2n}\left(t_0 + \Delta t\left(\langle i \rangle - 1\right)\right), \tag{4.2}$$

where c is the speed of light, n is the refractive index, t_0 is the camera start delay time, Δt is the camera delay step time, < r > is the average range corresponding to the weighted average image number

$$\langle i \rangle = \sum_{i=1}^{N} iQ_i \Big/ \sum_{i=1}^{N} Q_i \,, \tag{4.3}$$

where Q_i is the pixel value in the i'th image (1,2,…,N), and N is the number of images in the sequence.
There are several alternative ways in which the pixel range can be determined. For example the range can be found by threshold of the rising edge or the falling edge of the pixel profile. If applied to the unprocessed image sequence, such a method has the disadvantage of not being able to determine the range better than the corresponding length of a delay step. Another alternative could be to estimate the range from the maximum of the raw pixel profile. Again the disadvantage is that the range can not be determined any better than the corresponding length of a delay step. The different methods could be applied to a low-pass filtered pixel curve or to some (polynomial) curve fitting of the pixel profile. Either variant requires more computations which increase the time used to three-dimensional image formation.
In the next section the range accuracy is discussed.

4.3 Range accuracy, precision, resolution and deformation

In this section a set of concepts useful for evaluation of the performance of the three-dimensional laser radar are discussed. The concepts of range accuracy, range precision, range resolution and target shape deformation are considered below.
The range accuracy is in practice considered as the standard deviation of the range noise in the equidistant pixels of the range image, thus the range accuracy can be determined directly from the range image. A derivation based on error analysis of the pixel profile leads to the range accuracy, [Busck et al. 2004a],

$$\Delta r \approx \frac{c}{2n}\frac{\sigma}{SNR}, \tag{4.4}$$

where c is the speed of light, n is the refractive index, σ is given by the expression Eq. 4.1, and the SNR is the signal to noise ratio. Determination of the signal to noise ratio in the expression Eq. 4.4 is described in the literature, ([Busck et al. 2004a]).
The range precision is considered as the ability to determine the overall range to the object, i.e. the range precision is a measure for a systematic range offset throughout the entire range image. Range precision cannot be estimated directly from the range image itself, because it is impossible to determine whether the image has a systematic range offset. A direct method of determining the range precision at short range is to measure the range from the laser radar system to the object with a ruler and compare with the predicted laser radar range. At long range a calibrated laser range finder may be used instead of the ruler. A correction for improvement of the range precision has been described, [Busck et al. 2004b]. The correction is applied to compensate for the broadening of the pixel profile caused by the camera gate time. The variation in the uncontrollable internal electronic camera delay is a source that deteriorates the range precision. In general a variation in the electronic internal camera delay Δt_{delay} deteriorates the range precision by

$$\Delta r_{delay} = \frac{c}{2n} \Delta t_{delay} , \tag{4.6}$$

where c is the speed of light and n is the refractive index. In the air the range is biased by 15 cm per 1 ns change in the internal electronic camera delay.
The range resolution is considered as the ability to separate two distinct points in range within the field of view of a single pixel, which is in agreement with (some of) the literature, [Fox, 1996]. The range resolution cannot be determined from the range image. One way to consider the range resolution is that the points should be separated by the distance corresponding to the depth of the range gate, i.e. 15 cm in air and 11 cm in water with a camera gate time of 0.5 ns and laser pulse time of 0.5 ns.
The target deformation is considered as incorrect reproduction of the general shape of the three-dimensional target. The target deformation may be determined from the range image if any knowledge or information is available about the target shape. For example most human beings posses knowledge about the three-dimensional shape of the human face.
The three-dimensional gated viewing laser radar image of the doll's head is shown in Fig. 4-4. The three-dimensional image was recorded in the laboratory under good conditions with plenty of laser power, good signal to noise ratio, and minimal medium disturbance like turbulence and scattering. The target deformation is minimal and only the outstanding parts of the eyes are noteworthy. The range accuracy is excellent and less than a millimeter. The high range accuracy of the gated viewing three-dimensional laser radar system composed of the pulsed laser and the intensified fast gating CCD camera is not seen before in the literature of gated viewing laser radar systems. The reports about object detection and three-dimensional laser radar imaging present range resolution about 5 cm [Dries et al. 2004], range resolution 2-3 cm [Gleckler et al. 2001], millimeter to centimeter object detection [Saade et al. 1994].

In general it is my opinion that there is a confusing use of the concepts of range accuracy, range resolution, and range precision in the literature. Therefore I consider the concepts of range accuracy, range precision, range resolution, and target deformation as valuable for characterization of the three-dimensional laser radar performance. It is not a matter of using "accuracy" or "resolution" or "precision", but it will make the literature easy to read and compare if researchers in the field use a standard set of well defined concepts.

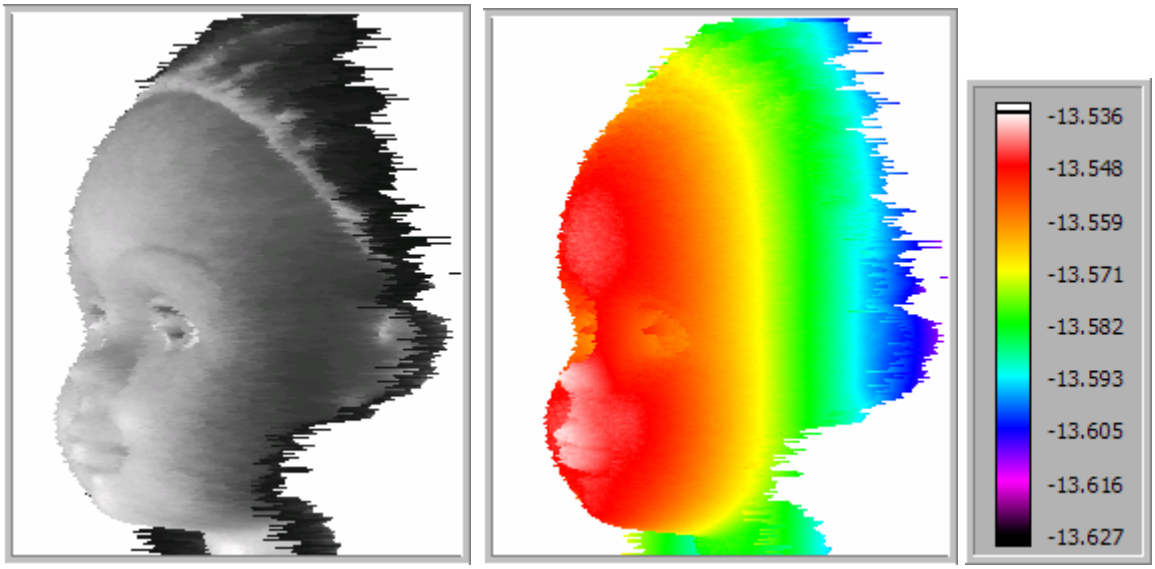

Fig. 4-4 Left: Three-dimensional range image with overlaid contrast. Right: Color-coded range image with color-coded range scale in meters. Range accuracy is better than a millimeter.

The gated viewing three-dimensional laser radar imaging requires a proper elimination of the image noise background to get high range accuracy. If the background noise is not properly eliminated the effect on the gated viewing three-dimensional laser radar images is a complex distortion of the three-dimensional shape of the object.

Figure Fig. 4-5 shows a simulated plot of two pixel profiles, i.e. the pixel values of two pixels in a sequence of 50 images. The abscissa (x-axis) is the image number and the ordinate (y-axis) is the pixel value or pixel intensity in 8 bit units 0-255. Recall that the range is found by calculating the average image number weighted by the pixel values. The conversion from image number to range was explained in Sec. 4.2 above. A bias in average image number leads to a bias in range.

In Fig. 4-5, the arrows “A1” and “B1” indicate the weighted average image number of the red points and the blue points, respectively, before subtraction of the noise background. The arrows “A2” and “B2” indicate the corresponding average values after subtraction of the noise background. The average image number bias is of opposite sign for the two pixels, i.e. background noise biases the average image number toward the center of the sequence. The average image number bias is dependent on the maximum value of the pixel values in the sequence, i.e. |”A2” – “A1”| > |”B2” – “B1”|. Thus it is concluded that an incorrect background subtraction can corrupt the three-dimensional image considerably.

The image noise background can either be eliminated by image processing or by change of the black and white levels on the frame-grabber. For more details on the image background see App. B.

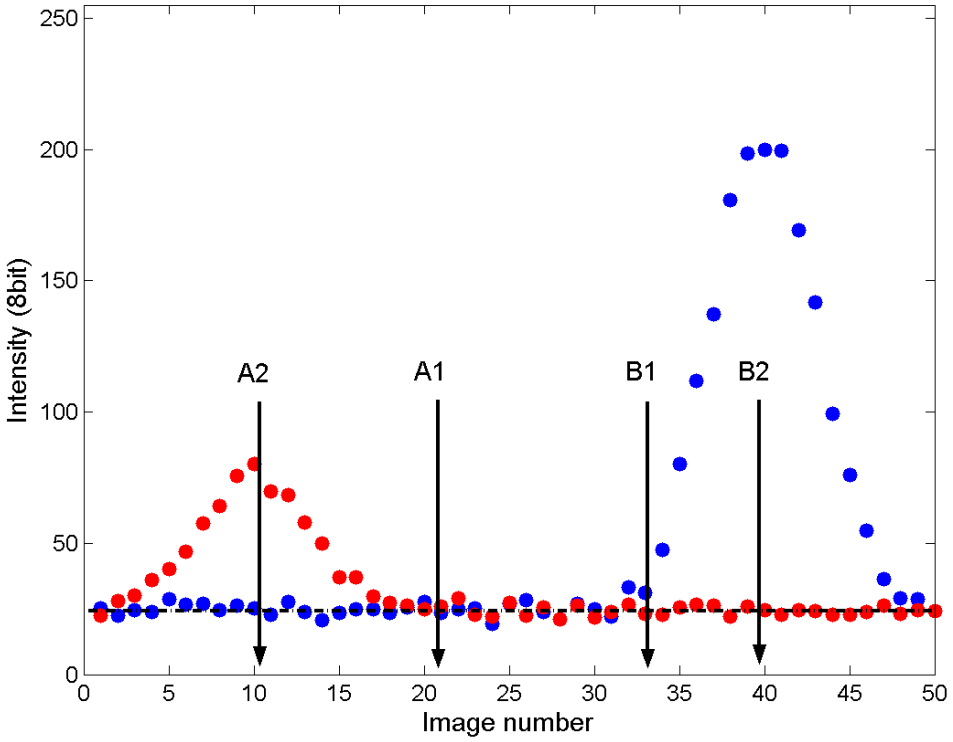

Fig. 4-5. Simulated pixel intensity for two pixels in an image sequence of 50 images.

The orientation and distribution of the reflection points within the field of view of a single pixel are among the variables that determines the shape of the pixel profile. The target shape impulse responses for a cone, a sphere, a paraboloid, and a cylinder have been reported, [Steinvall, 2000]. To illustrate how the reflectivity of a point can affect the symmetry of a pixel profile, the range gating of two boxes are illustrated in Fig. 4-6. If the reflectivities of the two boxes are equal the pixel profile is symmetric. If the reflectivity of the box to the right is lower than the reflectivity of the box to the left, the pixel profile becomes asymmetric, illustrated by the gray circle, Fig. 4-6. The symmetric pixel profile leads to the determination of the average range to the boxes, while the asymmetric pixel profile leads to a bias in range towards the closer box. It is concluded that the range to the points within a single pixel field of view, computed by the weighted average of the pixel profile, is in favour of the points that reflects more light. Anyhow, the favourization of the stronger reflecting points are negligible for the underwater sea-mine identification and the general applications presented here, because of the high angular resolution of the laser radar.

If the time profile of the laser pulse is asymmetric, which has been suggested in the literature, [Steinvall, 2000], then the pixel profile becomes asymmetric affecting the range precision. If an inherent asymmetric pixel profile is amplified above the level of saturation, then it affects the range determination, because the largest values of the profile are fixed at the saturation value. A pixel is said to be saturated when the pixel value is at the maximum of 255 units of 8 bit (0-255). Note that pixel saturation is not the same as detector saturation. The image pixel value is determined by the black- and white-level

settings of the analog-to-digital converter of the frame-grabber, which is placed in the computer. Three pixel profiles of a flat white board at 5 m range are shown in Fig. 4-7. Profile 1 (blue triangles), profile 2 (red crosses), and profile 3 (green circles), are recorded with the camera gain voltage of 320, 350, and 400 V, respectively. Note that the camera gain is not linear in the camera gain voltage, (App. A). Camera gate time is 0.4 ns and the delay step is 0.1 ns for all three profiles. The image background has been subtracted. The weighted mean image number < i > for each profile is shown in Table 4-1. The higher the gain voltage of the profile the smaller the weighted average image number < i >. The deviation in < i > leads to a deviation in the range (see Eq. 4.2, Sec. 4.2 above). For example, consider profile number one to represent the correct image mean number, the profiles two and three are off by (25.2-26.0)×1.5 cm = –1.20 cm, and (24.3-26.0)×1.5 cm = –2.55 cm, respectively. The saturation of several neighboring pixels causes target deformation, for example the saturated pixels of the eyes of the doll in Fig. 4-4. There is a trade-off between the need to amplify the low signal image pixels and the need for a reduction of signal in the saturated pixels to prevent image deformation. A source of error is the variation in the internal camera delay.
How the amplitude of the pixel profile and the background subtraction affect the weighted average image number can be summarized

$$\langle i \rangle = \sum_{i=1}^{N} i\big(Ap(i) - B\big) \Big/ \sum_{i=1}^{N} \big(Ap(i) - B\big), \tag{4.7}$$

where < i > is the weighted average image number i of an image sequence, A is the pixel profile amplitude and depends on target reflectivity, camera gain, etc., p(i) is the range gated laser pulse, and B is the background.
The expression Eq. 4.7 tells how the three-dimensional image is affected by the environment and the laser radar system settings. For example, if the gain is increased the amplitude A of the pixel profile is increased and the weighted average image number <i> is altered, and therefore the range is altered according to Eq. 4.2. For example, if the reflectivity of the target changes, the target will not be imaged three-dimensionally correct, because the amplitude A of the pixel profile changes with the target reflectivity. It is concluded that the quality of the three-dimensional image, i.e. the reproduction of the true three-dimensional target shape, depends on the target characteristics, the environment (e.g. turbulence), and the laser radar system settings. An ideal case arises if B is equal to zero in Eq. 4.7.
The gated viewing technique for three-dimensional image formation has a disadvantage concerning the utilization of reflected laser pulse radiant energy, not all the laser pulse radiant energy reflected at the target is recorded in the individual images of the image sequence, because of the short range gate, i.e. some of the laser pulse radiant energy reflected at the target is gated out and lost. The amount of energy lost varies from image to image and depends on the depth of the range gate and the size and shape of the target.

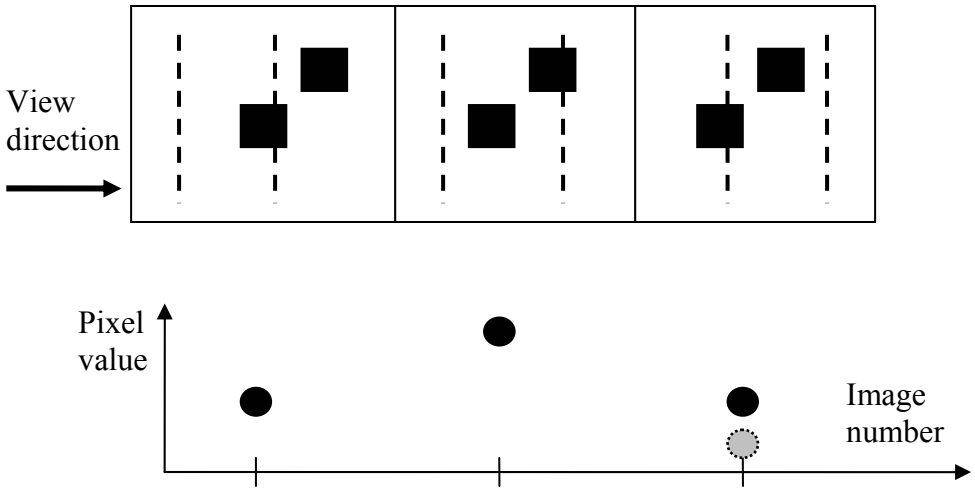

Fig. 4-6 Top: The range gating of two boxes in the field of view of a single pixel. The depth of the range gate is illustrated by the stippled lines. Imagine the gated viewing laser radar located to the left of the paper, i.e. the line of sight is from left to right. Bottom: The corresponding pixel profile. If the reflectivities of the two boxes are equal the pixel profile is symmetric, (i.e. the black circles are symmetric). If, for example, the reflectivity of the box to the right is lower than the reflectivity of the box to the left, the pixel profile becomes asymmetric illustrated by the gray circle.

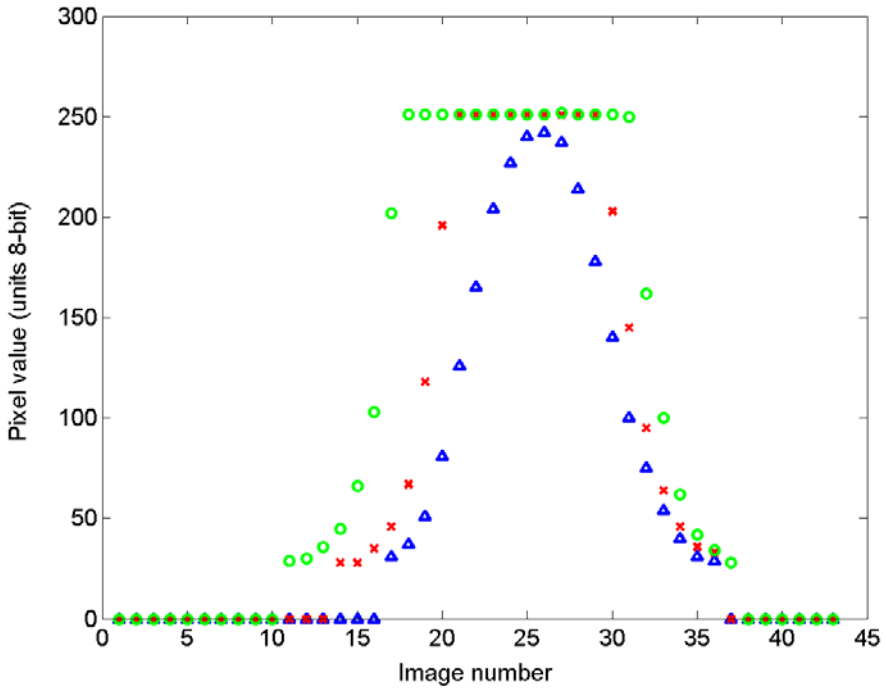

Fig. 4-7 Three pixel profiles of a flat white board at 5 m range. Profile 1 (blue triangles), profile 2 (red crosses), and profile 3 (green circles) are recorded with the camera gain voltage of 320, 350, and 400 V. The camera gate time is 0.4 ns and the delay step is 0.1 ns for all three profiles.

Profile	Camera gain voltage (V)	Weighted mean image number <i>
1	320	26,0
2	350	25,2
3	400	24,3

Table 4-1. The weighted mean image number < i > for the three pixel profiles of Fig. 4-7. Note that the gain of the pixel profiles is not linear in camera gain voltage.

4.4 Analysis program for three-dimensional imaging

In this section the analysis program is described. The analysis program is the second of two Labview programs applied to record and compute the three-dimensional images. The computations done by the program has been outlined above and in the literature, [Busck et al. 2004a]. In short the program loads an image sequence, computes the weighted average image number and converts it into range. The analysis program can either be called directly from the recording program (Sec. 3.2 above), or opened individually for analysis of older image sequences. It takes about 30 s on a 2.4 GHz laptop to process an image sequence of 50 images in the file format: Portable Network Graphics (PNG). The program corrects the range for camera gate time, the internal electronic camera delay, the optical fiber length and refractive index, the medium refractive indices for combined path length in air and water. The analysis program interface with the two-dimensional contrast of the image sequence in the lower left corner and the three-dimensional image, which can be rotated by the computer mouse, is shown in Fig. 4-8.

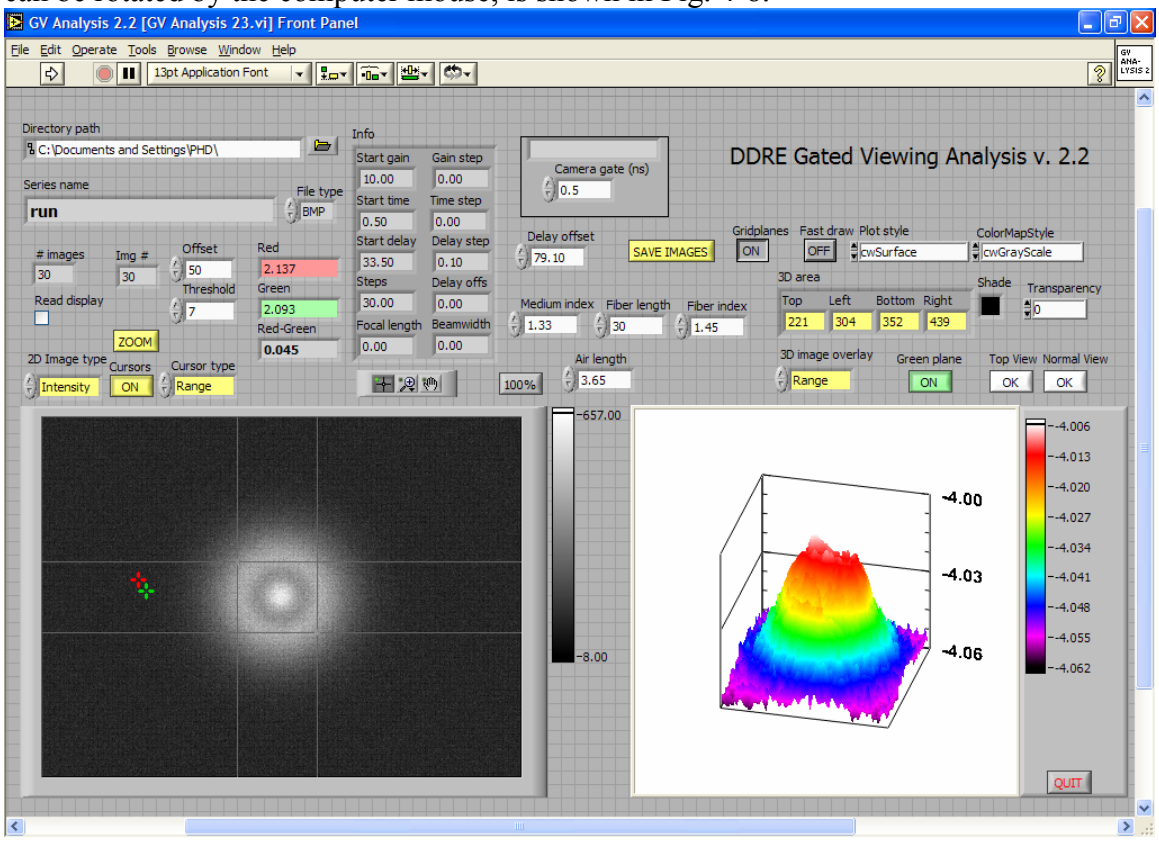

Fig. 4-8. Interface of gated viewing three-dimensional image analysis program. The analysis program processes the range gated image sequence and computes the three-dimensional image.

4.5 Summary and conclusion

A novel algorithm for three-dimensional image formation has been presented. It is the first time such high accuracy three-dimensional images are recorded with the gated viewing laser radar. The three-dimensional image is computed by the algorithm by taking the weighted averages of the pixel profiles of the recorded image sequence. An image sequence of 50-100 images can be recorded in a few seconds time. That should be a sufficiently short period for an underwater remote operated vehicle to stand still, while recording. The three-dimensional image is computed in 30-45 s time by processing the image sequence. The short computation time is an advantage. It is concluded that the time needed for computation of a three-dimensional image is feasible for the gated viewing laser radar to be implemented in an underwater remote operated vehicle. Range accuracy, range precision, range resolution, and target deformation have been discussed. Error sources that deteriorate the three-dimensional image have been discussed, for example the error source of incorrect background subtraction, which can worsen the range precision and cause target deformation. A disadvantage of the gated viewing three-dimensional imaging technique is the waste of laser pulse energy, i.e. some of the reflected target photons are gated out because of the narrow range gate. It is concluded that the quality of the three-dimensional image, i.e. the reproduction of the true three-dimensional target shape, depends on the target characteristics, the environment (e.g. turbulence), and the laser radar system settings. The advantages of the algorithm for three-dimensional image formation are that it is relatively fast, simple to implement, and produces fine three-dimensional images.

5 Applications of gated viewing three-dimensional laser radar imaging

In extension to the tests and experiments of Chap. 3, which were focused on the ability of the gated viewing laser radar to eliminate backscatter, experiments are presented in this chapter with the purpose of testing the three-dimensional image capabilities of the laser radar at different ranges and different targets. Some of the targets are chosen for a specific purpose, for example the sea-mine dummies are chosen for their simplicity being easy to simulate digitally. The vehicles as laser radar target were chosen by inspiration from the literature, [Steinvall et al. 2003; Albota et al. 2002; Schilling et al. 2002; Gleckler, 2000], and for the general military purposes of detection, classification and identification of vehicles. The antenna cluster was chosen as the most obvious of the long range targets available at the location. A laboratory three-dimensional image experiment was done at the range of roughly 10 m, which is comparable to the expected range for the underwater application. The result of the laboratory experiment, which was done in air, gives an overestimated upper bound on the underwater performance, because of the scattering and absorption in water. It is expected and experimentally confirmed that the performance underwater is considerable worse than the performance in air, (Chap. 6 below).

A high and low contrast experiment is presented in Sec. 5.1. In Sec. 5.2 the potential for three-dimensional face recognition is presented. The face recognition experiment shows that the gated viewing three-dimensional laser radar imaging by weighted average has a wide potential with excellent high accuracy images. In Sec. 5.3 long range (1 km) three-dimensional imaging of an antenna cluster is presented. The long range three-dimensional imaging in air is interesting in itself and for airborne underwater mine identification. Very long range (7 km) gated viewing three-dimensional imaging of military vehicles is reported in the literature, [Klasen et al. 2004].

5.1 High and low contrast

Three-dimensional laser radar systems are better off identifying objects and their shapes, than two-dimensional laser radar systems, [Nevis et al. 2003, 2002; Nevis, 2003]. The range adds valuable information to the optical identification process. For example, consider the Manta sea mine with the shape of a truncated cone together with a car tire on a bright sandy bottom. The car tire and the manta are imaged as a black disk with a bright circular spot in the middle by the two-dimensional laser radar system. Exceptionally the presented gated viewing laser radar system is able to correctly identify and distinguish the objects by two-dimensional images, because the range gated images allows for discrimination of the reflections from either the top or the bottom of the objects. The three-dimensional laser radar system will clearly see that the center of the manta mine rises up from the bottom and that the center of the car tire does not.

For the trial of contrast two miniature Manta sea mines is chosen. The size of the dummies is 12.3 cm in width and 5 cm in height. They are glued to a flat piece of wood, which is covered with sand. One of the dummies is camouflaged with sand. A digital image of the target is shown in Fig. 5-1. At 532 nm the reflectivity coefficients of the

dark and the sandy dummies are 0.12 and 0.33 respectively. The contrast for the dark and the sandy dummies are 47 % and 0 %, (Sec. 6.4 below). The contrast of 0 % made the sandy dummy invisible if it was not for the slope from the top to the bottom of the dummy. The slope reflects less radiant energy and therefore the effective contrast of the slope is higher than 0 %. In general the effective contrast depends on the shape and the orientation of the objects and not only on the reflectivity of the surface texture. The laser illuminated contrast image of the dummies is shown in Fig. 5-2, left. In spite of the higher reflectivity the sandy dummy is harder to recognize than the dark one. Two-dimensional target recognition depends on object contrast. The range image is shown in the middle of Fig. 5-2. In the range image the two dummies are recognized with equal ease. The corresponding three-dimensional image is shown in Fig. 5-2, right. It is emphasized that the tilt of the sandy foundation can not be recognized in the left image, hardly in the middle image, but clearly in the right three-dimensional image. It is a great advantage of three-dimensional images that they can be rotated in the computer.

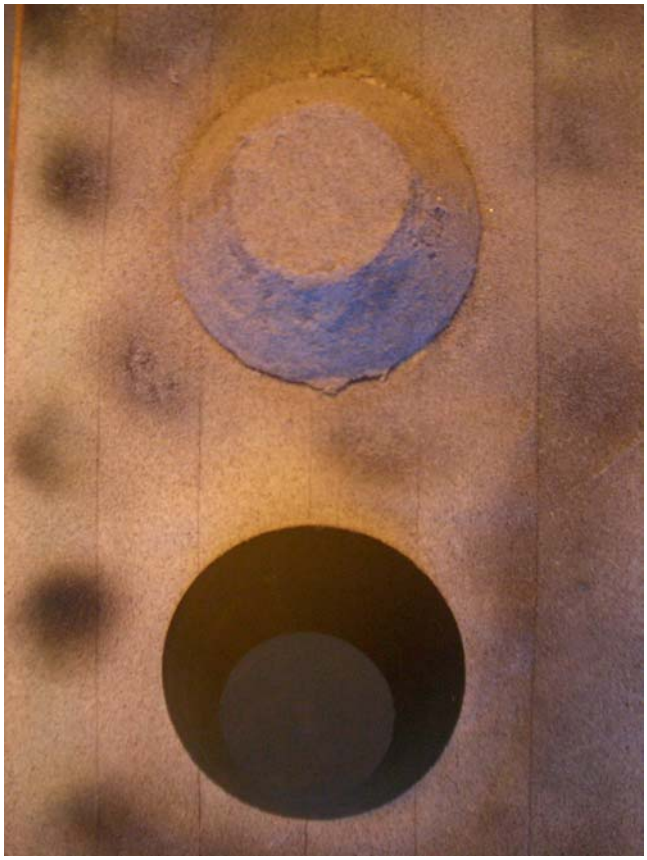

Fig. 5-1. Digital image of the two miniature sea-mine dummies, where the top one are camouflaged with sand. The image is recorded with an amateur digital camera with 4 mega-pixels.

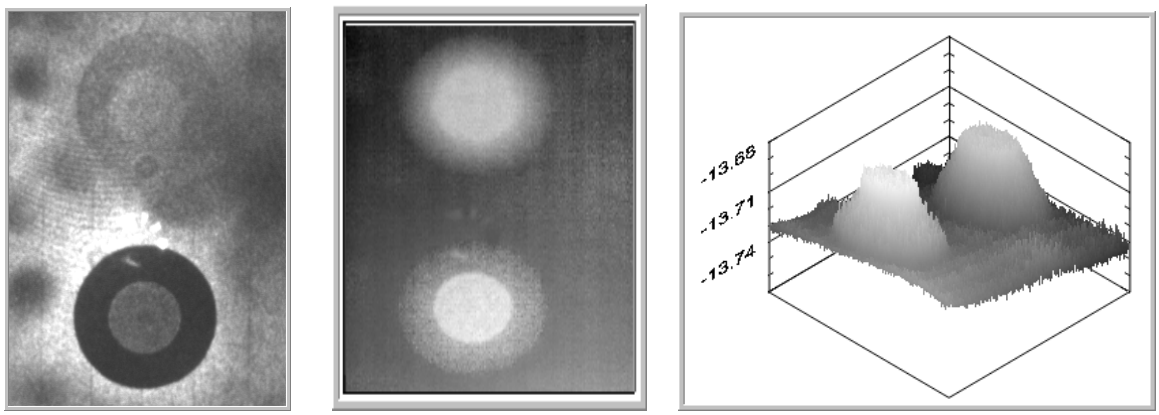

Fig. 5-2. Left: Laser illuminated contrast image of the two dummies. Middle: Corresponding range image, the brighter the closer. Right: Corresponding three-dimensional image. Notice the tilt of the sandy foundation can not be recognized in the left image, hardly in the middle image, but clearly in the right three-dimensional image. (The tilt of the foundation arises from the fact that the object set-up was resting up against the wall).

5.2 Face recognition and person identification

The image recording part of face recognition is related to the thesis as an application of the gated viewing three-dimensional laser radar. A close up color image of the doll recorded with an amateur digital camera is shown in Fig. 5-3. The doll has two advantages for exploration of the gated viewing three-dimensional laser radar performance. First the face of the doll is easily recognized by everyone. Second the doll resembles a small human face and can be used for face recognition research without worries about safety issues. The laser radar contrast image and the three-dimensional image recorded at roughly 10 m range with 500 mm focal length camera optics are shown in Fig. 5-4. The camera gate time is 0.4 ns and the delay step is 0.1 ns.

The telescopic face recognition trial is set up at the Danish Defence Research Establishment. The doll is placed outside at 207 m range and the camera optics is replaced by the 14 inch Celestron telescope with 4 m focal length. The camera gate time is 1 ns and the delay steps are 0.1 ns. The telescopic laser radar contrast image and the three-dimensional image are shown in Fig. 5-5. The range accuracy is excellent. The features of the face below the eyebrows are well reproduced, but the forehead is deformed and conspicuous. The deformation of the forehead may be caused by the strong reflecting box which the doll was resting on. The box reflects light onto the forehead and disturbs the pixel profiles of the forehead of the recorded image sequence.

The images display a pattern of interference caused by interference of the laser light. The interference pattern could be eliminated by a frequency filter that filters out the frequency of interference. The frequency filter should be applied to the individual images of the recorded image sequence. A weak beehive pattern can be recognized, (see the forehead of the doll in Fig. 5-5). The beehive pattern is caused by the camera and is more likely seen in long exposure images recorded in ambient light. However the beehive pattern disturbance is weak and can be ignored.

Fig. 5-3. Digital image of the doll, (4 mega pixels).

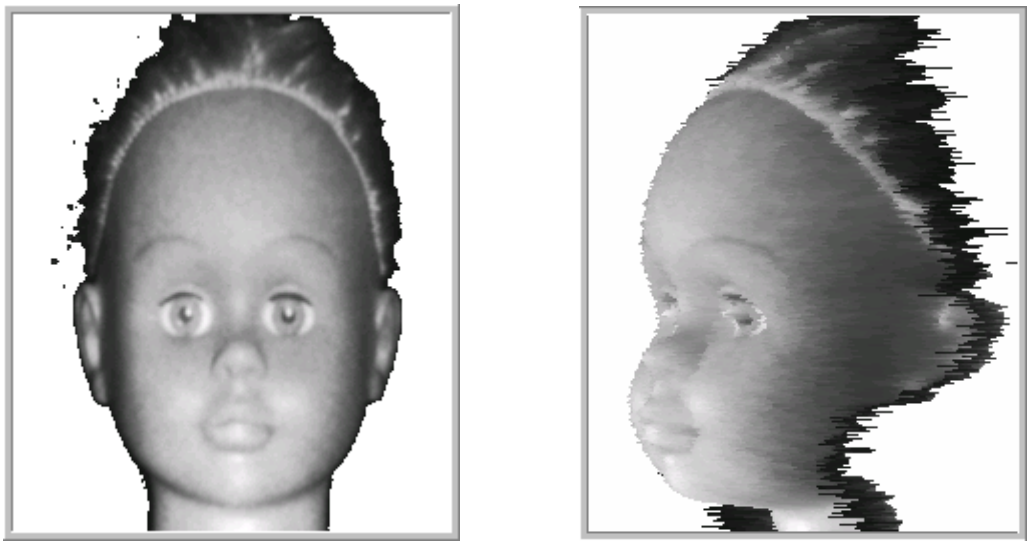

Fig. 5-4. Gated viewing three-dimensional laser radar image at roughly 10 m range recorded with 500 mm camera optics.

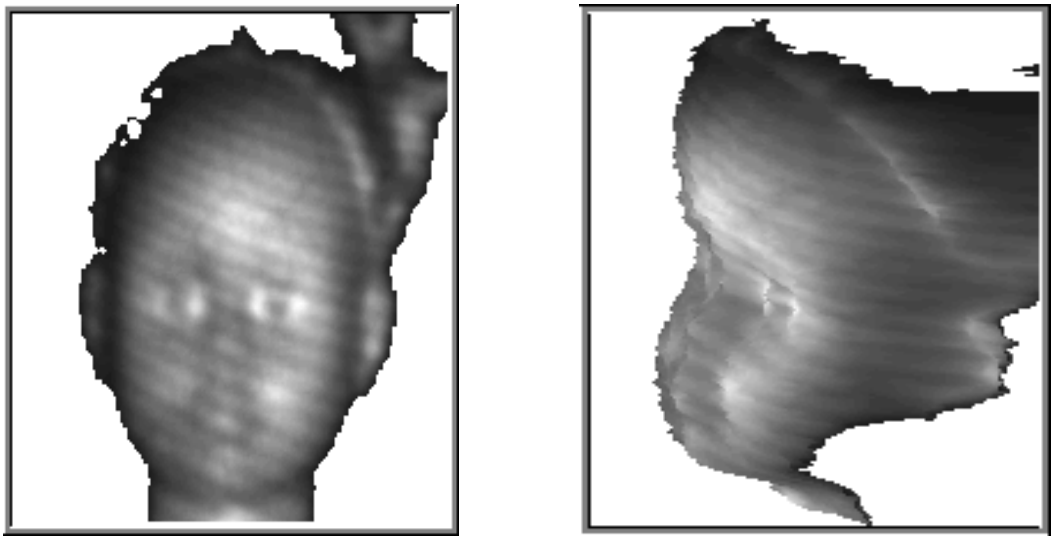

Fig. 5-5. Gated viewing three-dimensional laser radar image at 207 m range recorded with the telescope.

Three-dimensional face recognition may be based on a geometric algorithm that computes a set of distances from some recognizable features in the face, for example the distance from the nose to the chin. The algorithm is then independent on the orientation of the face. The x and y ranges is computed by knowledge of the camera resolution and the z range by gated viewing three-dimensional imaging, where the z-axis is along the line of sight. Analog to the face recognition a similar algorithm based on three-dimensional imaging could be developed for underwater optical sea-mine identification.
Experimental research on telescopic person identification at long distances is reported, [Andersen et al. (sub.2005)].

5.3 Long range imaging (1 km)

The gated viewing laser radar is extended with the 14 inch telescope for long range application. The long range three-dimensional imaging could be interesting for airborne shallow water sea-mine identification. The antenna cluster presented in this section is roughly $(1.5\ \mathrm{m})^2$ and comparable to the size of a sea-mine. The view of the antenna cluster at 1 km range and a closer up view (by camera zoom) are shown in Fig. 5-6. The color-coded telescopic range image of the antennas is shown in Fig. 5-7. The antennas are recorded with the camera gate time 1 ns and the camera delay step 0.1 ns. The range accuracy is 1-3 cm.
One source of image degradation is image blurring by vibration. Small vibrations in the foundation, (the third floor of the Danish Defense Research building), are observed to propagate into the laser radar system. The vibrations can be caused by people moving around, air-condition systems, strong wind, etc. Second source of image degradation can be cells of water vapor drifting in from the sea, causing the target to drift in and out of focus. Third source of image degradation is atmospheric turbulence.

Fig. 5-6. Left: Amateur digital image of antennas to the left of the chimneys on top of the local power plant. Right: Closer look at the antennas by the zoom of the amateur camera.

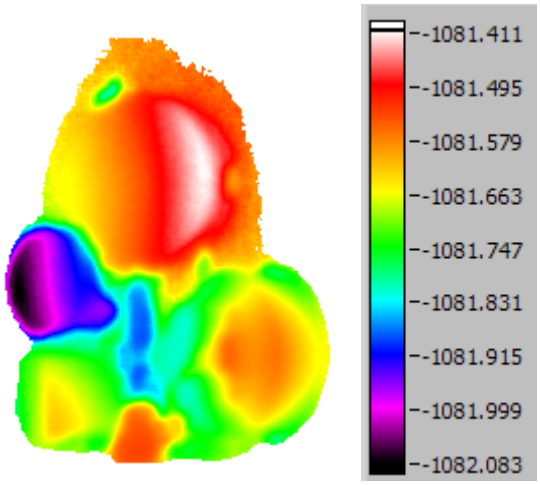

Fig. 5-7. Range image of the antennas recorded with the 14 inch telescope. The width and height of the antenna cluster is about 1.5 m. The range is color-coded and the range scale is in meters. The range accuracy is 1-3 cm.

5.4 Three-dimensional images of vehicles

This section presents experiments and results that are part of the general testing of the imaging capabilities of the gated viewing laser radar. It has more or less become a standard to test the three-dimensional laser radar imaging on man-driven vehicles. A number of three-dimensional images of vans, cars and other vehicles have been reported, [Steinvall et al. 2003; Albota et al. 2002; Schilling et al. 2002; Gleckler, 2000]. It was tempting to test the gated viewing three-dimensional laser radar on a vehicle making a quick comparison with the reported results. It is concluded that the gated viewing three-dimensional laser radar images compare well with the results reported elsewhere and in general with better accuracy. A van is recorded at 110 m range with 500 mm camera objective. Records revealed the interior of the van is displayed three-dimensionally, Fig. 5-8. The range accuracy is a few centimeters. The light bulbs of the front light can be seen in the range image. When looking through the windows it is possible to determine the range to people and objects behind the van. This could be interesting for the anti-

terror applications. The van is recorded at the Danish Defence Research Establishment during daytime. The sunlight is filtered out by the technique of gated viewing and by a 10 nm narrow optical band-pass filter. The three-dimensional gated viewing laser radar image of a military vehicle painted in camouflage colors is shown in Fig. 5-9. The vehicle is recorded at 95 m range in the coastal area of Oksbøl, Denmark, 2002. The thin layer of ice on the windows prevents three-dimensional imaging of the interior of the vehicle.

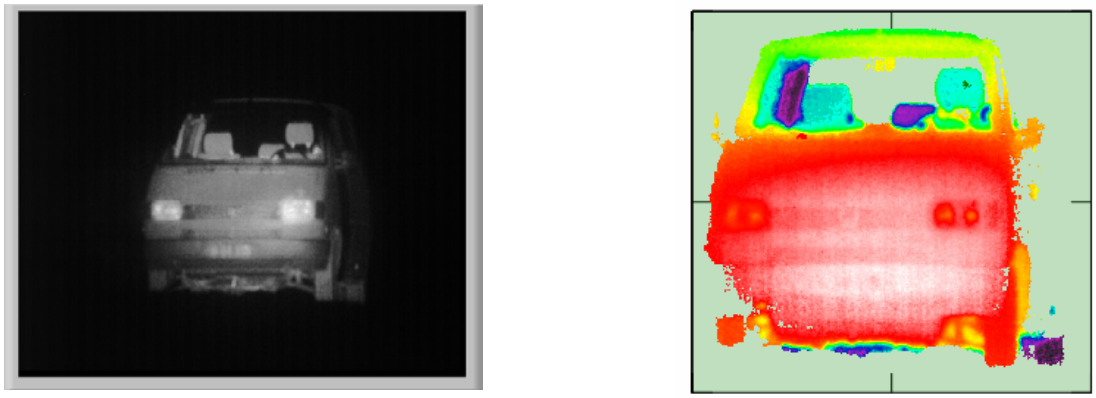

Fig. 5-8. Left: Laser illuminated Van at 110 m range. Right: Three-dimensional gated viewing laser radar image. For example, note the driver's wheel. The experiment was performed at the Danish Defence Research Establishment in 2002.

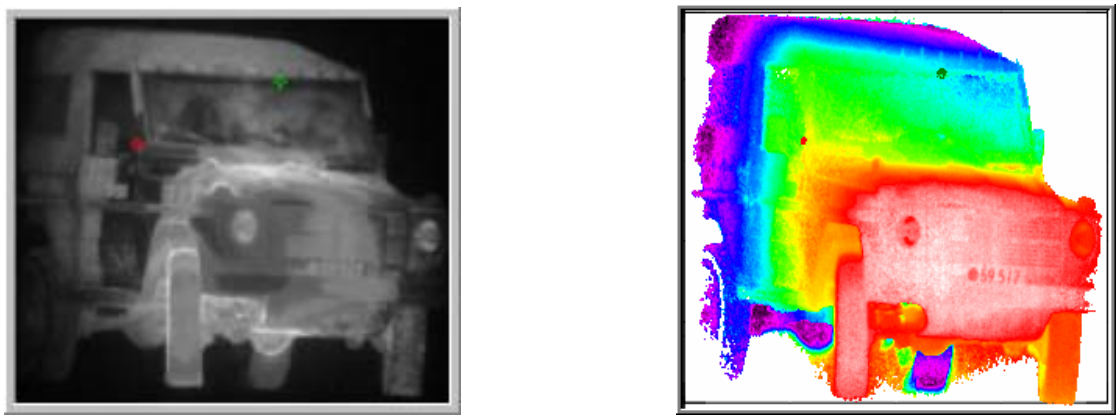

Fig. 5-9. Gated viewing three-dimensional laser radar imaging of military vehicle painted in camouflage colors. The range is about 95 m. The image recording toke place during nighttime at the coastal area of Oksbøl, Denmark, 2002.

5.5 Summary and conclusion

It is concluded that the gated viewing weighted average three-dimensional laser radar has a great potential in a wide variety of applications ranging from long range object recognition to face recognition. Three-dimensional face recording by the gated viewing laser radar has been presented at short range (10 m) and medium range (200 m). The potential for underwater sea-mine recognition is discussed in the next chapter, (Chap. 6 below).

In general, the high accuracy of the gated viewing three-dimensional laser radar is achieved by improved signal to noise ratio by the high repetition rate of the pulsed laser and the fine control of camera gate time, which reduces the backscattering noise. The image signal to noise ratio is improved by a factor of 25 by integration of the many laser pulses. The range accuracy is improved by the same factor of 25 to an optimal accuracy of 1 mm at 10 m range with a 500 mm camera objective. For a given camera objective the range accuracy increases approximately by the same factor as the signal to noise ratio decreases. A three-dimensional telescopic laser radar image with the range accuracy of 1-3 cm at 1 km has been presented. The great advantage of three-dimensional imaging over two-dimensional imaging in low contrast applications has been demonstrated. The sources of three-dimensional image degradation have been discussed in the concluding remarks of the previous chapter, (Chap. 4 above).

6 Underwater three-dimensional gated viewing

To the best of my knowledge (Jan. 2005) this thesis is the first in the literature to report on underwater three-dimensional gated viewing laser radar imaging with the system configuration described in the previous chapters. There are alternative underwater laser radar systems, but they apply different techniques as described in Chap. 2 above. The laser line scanner can provide high-resolution optical images as shown in Fig. 2-5, but no three-dimensional underwater images have been reported. The laser line scanner utilizes the method of spatial separation to minimize the common volume between the field of illumination and the field of view. Also there are reports on the development of a modulated laser line scanner, e.g. [Mullen et al. 2004], and modulated pulsed laser radar, [Pellen et al. 2001, 2000; Mullen et al. 2000, 1996; Lagaye et al. 1997], there are no reports on three-dimensional images recorded by the modulated laser radars. The streak tube imaging lidar is promising and delivers both two- and three-dimensional images from the same data, [Nevis et al. 2003, 2002; Nevis, 2003; Gleckler et al. 2001; Gleckler, 2000, 1999; McLean et al. 1998]. The streak tube imaging lidar separates the reflected target signal from the backscatter noise by sweeping the received light across the detector array, thus achieving a good range resolution. In general the literature is very spares on reported underwater laser radar images. The first reports on underwater gated viewing two-dimensional laser radar with a CCD-camera, are from the early 90'ties, [Fournier et al. 1993; Swartz et al. 1991].

This chapter is the final chapter explicitly dedicated to the testing and evaluation of the gated viewing three-dimensional laser radar applying the algorithm of weighted average. The previous chapters have concentrated on describing the components of the laser radar, the technique of gated viewing, the algorithm for three-dimensional imaging, test and evaluation of the performance and applications in the air. With the knowledge acquired in the previous chapters this chapter is then to present the experiments and results of underwater gated viewing three-dimensional laser radar imaging, which are more closely related to the underwater optical identification of sea-mines.

The absorption, scattering and exponential attenuation are the main obstacles for underwater imaging, when the laser radar is submerged. Laser radar imaging from the air and into the water faces the challenge of seeing through the complex and turbulent air-water interface, [McLean et al. 1996]. Platform stability is another issue if the gated viewing laser radar is to be applied for airborne three-dimensional imaging. Anyway, airborne three-dimensional imaging is beyond the scope of this thesis, but platform stability is still an issue if the gated viewing laser radar is to be applied in an underwater remote operated vehicle.

Refraction in the air-water interface is described in Sec. 6.1; underwater attenuation is discussed in Sec. 6.2-6.3. An underwater contrast experiment, results and error sources are presented in Sec. 6.4. The underwater gated viewing three-dimensional laser radar experiment is presented in Sec. 6.5. Summary and conclusion is given in Sec. 6.6.

6.1 Refraction in air-water interface and image resolution

In this section the refraction in the air-water interface and the effect on image resolution is discussed. Thus this section is concerned with the interplay between the field of view

of the laser radar system and the refractivity of the medium. The refractive index of water n = 1.33 for essentially all natural waters and wavelengths, [Gierloff et al. 1986]. The refractive index of air is assumed unity. A ray of light crossing the air-water interface is refracted according to Snell's law, Fig. 6-1.
Consider the camera with focal length f_0 and half-angle field of view θ_0, is placed on the optical axis a distance r_0 from the air-water interface, Fig. 6-2. If the line of the refracted ray corresponding to the angle θ_0 is followed back into the air, then the optical axis is reached at the distance r_1 from the air-water interface. The geometry gives the distance $r_1 = nr_0$ and the angle $\theta_1 = \theta_0/n$. Consider the general relation between the focal length f, the angle θ, and the detector radius r_d, i.e. $\theta = r_d/f$, then $f_1 = nf_0$, where f_1 is the (pseudo-) focal length of the camera optics corresponding to the angle θ_1. Thus the image resolution of imaging through the air-water interface with the camera optics focal length f_0 and the camera placed the distance r_0 from the interface, corresponds to imaging with the (pseudo-) camera optics focal length f_1 and the camera placed the distance r_1 from the interface and replacing the water with air. The water decreases the field of view and improves the image resolution of the laser radar system.

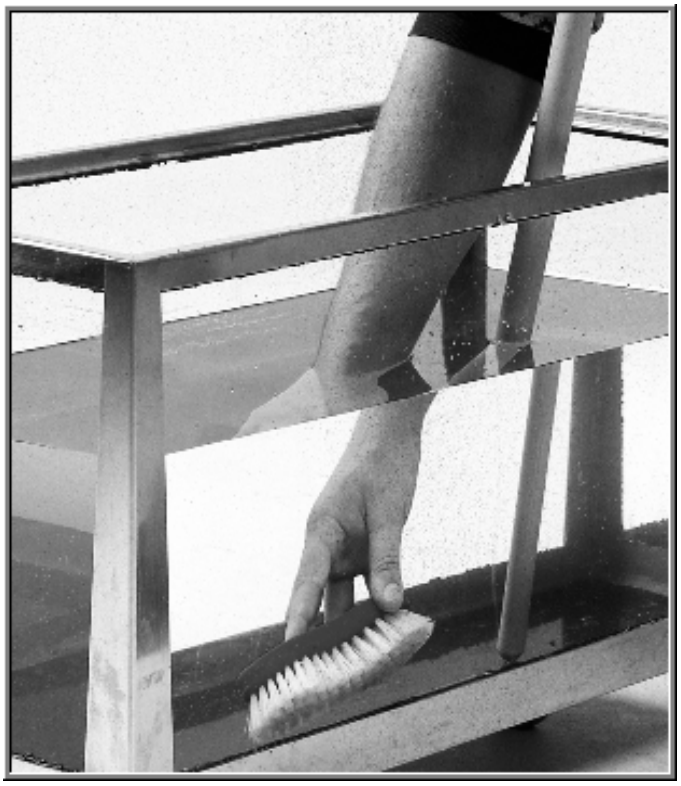

Fig. 6-1. Image of a hand cleaning the inside of an aquarium filled with water. The light rays are refracted in the air-water, the air-glass, and the glass-water interfaces. The arm and the stick look everything but straight, [Encyclopedia, 2004].

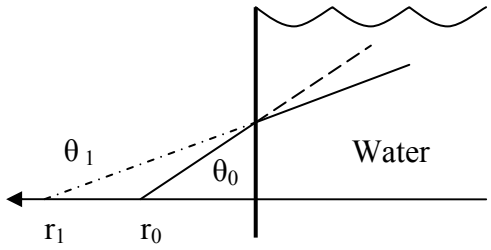

Fig. 6-2. Refraction in the air-water interface. The interface increases the image resolution corresponding to camera optics with focal length n times longer, where n is the refractive index of water.

Consider the detector radius in the horizontal- and vertical directions to be 6.4 mm and 4.6 mm, respectively, and the camera optics focal length 85 mm. The half angle field of view in the horizontal- and vertical directions are 75 mrad and 54 mrad. The number of detector elements in the horizontal and the vertical directions are 752 and 582, (Sec. 3.2 above). The angular image pixel resolution in the horizontal and the vertical directions is 0.1 mrad. Imaging through the air-water interface changes the angular image pixel resolution in the horizontal and the vertical directions to 75 μrad.
It should be mentioned that the laser field of illumination is also refracted in the air-water interface resulting in a decreased field of illumination.
It is concluded that imaging through the air-water interface magnifies the objects by refraction, which is an advantage in underwater sea-mine identification.

6.2 Range performance in water

In this section the underwater laser radar range performance is considered in relation to the exponential attenuation. Thus in this section the interplay between the available radiant laser energy and the medium attenuation is discussed.
Consider the exponential attenuation of radiant energy Q in water

$$Q(r) = Q_0 \exp(-\alpha r), \tag{6.1}$$

where r is range and 1/α is the attenuation length of the water.
Consider the arbitrary maximum range r_{max} given by the minimum received energy Q_{min} required for the laser radar to operate at that range

$$r_{\max} = \frac{1}{2\alpha} \ln\left(\frac{Q_0}{Q_{\min}}\right), \tag{6.2}$$

where Q_0 is the input energy and the ½ -factor tells that the laser pulse travels twice the range from the laser radar to the object.
For example, a change of the camera optics to one with shorter focal length will increase the pixel value in fewer target pixels. The amount of reflected radiant energy from the target is then shared by fewer pixels on behalf of a decrease in image resolution. Thus the

maximum range can be increased until Q_{min} is reached for the reduced number of target pixels.
If the laser power Q_0 can be doubled

$$r_{\max}(2Q_0) = \frac{1}{2\alpha}\ln 2 + r_{\max}(Q_0), \tag{6.3}$$

where $\ln 2/2 \approx 1/3$.
The expression Eq. 6.3 tells that doubling the laser power gives an increase in range by approximately 1/3 the attenuation length of the water, or equivalently the laser power should be increased eight times to increase the range by one attenuation length.
The maximum ranges in Eq. 6.2-6.3 are overestimates considering the laser radar equation for the gated viewing laser radar, [Busck, sub.2004]. The target reflection transforms the collimated laser beam into a spherical wave. The reflected wave is attenuated by the factor of $1/r^2$ of a spherical wave.
It is concluded that the exponential attenuation is a major limitation on the range performance of underwater laser radar imaging. Note that the maximum range discussed in this section should not be confused with the non-ambiguity maximum range determined by the laser pulse repetition rate discussed in Sec. 3.2 above.

6.3 Attenuation coefficient of the Raman scattered laser pulses

This section is concerned with the determination of the attenuation coefficient of water, which to a considerable extent determines the range performance of underwater laser radars according to the previous section.
The high peak power of 8.6 kW of the pulsed laser stimulates Raman scattering in the fiber. The stimulated Raman scattering is a nonlinear optical phenomenon [Agrawal, 2001; Stolen et al. 1984]. The Raman scattering broadens the spectrum of the laser pulses with additional Stokes peaks separated roughly 15 nm apart, Fig. 6-3. The water attenuation for the Raman scattered laser pulses is not readily determined in practice. Consider the Raman spectrum $R(\lambda)$ of the laser pulses and the water spectral attenuation coefficient $c(\lambda)$. The overall attenuation coefficient of the Raman scattered laser pulses

$$c = \frac{\int c(\lambda)R(\lambda)d\lambda}{\int R(\lambda)d\lambda}, \tag{6.4}$$

where λ is the wavelength, and the water spectral attenuation coefficient $c(\lambda)$ depends on the water type.
The spectral attenuation coefficient $c(\lambda)$ is the sum of the spectral absorption coefficient $a(\lambda)$ and the spectral scattering coefficient $b(\lambda)$, i.e. $c = a + b$. Thus expressions similar to Eq. 6.4 can be written for the absorption and the scattering coefficients. The spectral absorption for clear water is shown in Fig. 6-4. The optimal wavelength for transmission in water is the visible green-blue part of the electro-magnetic spectrum. The wavelength of optimal transmission depends on the water type. In general going from clear to turbid water the optimal wavelength shifts from the blue to green, i.e. towards longer

wavelengths. Recall the image of the two scuba divers in Fig. 1-3, Sec. 1.1. In severe turbidity the water can become yellowish.

It is concluded that the overall attenuation coefficient determination is complicated by the Raman spectrum of the laser pulses output from the optical single mode fiber. The estimation of the overall attenuation coefficient can be made by approximating the Raman spectrum by a low-degree polynomial fitting, for example.

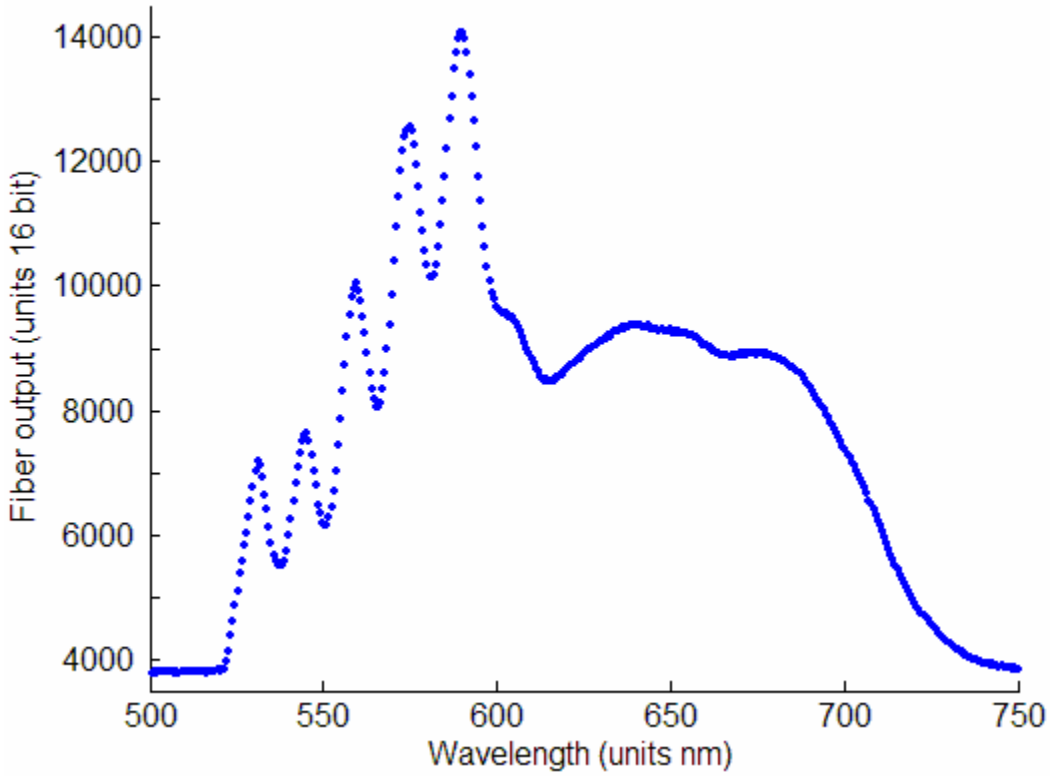

Fig. 6-3. Spectrum R(λ) of Raman scattered laser pulses output from the optical single mode fiber. The input wavelength to the fiber is the 532 nm laser output. The Stokes peaks are separated by roughly 15 nm. The ordinate axis shows the fiber output spectrum measured with a spectrometer. The units are 16 bit spectrometer counts, [Spectrometer manual, 1994]. (The Raman spectrum is measured with a spectrometer at the Danish Defence Research Establishment in 2004).

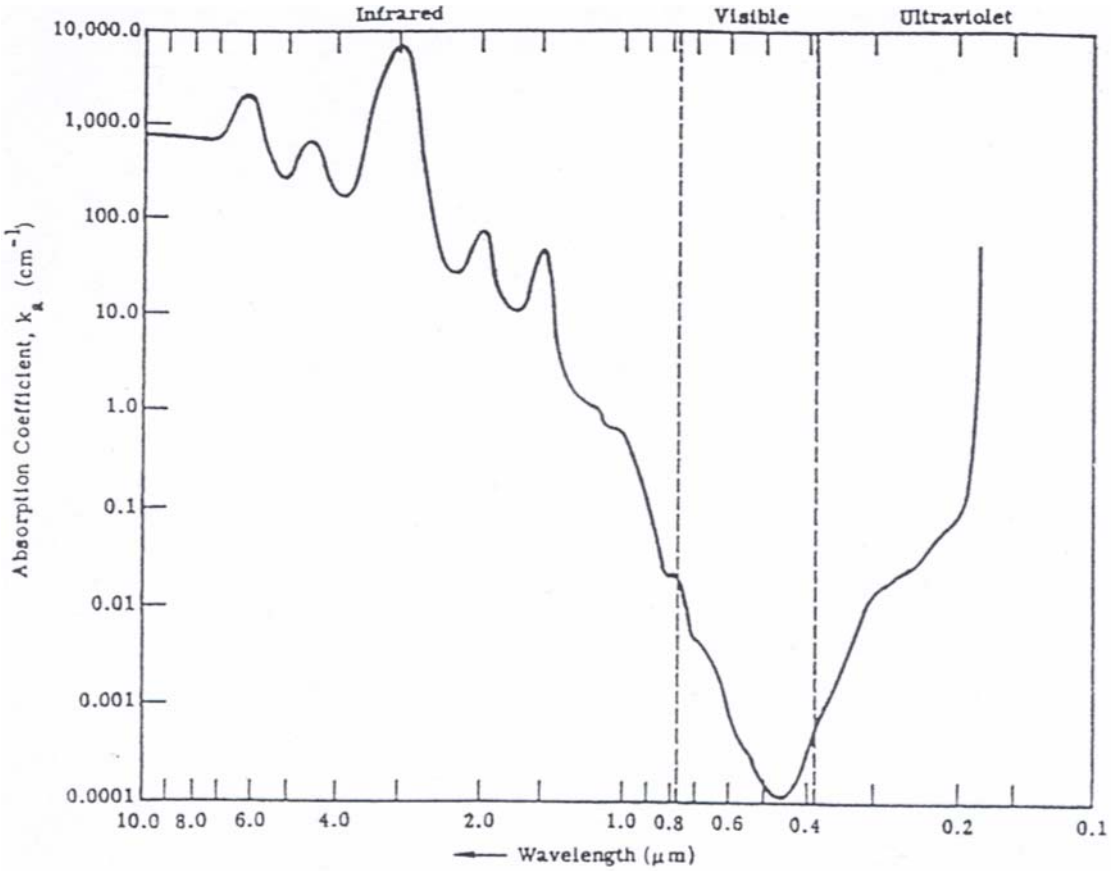

Fig. 6-4. Seawater spectral absorption of the infrared, visible, and ultraviolet parts of the electromagnetic spectrum. The minimum absorption is at the visible green-blue part of the spectrum. The minimum absorption is dependent on the water type. Note: Increasing wavelength from right to left. [Ewing, 1965].

6.4 Image contrast

This section is focused on evaluating the interplay between the gated viewing laser radar and the water by measurements of the image contrast. The image contrast is measured as function of range and water type. The contrast measurements were carried out at the Danish Defence Research Establishment in Nov.-Dec. 2004. The experimental set-up is described in Sec. 6.5 below.

The contrast, as considered in the expression Eq. 6.5 below, is a well known concept and widely used in laser radar applications, e.g. [He et al. 2004, 2002; Mullen et al. 2004; Sakai et al. 1998; Allwood et al. 1997; Bjarnar et al. 1991]. The contrast is also called "modulation depth", [Boreman et al. 1995]. Since the contrast is also called modulation depth it is tempting to ask what relation exists between the contrast and another widely used concept: "modulation transfer function". The modulation transfer function is a widely used concept in optics and imaging and is basically a description of the point spread function in frequency domain. The literature has several reports on laser radar imaging characterized by the modulation transfer function, and modulation transfer function derivation from bar-target measurements, (e.g. [Buskila et al. 2004; Rogers, 1998; Boreman et al. 1995; Sitter et al. 1995; Marchywka et al. 1992]). A method has been proposed for the measurement of the modulation transfer function of sampled

imaging systems from bar-target patterns, [Sitter et al. 1995]. Anyway the contrast is considered here to avoid possible aliasing effects and effects caused by higher harmonics of the Fourier transform, when measuring the modulation transfer function from bar-targets, [Sitter et al. 1995; Boremann et al. 1995].
The image contrast C is exploited for characterization of the underwater blurring by scattering of the recorded images. A set of black and white bar-targets with different spatial periods are used, Table 6-1.
The contrast

$$C = \frac{A_{\max} - A_{\min}}{A_{\max} + A_{\min}}, \tag{6.5}$$

where A_{max} is the white bar image value, and A_{min} is the black bar image value. For example the contrast of a sine wave is the ratio of the amplitude to the mean.
For the experiment the camera is optimally focused to sharpen the edges of the bars. The single mode Gaussian laser beam (TEM_{00}) is centered at the bar-target. The bar-target images depend both on the environment and the system settings of the laser, the camera, the camera optics, the gain value, and the black and white levels of the frame-grabber. The system settings are optimal in contrast when the white bars are as bright as possible with the black bars as dark as possible. One challenge of active illumination imaging with a Gaussian beam profile is the uneven illumination pattern.
The bar-targets numbered 3, 4, and 5 at 5 m range of seawater and recorded with the camera gate time 0.5 ns are shown in Fig. 6-5. All the bar-target images are recorded with a camera gate time of 0.5 ns. The short gate time eliminates backscattering. The short camera gate is identical with the gate time of the three-dimensional underwater image recording, (Sec. 6.5 below). The contrast is measured for each three-dimensional underwater image and with the short camera gate time the contrast is well adapted. To improve the signal to noise ratio the average of 100 contrast images are used. The image background is subtracted from the bar-target images. Incorrect background subtraction gives a systematic bias in the contrast. The underwater contrast at 3 and 4 m in tap water and 4 and 5 m in seawater is shown in Fig. 6-6. The contrast measurements at 3 m in seawater were prevented by technical problems with the internal electronics of the camera and the 5 m contrast in tap water has been excluded, because the data were corrupted by the ambient light field. In general the underwater laser radar experiments were done under a tremendous stress leaving no time to repeat the experiments, because of closing of experimental deadline.
It is obvious that the contrast goes to zero, when the bar-target period goes to zero. It is less obvious what happen to the contrast, when the bar-target period become large enough that the leakage by scattering no longer alters the center of the black bar. At first hand it would be expected that the contrast would increase to 100 %. As is clear from the contrast of 3 m tap water, (Fig. 6-6), the slope decreases, which can be explained by two things. First, some light is reflected from the black bar since it is not a perfect absorber. Second, the range gate of the laser radar is not perfectly narrow, and therefore some backscattering from the range gated water volume is recorded leading to a decrease in contrast. It is obvious that an unlimited increase in range results in zero contrast, because of photon limitation caused by attenuation.

To get a high bar-target contrast the black bar value should be as low as possible and the white bar value as high as possible. If the difference between the white and the black cannot be altered, then the contrast can be increased by decreasing the average of the white and the black bar values, (see Eq. 6.5).
A source of error in measuring the contrast C is saturation of the white bars. Increasing the white bar image value above saturation by increase of camera gain, will keep the white value fixed while the black value increases resulting in a decrease of contrast. Another source of error is uneven illumination of the bar-pattern. Another source of error is random noise in the images, however this error is reduced by averaging 100 bar-target images. Defocusing by the camera optics and the digital sampling by the detector array can also contribute to contrast reduction. Scattering causes the reflected light from the white bar to leak into the black bar, reducing the contrast.
It is concluded that the contrast measurement is useful for characterization of the water as a medium of optical imaging, because the contrast is measured under the same conditions as the gated viewing two- and three-dimensional laser radar imaging. The water type, the laser radar system settings, and the range are the same, i. e. for each three-dimensional recording the contrast has also been recorded. It is concluded that scattering is the major source of contrast reduction and at longer distances both scattering and absorption reduce the contrast by attenuation. It is concluded that for a given range and bar-target period, the contrast depends on the water type. It was experimentally verified in Sec. 5.1 above, that fine three-dimensional images could be recorded even in low contrast conditions. Thus if the contrast is high enough then a two-dimensional underwater imaging mode for sea-mine identification is feasible. If the contrast is low a three-dimensional underwater imaging mode for sea-mine identification is feasible. Thus the Navy's sea-mine identification operator needs a switching capability between high contrast two-dimensional gated viewing laser radar live video imaging and low contrast gated viewing three-dimensional laser radar imaging.

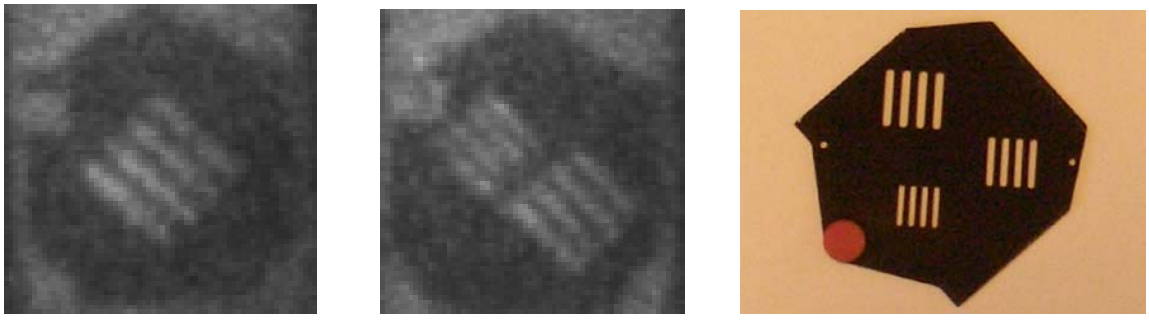

Fig. 6-5. Left, middle, and right: Bar-target number (3), (4, 5), and (6,7,8) respectively, (see Table 6-1). . Left and middle: The bar-targets are recorded through seawater at 5 m range with camera gate time 0.5 ns. Right: The bar-target is recorded in air with an amateur digital camera.

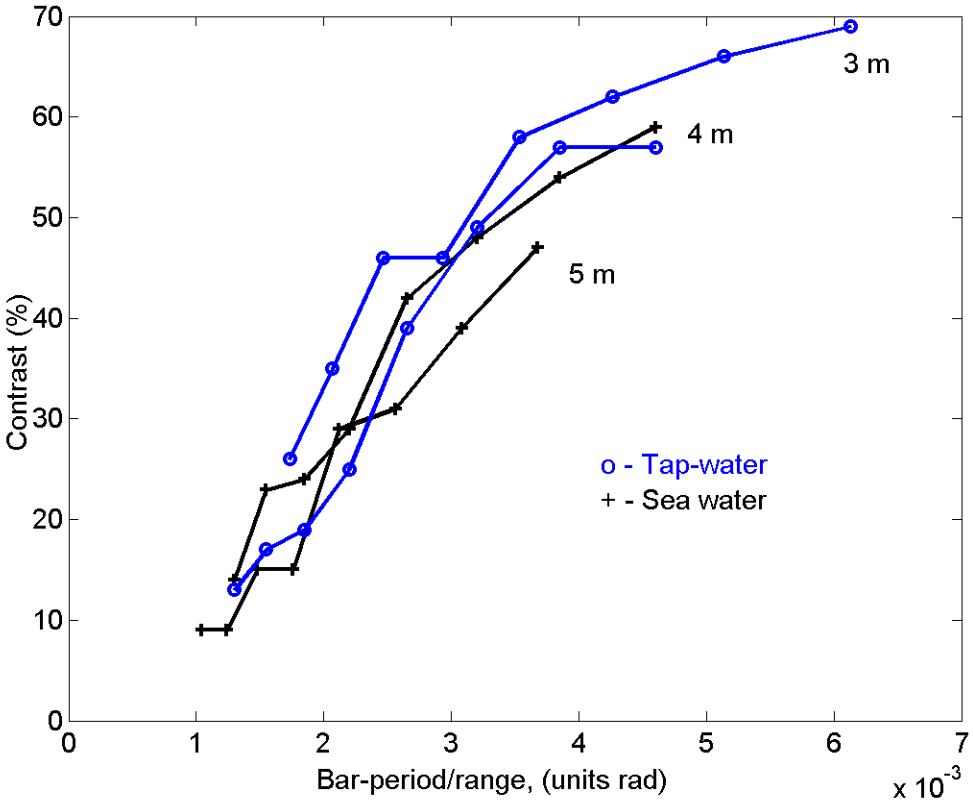

Fig. 6-6. Underwater bar-target contrast in tap water at 4 and 5 m range and in seawater at 3 and 4 m. The contrast is zero for zero bar-period.

Bar number	Bar period (black and white, mm)
1	18.4
2	15.4
3	12.8
4	10.6
5	8.8
6	7.4
7	6.2
8	5.2

Table 6-1. The periods of the bar targets. One period is equal to the width of a black and a white bar.

6.5 Trial of three-dimensional underwater imaging

In the previous sections information has been acquired about the water as a medium of optical imaging. That information helps to understand the results of the underwater laser radar experiment presented below. This section presents the gated viewing three-dimensional laser radar images recorded at the Danish Defence Research Establishment in Nov.-Dec. 2004. This section in combination with the preceding sections gives a reasonable good intuition about how well the gated viewing laser radar will perform, when applied in sea-mine identification applications.

Tap- and seawater is successively filled in a 10 m long and 0.4 m wide tube fitted with a glass window at one end, Fig. 6-7 and Fig. 6-8. Holes about 0.25 m wide are cut in the upper side of the tube at about 1 m intervals. Objects are placed in the tube through the holes. The laser and camera are put on an optical bar about 1.5 meters long. The focal length of the camera optics is 85 mm and the number of pixels is 582×752. The optical fiber is rolled up in front of the laser. The field of illumination of the laser pulses output from the fiber is controlled manually by change of the focal length of a small lens mounted on the optical bar. The salinity of the brackish sea water is about 15 ‰.
The target is the sandy miniature Manta sea-mine dummy displayed in Fig. 6-9. The sandy sea-mine is chosen to make an analog simulation of the condition where the sea-mine has laid some time on the bottom. The longer a sea-mine lies on the bottom the more likely is it that it will loose contrast, because it is covered by silt, sand, and marine life. A non-gated image of the sandy dummy through 5 m seawater is seen in Fig. 6-10. Repeated utilization of the dummy has several advantages. First, the dummy is small so the laser pulses can be concentrated in a narrow field of illumination. Second, the repeated utilization makes comparison of the three-dimensional imaging capabilities in air and in water easy. Third, the shape of the dummy is simple for simulation. Three-dimensional underwater images of the sandy dummy recorded at 4-5 m in seawater and 4 m in tap water are presented in Fig. 6-11 to Fig. 6-13. The camera gate time is 0.5 ns and the delay step is 0.1 ns. Through 5 m seawater the dummy height is reasonably well preserved, Fig. 6-11. It should be emphasized how much better the three-dimensional image in Fig. 6-11 is compared to the non-gated contrast image in Fig. 6-10. The non-gated image is deteriorated by the backscatter from the water column. The low contrast of the sandy dummy to the background makes it difficult to recognize even in a two-dimensional range gated image. It is a fine example of the strength of gated viewing three-dimensional laser radar imaging. Through 4 m seawater the dummy height is well preserved with high range accuracy, Fig. 6-12. The decrease in range accuracy from 4 to 5 m in seawater is caused by a decrease in signal to noise ratio. Through 4 m tap water the dummy height of 5 cm is well preserved, Fig. 6-13. The target deformation is small at 4 m in tap- and seawater and larger at 5 m in seawater. In general the target deformation is a rounding of the edges, which is more pronounced at 5 m than at 4 m. Reflections on the inside of the tube have been observed in the range gated images. The gated viewing three-dimensional laser radar images presented in Fig. 6-11 to Fig. 6-13 are the raw versions without any post-enhancement algorithms applied. The raw gated viewing three-dimensional images are displayed because they give an intuition of the raw laser radar performance. In general, the three-dimensional images can be improved in two ways by the application of digital signal processing. First, the images of the recorded image sequence can be enhanced by different noise reducing techniques, such as frequency filters and de-convolution filters, e. g. Wiener filter, [Gonzalez et al. 2004], which lead to a three-dimensional image with improved range accuracy. Second, the same noise-reducing techniques can be applied directly to the range image or the three-dimensional image. Computational it is faster to work with single three-dimensional image than with the whole image sequence of 50-100 images. In future image enhancement techniques will be applied to the three-dimensional images.

Fig. 6-7. Gated viewing three-dimensional underwater imaging. The optical fiber laser radar set-up and the entrance of the water tube. The yellow coil is the 30 m optical fiber. The gated viewing laser radar is placed in the basement at the Danish Defence Research Establishment.

Fig. 6-8. Gated viewing three-dimensional underwater imaging. Water tube, 10 m long and 0.4 m diameter.

Fig. 6-9. The sandy dummy recorded with an amateur digital camera. The Dummy is 5 cm high and 12.3 cm in bottom diameter.

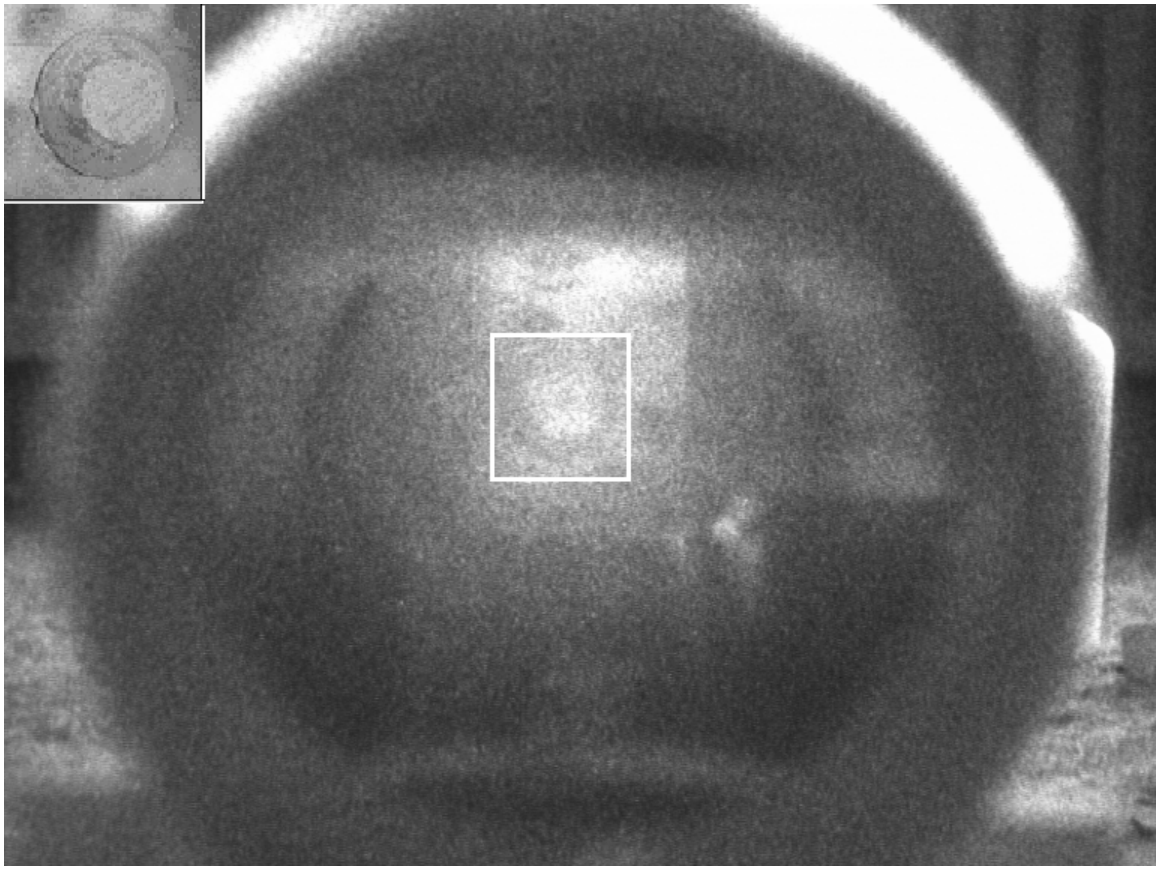

Fig. 6-10. Laser illuminated and non-gated image of the sandy dummy at 5 m range in seawater. The dummy is placed inside the tube, (Fig. 6-8). The sandy dummy in the white box is hardly seen because of the backscatter. Upper left corner: Handheld digital image of the sandy dummy.

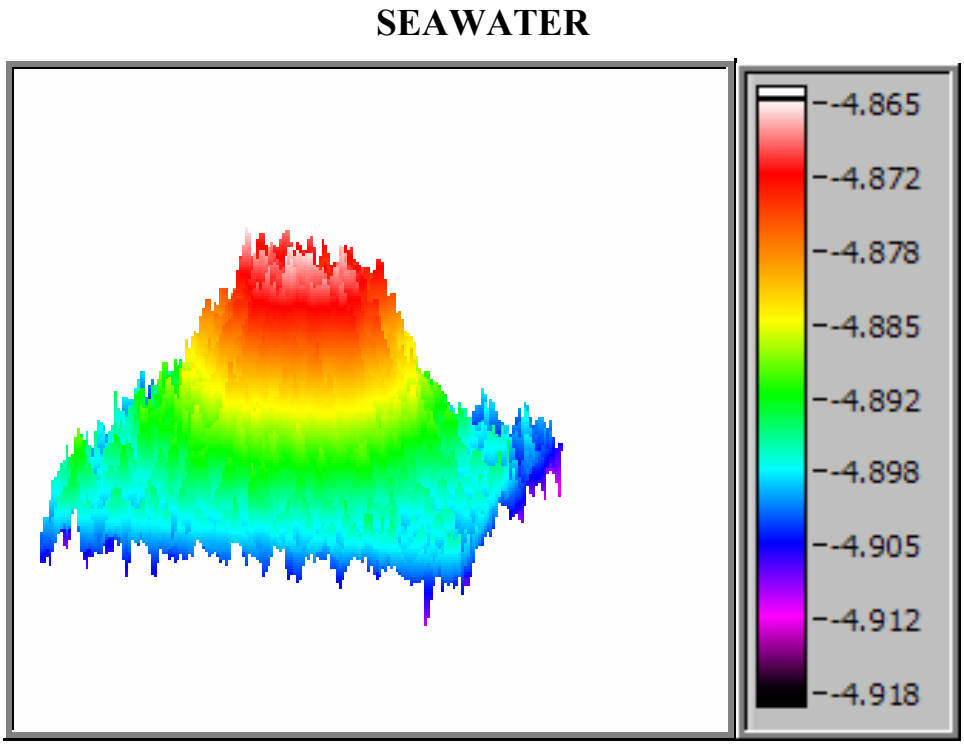

Fig. 6-11. Sandy dummy in seawater. The camera gate time is 0.5 ns and the delay step is 0.1 ns. The two range scales are in meters. (Note: The horizontal is not in scale).

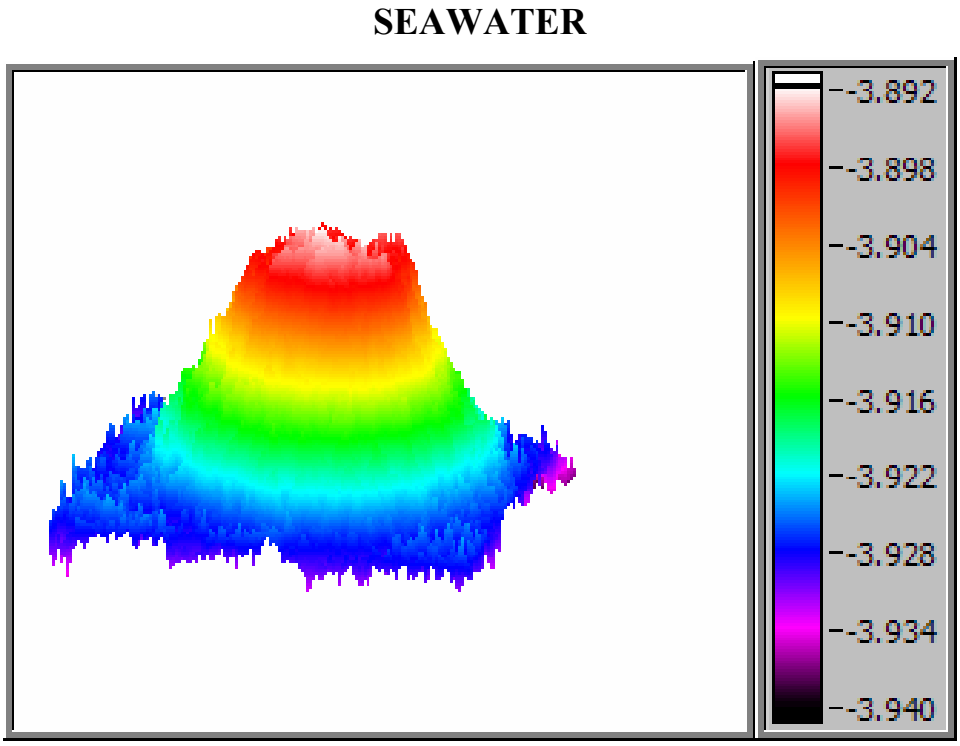

Fig. 6-12. Sandy dummy in seawater. The camera gate time is 0.5 ns and the delay step is 0.1 ns. The two range scales are in meters. (Note: The horizontal is not in scale).

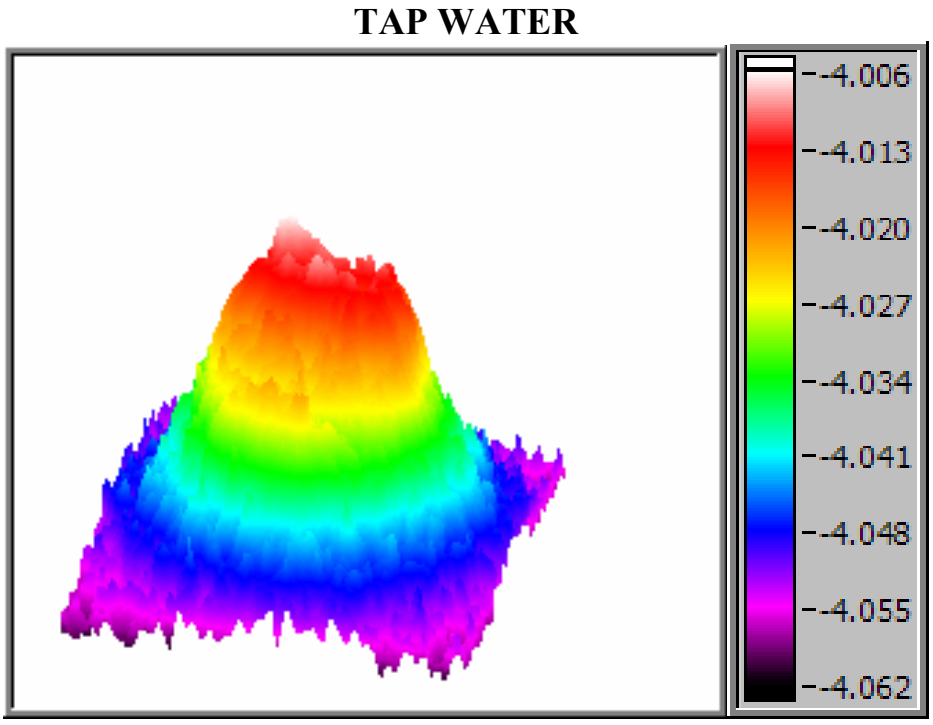

Fig. 6-13. Sandy dummy in tap water. The camera gate time is 0.5 ns and the delay step is 0.1 ns. The two range scales are in meters. (Note: The horizontal is not in scale).

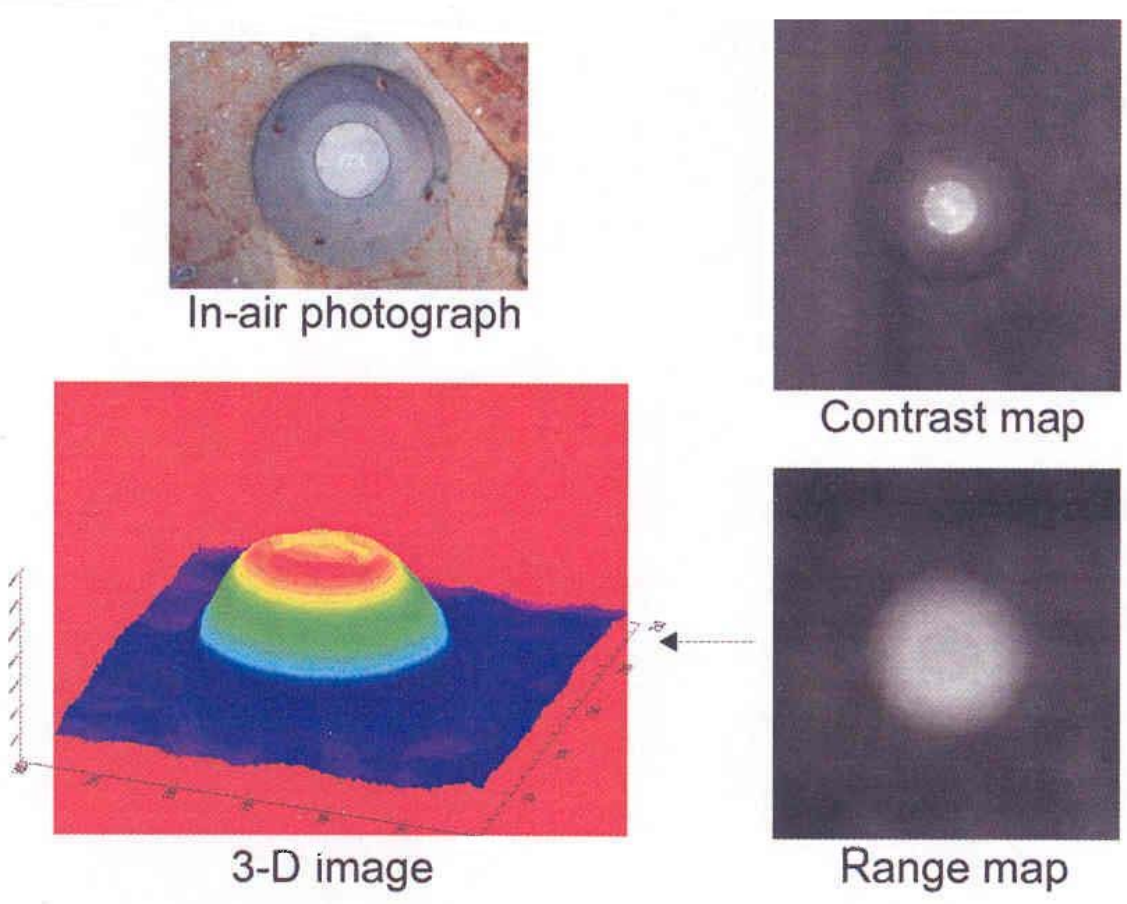

Fig. 6-14. Sea-mine images by the streak tube imaging lidar (STIL), [Nevis, 2003].

In 2002 a three-dimensional underwater images of a Manta sea-mine dummy ten times larger than the dummy presented here were reported, Fig. 6-14, [Nevis et al. 2003, 2002; Nevis, 2003]. In 1999 a much similar trial has been done with more or less the same outcome, [Gleckler, 1999]. The dummy was imaged at 7 m range underwater by the streak tube technique. The range accuracy was about 1 cm and the target was deformed by rounding of the edges. Though the result is fine the processing of the streak tube imaging lidar data take much longer (hours) than the processing time for the gated viewing three-dimensional laser radar images, which is less than a minute.

6.6 Summary and conclusion

For the first time gated viewing three-dimensional underwater imaging is presented, i.e. nobody has reported on the application of the laser radar configuration described in the preceding chapters to record three-dimensional underwater images. There are other laser radar systems, which have been used for submerged underwater two- and three-dimensional imaging, [Nevis et al. 2003, 2002; Nevis, 2003; Gleckler, 1999; Tetlow et al. 1999; Maddalena et al. 1998; McLean et al. 1998; Chantler et al. 1997; Bjarnar et al. 1991]. The best of the reported underwater three-dimensional images made by others are presented in this thesis, (Fig. 2-3, Fig. 2-5, and Fig. 6-14). It is concluded that the two-dimensional and three-dimensional performance of the presented gated viewing laser radar configuration is good enough to be tested further in an underwater remote operated

vehicle applied in a simulated sea-mine identification trial. The tests, experiments, and trials of the thesis have been throughout static, i.e. the laser radar and the targets do not move. It is an obvious step forward to test the laser radar performance from a moving or hovering platform, the platform being submerged, on land, or in the air.

The refraction of light in the air-water interface improves image resolution but plays an ignorable role for the three-dimensional underwater images presented. The tap- and seawater attenuation is exponential and together with the blurring by scattering, the decrease in signal to noise ratio expectedly deteriorates the three-dimensional images more at 5 m than at 4 m range. It is concluded that due to the exponential attenuation, the laser power should be increased eight times to increase the range performance by one attenuation length.

Image processing techniques can of course be exploited to enhance the recorded three-dimensional images, but due to time constraints the three-dimensional image enhancement has been omitted. The contrast is measured and reveals a decrease in contrast by an increase in range for both tap- and seawater. It has been proposed that gated viewing two- and three-dimensional imaging is feasible under high and low contrast conditions.

7 Scattering phase function model and underwater optical data set

This chapter is dedicated to the underwater environment, i.e. the laser radar is not discussed in this chapter. It has been discussed in the previous chapters that absorption and scattering are the physical properties of the water that limits the performance of underwater laser radar. Regarding the spectral absorption, the optical blue-green wavelength is optimal for underwater imaging dependent on the water type, (Fig. 6-4). Thus after choosing the optimal wavelength for transmission there is not much to do to overcome the exponential absorption other than applying a more powerful laser. The attenuation by scattering is also exponential but most of the scattered light is forward scattered in small angles. The small angle forward scattering causes a degradation of the recorded images. If a deeper knowledge about the scattering can be acquired it can be exploited for optimal image restoration of the degraded images.

In the spring of 2003 three months of research was carried out at the Defense Research & Development of Canada (DRDC), Quebec, Canada. The aim was to study a scattering phase function model proposed by the Canadians, and analyze an underwater optical characteristics data set with respect to the scattering phase function model, [Forand et al. 1999, Fournier et al. 1994].

An introduction is given in Sec. 7.1, the data set of the underwater optical characteristics (i.e. attenuation, scattering and absorption) is described in Sec. 7.2, the data analysis is described in Sec. 7.3-7.5, and summary and conclusion is given in Sec. 7.6.

The rigorous scattering phase function model is presented in App. C.

7.1 Introduction

Physical aspects of the scattering phase function are introduced in this section. What amount of light is scattered? The amount of light is scattered covering how long distance? In which directions are the light scattered?

The proposed scattering phase function (β) depends on scattering direction (θ,Φ), the relative refractive particle index (n_r), i.e. relative to pure water, and the size distribution of the particles $F(r_p)$, where r_p is the particle radius. It is commonly assumed that the phase function is rotationally symmetric with respect to the line of propagation, i.e. independent of Φ, Fig. 7-1.

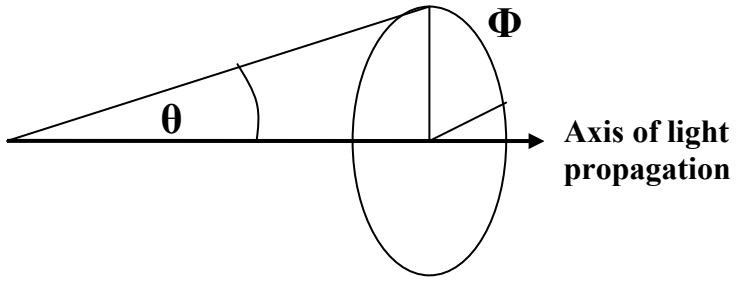

Fig. 7-1. Sketch of the scattering angles, where it is commonly assumed that the phase function is rotationally symmetric with respect to the line of propagation, i.e. independent of Φ.

The light scattered in a given direction is described by the scattering phase function β. Consider rotational symmetry around the axis of propagation of the photons, the scattering coefficient is given by integration of the scattering phase function

$$b = 2\pi \int_0^{\pi} \beta(\theta)\sin(\theta)d\theta\,, \tag{7.1}$$

where the factor of 2π comes from the implicit integration of the symmetric angle Φ.
Consider the exponential attenuation of light due to absorption and scattering

$$Q(r) = Q_0 \exp(-(a+b)r)\,, \tag{7.2}$$

where Q_0 is the amount of light at r = 0, a is the absorption coefficient, and b is the scattering coefficient.
Consider the total amount of light lost by absorption and scattering covering the distance from 0 to r

$$Q_{total}(r) = Q_0(1 - \exp(-(a+b)r)\,. \tag{7.3}$$

Consider the loss of light due to absorption Q_a and scattering Q_b, covering the distance from 0 to the characteristic scattering length r = 1/b

$$Q_a = Q_0 \frac{a}{a+b}\left(1 - \exp\left(-\frac{a+b}{b}\right)\right), \tag{7.4}$$

$$Q_b = Q_0 \frac{b}{a+b}\left(1 - \exp\left(-\frac{a+b}{b}\right)\right), \tag{7.5}$$

where it can be noted that the ratio $Q_a/Q_b = a/b$ of light lost to absorption and scattering is constant, i.e. independent on range r. Note also that of course $Q_{total}(r) = Q_a(r) + Q_b(r)$.
The expressions Eq. 7.1 and Eq. 7.5 tell that Q_b is the amount of light lost by scattering covering the distance from 0 to the characteristic scattering length r = 1/b, and that the light is scattered at the angles described by the scattering phase function β.
The scattering phase function model is based on an assumption about the particle size distribution. The assumption is that the particles are distributed according to an inverse power law. The distribution is called a Junge particle distribution.

$$F(r) = \frac{C}{r^{\mu}} \tag{7.6}$$

where C is a constant, r is particle radius and μ is the Junge coefficient.
The data analysis in Sec. 7.3-7.5 focuses on the determination of the Junge coefficient and determination of the relative refractive particle index (n_r).

A derivation of the point spread function from the scattering phase function has been reported, [Fournier et al. 1999]. The point spread function is a result of multiple scattering. The point spread function is a well known concept and widely used in image restoration filters, e.g. the general de-convolution filters or inverse filters, the Wiener filter, the parametric Wiener filter, or the Lucy-Ricardson filter, [Gonzalez et al. 2002, 1987; Matlab, 2002; Jain, 1989].
It is concluded that if the scattering phase function can be determined, then it can be exploited for image enhancement and improved sea-mine identification.

7.2 Data set

The underwater optical data set was collected in Halifax harbor, Nova Scotia, Canada, February, 2002, [Wiedemann et al. (unpub.2004)]. The data set consists of absorption- and attenuation coefficients measured at the wavelengths: 412, 440, 488, 510, 532, 555, 650, 676, and 715 nm. These coefficients were measured with an absorption and attenuation instrument called AC-9. The volume scattering function (VSF) was measured at three angles: 100^{o}, 125^{o}, and $150\ ^{o}$, with an instrument called ECO-VSF. The two instruments are lowered down slowly through the water column and the data are collected as profiles of the column. Each profile is composed of about 2000 samples for each nine wavelengths of the AC-9 and for each of the three angles of the ECO-VSF instrument. The maximum depth is about 10-12 meters. The scattering coefficient b is derived from the absorption and attenuation coefficients by the relation

$$b = \alpha - a, \tag{7.7}$$

where a is the absorption coefficient and α is the attenuation coefficient.
An example of a depth profile of the seawater scattering coefficient is shown in Fig. 7-2. The scattering coefficients are derived for the water column from 0.5 m to 9 m. The magnitude of the scattering coefficient decreases about (0.9-0.6)/0.9 = 33 % from the top to the bottom. In oceanography it is often assumed that the ocean consists of horizontal layers. Variations in the horizontal direction are more pronounced in the vicinity of river outflows or up- or down-welling areas. It has been observed that the data set contains variations in the optical properties over time at a fixed location. It can be seen from Fig. 7-2, that for image enhancement purposes, it is insufficient to measure the optical properties at the surface if sea-mines are to be found on the bottom. Thus the optical properties have to be measured at the same time, depth and horizontal position as the sea-mine identification occurs, which puts restraints on the image enhancement processing utilizing the measured optical properties. A practical example was given in the introduction (Chap. 1 above), it is crucial that the thrusters of the remote operated vehicle do not stir up the fine particles deposited on the bottom, because of immediate disturbance of the underwater visibility, i.e. immediate change of the (local) optical properties.

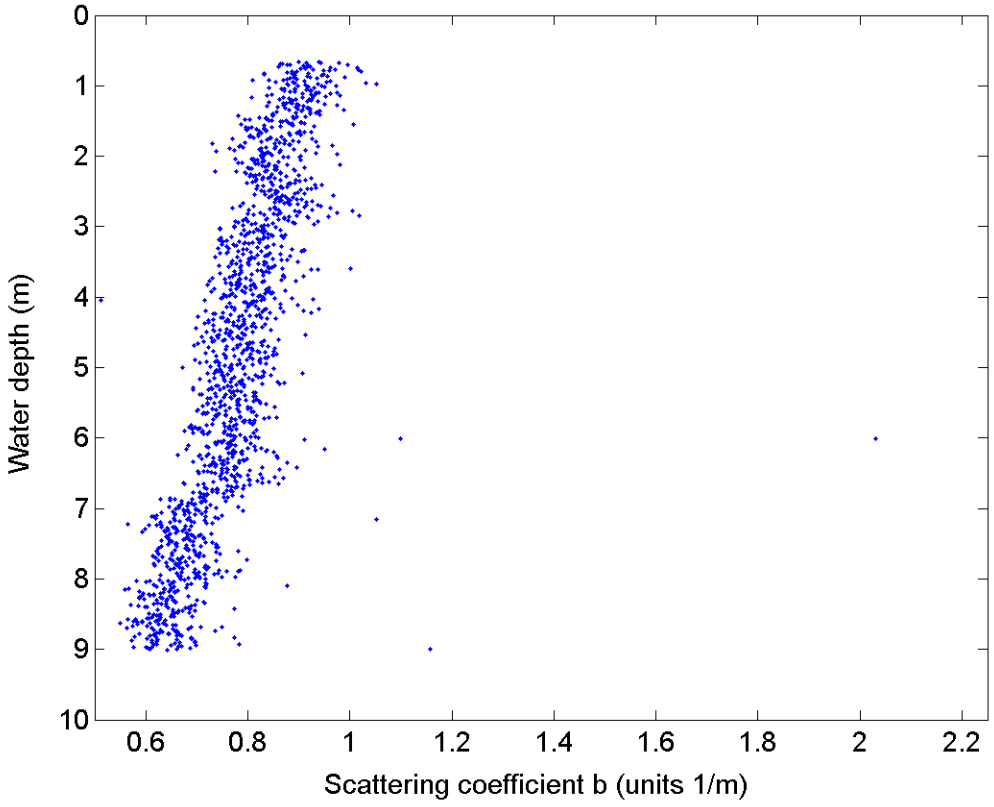

Fig. 7-2. The scattering coefficients b at the wavelength of 532 nm.

7.3 First approach to determine the Junge coefficient

The Junge coefficient (μ) of the particle size distribution of the particles suspended in the water needs to be determined for a determination of the scattering phase function, which can lead to a point spread function, that can be exploited for image enhancement and improved sea-mine identification.

Using the expression Eq. C5, (App. C), and dividing by b_{ref} on both sides and taking the logarithm, the Junge coefficient can be isolated

$$\mu = \frac{\log\left(b/b_{ref}\right)}{\log\left(\lambda_{ref}/\lambda\right)} + 3, \tag{7.8}$$

where b is the scattering coefficient and b_{ref} is the scattering coefficient at the reference wavelength λ_{ref}.

It is assumed that the change in the relative particle refractive index n_r by change of the wavelength is small enough that it can be considered constant within the wavelength interval 412-715 nm. The expression Eq. 7.5 is applied for the derivation of the Junge coefficient. An error bar plot of the Junge coefficient versus wavelength is shown in Fig.

7-3. The Junge coefficient describes the particle size distribution and does not depend on wavelength.
The 715 nm channel is missing due to an instrument malfunction. The blue, green, and red error bars are plots of μ with λ_{ref} = 412, 532, and 676 nm, respectively. The width of the error bars are the standard deviation down through the water column. The error bars close to the reference wavelength λ_{ref} are large, because of division in Eq. 7.5 by the log(x), where x = λ_{ref} /λ is close to 1. Note that the blue is missing at 412 nm, the green is missing at 532 nm, and the red is missing at 676 nm.
In general it has been observed that the scattering phase function, (App. C, Eq. C1), is invalid for certain values of the relative refractive index (n_r), the scattering angle (θ) and the Junge coefficient (μ), i.e. the predicted scattering phase function value is negative.
A different approach to determine the Junge coefficient is taken below to see whether the results are consistent.

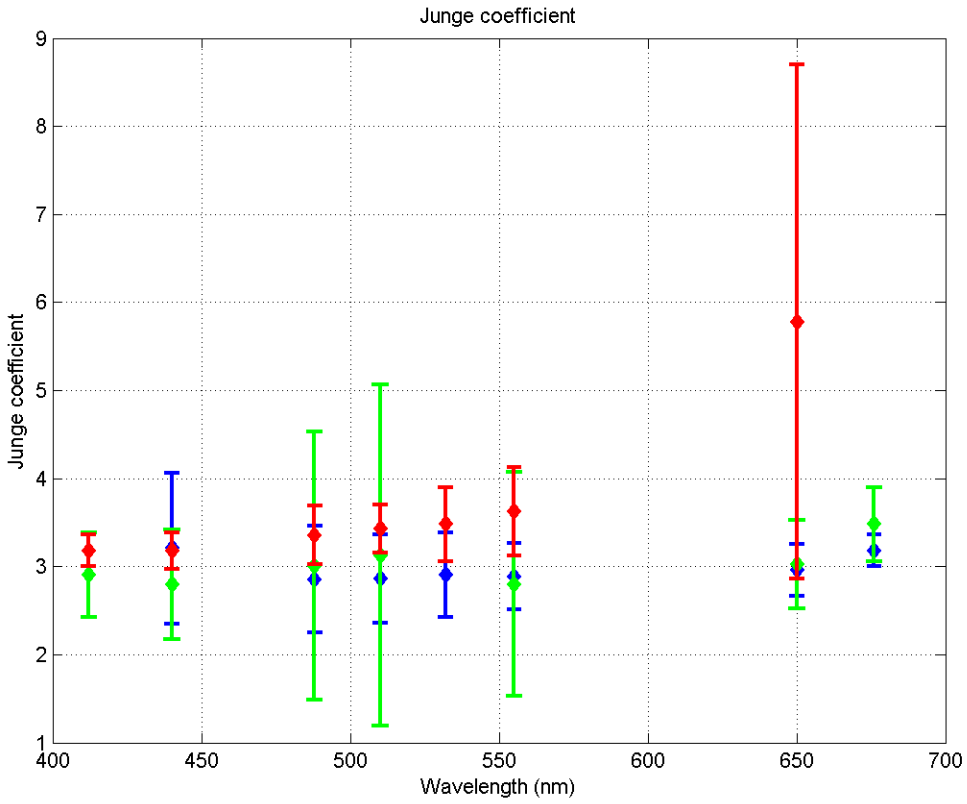

Fig. 7-3. The Junge coefficient versus wavelength.

7.4 Second approach to determine the Junge coefficient

In this section the determination of the Junge coefficient is based on all the wavelength channels of the AC-9 instrument, except for the malfunctioning 715 nm absorption channel, which is dead zero. The determination of the Junge coefficient is restricted to the values from three to five.

The Junge coefficient μ is determined by the linearity of the logarithmic scattering coefficient to the logarithmic wavelength. Take the logarithm on both sides of expression Eq. C4, (App. C),

$$\log(b) = k_2 + k_1 \log(\lambda), \tag{7.9}$$

where b is the scattering coefficient, k_1 and k_2 are the variables to be fitted, and λ is the wavelength.
The linear relation in Eq. 7.9 is fitted by a least squares method. The fitting includes an outlier filter of the scattering profiles of the water column, i.e. the scattering coefficients deviating more than the mean value plus/minus two times the standard deviation of the nearest 50 data points are replaced by the mean value of the 50 points.
The Junge coefficient is related to the slope k_1

$$\mu = 3 - k_1, \tag{7.10}$$

where the determined Junge coefficients are plotted in Fig. 7-4. The determination of the Junge coefficient is restricted to values above three, because it has been observed that in many cases the scattering phase function is negative for values of the Junge coefficient below three.

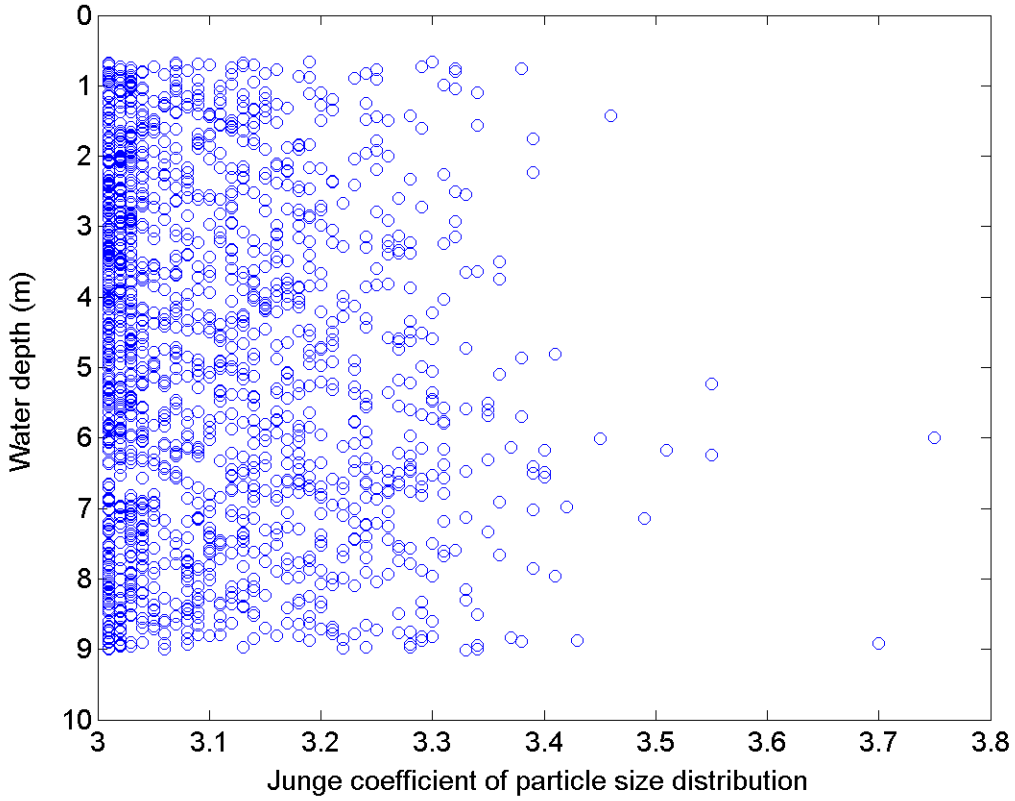

Fig. 7-4. The Junge coefficient of the particle size distribution. The Junge coefficient is determined for all wavelengths. The water depth is 0.5-9.0 m. (Note, the scale of the water depth is reversed).

7.5 Fitting the relative refractive index of the particles

The Junge coefficients derived by the second approach in the previous section are used together with the volume scattering phase function data, measured by the instrument ECO-VSF, to fit the relative refractive particle index (n_r), where n_r is taken relative to the refractive index of pure water.

In the following analysis is it assumed that the relation between the model scattering phase function (β), the measured volume scattering function (VSF_{meas}), and the measured scattering coefficient (b_{meas}) can be written

$$VSF_{meas} = \beta \times b_{meas} . \tag{7.11}$$

The relative refractive particle index (n_r) fit is done by a least squares method

$$\begin{aligned} s = & \left(\beta\left(100^o, n_r\right) - \frac{VSF_{meas}\left(100^o\right)}{b_{meas}} \right)^2 + \\ & \left(\beta\left(125^o, n_r\right) - \frac{VSF_{meas}\left(125^o\right)}{b_{meas}} \right)^2 + \\ & \left(\beta\left(150^o, n_r\right) - \frac{VSF_{meas}\left(150^o\right)}{b_{meas}} \right)^2 \end{aligned} \tag{7.12}$$

where s is the sum to be minimized with respect to the relative refractive particle index n_r, β is the model scattering phase function, and b_{meas} is derived from the measured absorption and attenuation coefficients at 532 nm. The volume scattering function instrument (ECO-VSF) measures the scattering at 530 nm. The two nanometers difference is ignored.

The relative refractive particle index is plotted in Fig. 7-5. As can be seen in the figure the relative refractive particle index is not well determined. A closer look at the scattering phase function model reveals that the model predicts zero scattering when the Junge coefficient is equal to three. With a Junge coefficient slightly larger than three the model predicts a non-zero, positive scattering, but the model phase function is only weakly dependent on the particle index, (App. C, Fig. C2). A small error in the determination of the Junge coefficient leads to a large error in the determination of the relative refractive particle index. Unfortunately, this is the case for all the scattering angles $0^o \leq \theta \leq 180^o$, when the Junge coefficient is close to three.

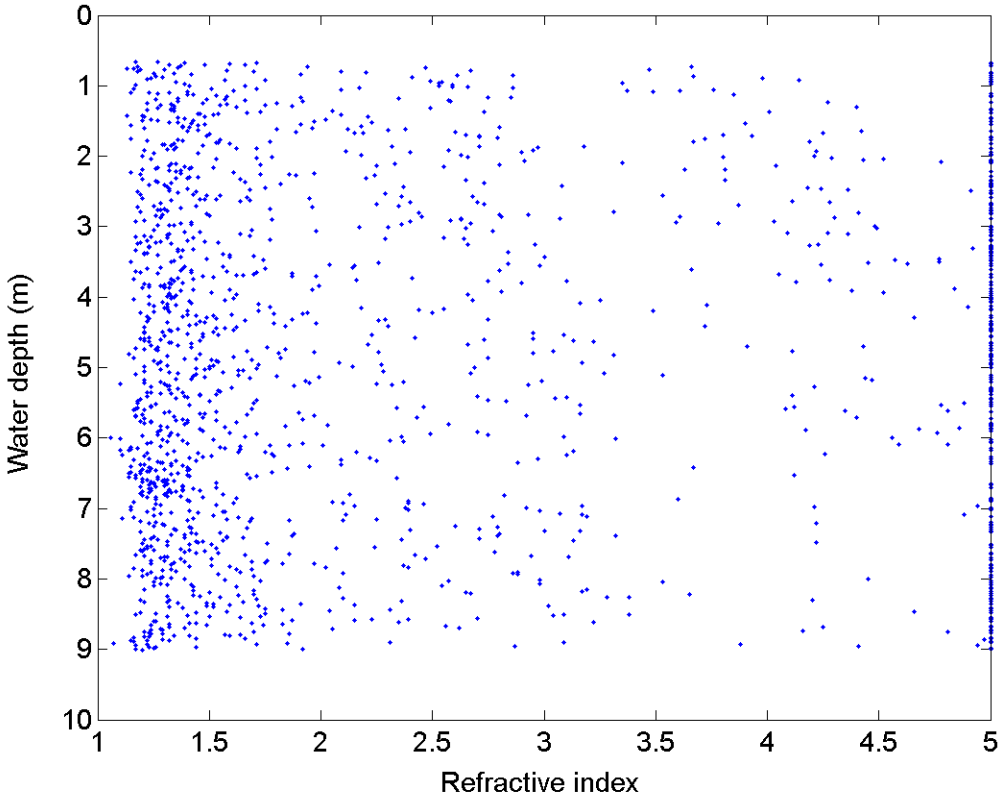

Fig. 7-5. The relative refractive particle index (n_r). The refractive particle index is taken relative to the refractive index of pure water.

7.6 Summary and conclusion

The scattering phase function has been introduced and the scattering phase function model proposed by the Canadians has been discussed. A data set of underwater optical properties has been analyzed concerning the proposed scattering phase function model and more specific the Junge coefficient of the particle size distribution and the relative refractive particle index. The value of the Junge coefficient was found to be close to three, which makes it difficult to determine the relative refractive particle index. The resulting relative refractive particle index shows a large variability, which makes it unfit for practical use. In conclusion it is estimated that the resulting relative refractive particle index can not be used in practice to determine the scattering phase function and therefore the goal of outlook of the scattering phase function analysis can not be reached. The outlook of the scattering phase function analysis was to simulate a point spread function of water by a Monte-Carlo algorithm from the knowledge of the scattering phase function acquired from the data set of underwater optical properties acquired at Halifax in Nova Scotia. The point spread function could then have been applied in an image enhancement filter, the Wiener filter, for the ultimate goal of improved sea-mine identification. It is concluded that no further effort has been done to determine the scattering phase function regarding the work of this thesis.

Questions that have risen from the work with the scattering phase function model. For example, what is the size and variability in space and time of the water volume for which

the Junge particle size distribution is valid? What is it, in the derivation of the scattering phase function model, which causes the scattering phase function model to predict negative scatter in some cases?

8 Signal processing – simulation and experiment

In Chap. 7 the overall goal of improved sea-mine identification by image enhancement based on measurement of the inherent optical properties of the seawater and determination of the water point spread function by a model scattering phase function, was somehow wrecked, because it was estimated that the result of the data analysis, i.e. the relative refractive particle index, could not be used in practice. In this section a different approach is taken with regard to the determination of the point spread function and the aim of improving the sea-mine identification by image enhancement. The approach in this section is to determine the line spread function which is closely related to the point spread function. An empirical de-convolution filter method is first applied to simulated data and afterwards applied to recorded slit images.

An optical image transmitted through a scattering medium convolves with the medium point spread function (psf). In general the point spread function is the transmitted image of a point. The overall point spread function is dependent on the camera optics, the range from the object to the detector, and the optical scattering characteristics of the transmitting medium. The image blurring caused by the medium point spread function is a result of multiple scattering of the light by particles and molecules. The large span of optical characteristics for different media determines the varied performance of the laser radar system. For example, in clear water the performance may be much better than in murky water. The image blurring caused by the point spread function decreases the image contrast.

The mathematical operations of the Fourier transform and convolution stated in the following has been done by the build-in functions of Matlab, [Matlab, 2002], (alternatively: [Gonzales et al. 2002]).

Consider a noiseless input image h(x,y). The transmitted image

$$g(x,y) = psf(x,y) * h(x,y), \tag{8.1}$$

where x and y denote the image pixels, * denotes convolution in x and y, and psf(x,y) is the point spread function.

By taking the Fourier transform F on both sides, the convolution operation becomes an operation of multiplication in the complex spatial frequency domain

$$G(u,v) = otf(u,v) \times H(u,v), \tag{8.2}$$

where u and v denotes frequency (units: 1/pixel), G(u,v) = F(g(x,y)), otf(u,v) = F(psf(x,y)) is the optical transfer function, and H(u,v) = F(h(x,y)).

The inverse filter de-convolution is done in frequency domain by division

$$H(u,v) = \frac{G(u,v)}{otf(u,v)}, \qquad (otf(u,v) \neq 0), \tag{8.3}$$

and with the inverse Fourier transform F^{-1}

$$h(x,y) = F^{-1}\left(\frac{G(u,v)}{otf(u,v)}\right), \tag{8.4}$$

where the original image h(x,y) is restored.
If both the images h(x,y) and g(x,y) are known, the point spread function can be determined

$$psf(x,y) = F^{-1}\left(\frac{G(u,v)}{H(u,v)}\right). \tag{8.5}$$

Note that G(u,v) and H(u,v) can be the Fourier transform of any images on the restraints that H(u,v) is not zero and the expression Eq. 8.1 is fulfilled.
Consider the line spread function

$$lsf(x) = \int psf(x,y)dy, \tag{8.6}$$

where x and y denote the image pixels.
Consider the one-dimensional optical transfer function otf(u) to be the Fourier transformation F of the line spread function, i.e. otf(u) = F(lsf(x)).
A cross sectional profile h(x) of a Gaussian laser beam is simulated. The line spread function lsf(x) is assumed Gaussian.
The output

$$g(x) = lsf(x) * (h(x) + n_h(x)) + n_g(x), \tag{8.7}$$

where * denotes convolution in x, $n_h(x)$ and $n_g(x)$ are simulated Gaussian distributed input- and output noise respectively, (Fig. 8-1, top, red points). The standard deviations of the input and output noise are 10 units 8-bit.

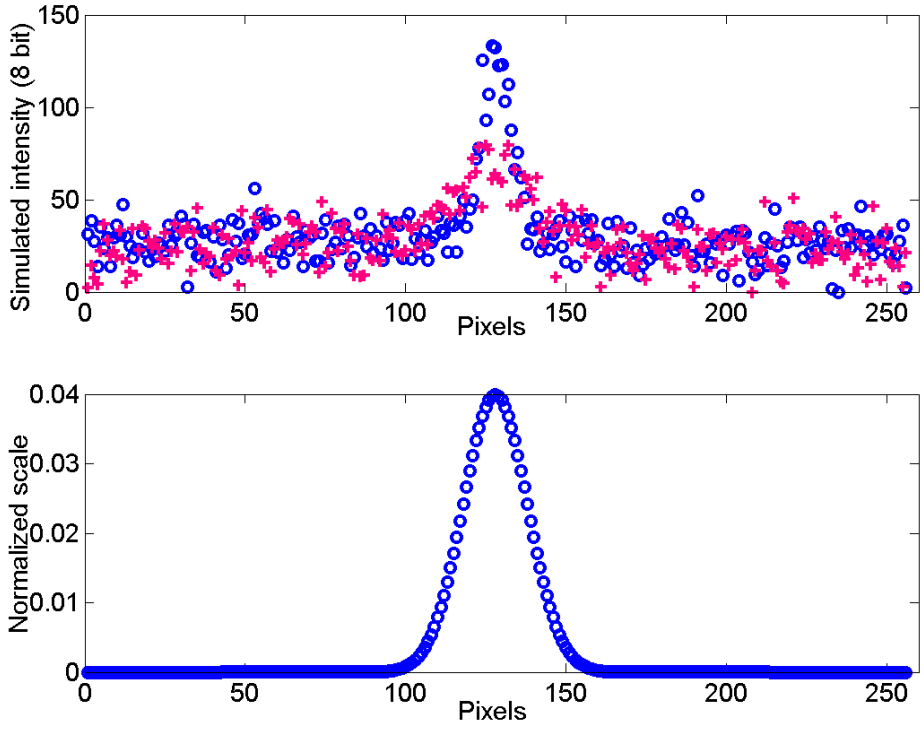

Fig. 8-1. Top: The simulated input signal with noise, i.e. h(x) + n_h(x), (blue). The simulated output with noise, i.e. Eq. 8.7, (red). The simulated output is the discrete convolution of the input and the line spread function. Bottom: The line spread function (lsf(x)) is normalized, i.e. the line spread function integrates to unity.

The simulated data displayed in Fig. 8-1 (top diagram), is used as the onset for restoration of the original line spread function. The restoration consists of two steps: an inverse de-convolution followed by a low-pass filter.
The first step

$$otf(u) \approx \frac{F\big(g(x)\big)}{F\big(h(x)+n_h(x)\big)}, \tag{8.8}$$

where the approximation (≈) is introduced, because the nominator is F(g(x)) and not F(g(x) - n_g(x)), which would have been correct according to the expression Eq. 8.7.
The next step is a low-pass filtering

$$lsf(x) = F^{-1}\big(lp(u)\times otf(u)\big), \tag{8.9}$$

where lp(u) is the rectangular low-pass filter defined by

$$lp(u) = 1 \quad for \quad |u| < u_{\max}\ . \tag{8.10}$$

where the frequency $u_{max} \approx 1/(2\sigma_{lsf})$, and σ_{lsf} is the standard deviation of the line spread function.
The lsf(x) is the function to determine, so σ_{lsf} is generally not known and u_{max} is therefore determined by manual inspection of the power spectrum

$$P(u) = \left|F\left(lsf\left(x\right)\right)\right|^2 . \tag{8.11}$$

The power spectrum is the same as the square of the modulus of the optical transfer function. The modulus of the optical transfer function is the modulation transfer function mtf(u), [Ducharme, 2004]. The modulation transfer function is shown in Fig. 8-2. The blue circles are the unfiltered modulation transfer function, while the red crosses are the low-pass filtered modulation transfer function.
In Fig. 8-3, the restored line spread function, (i.e. restored by the expression Eq. 8.9), is shown together with the original simulated line spread function, (Fig. 8-1, bottom). The oscillation around zero is caused by the low-frequency noise and related to the low-pass filter cut-off frequency. The amplitude of the oscillation is about 10 % of the maximum value of the line spread function.
Because of time constraints it is beyond the scope of the thesis to find and apply a method to get rid of the oscillations, but that could be an obvious follow-up.

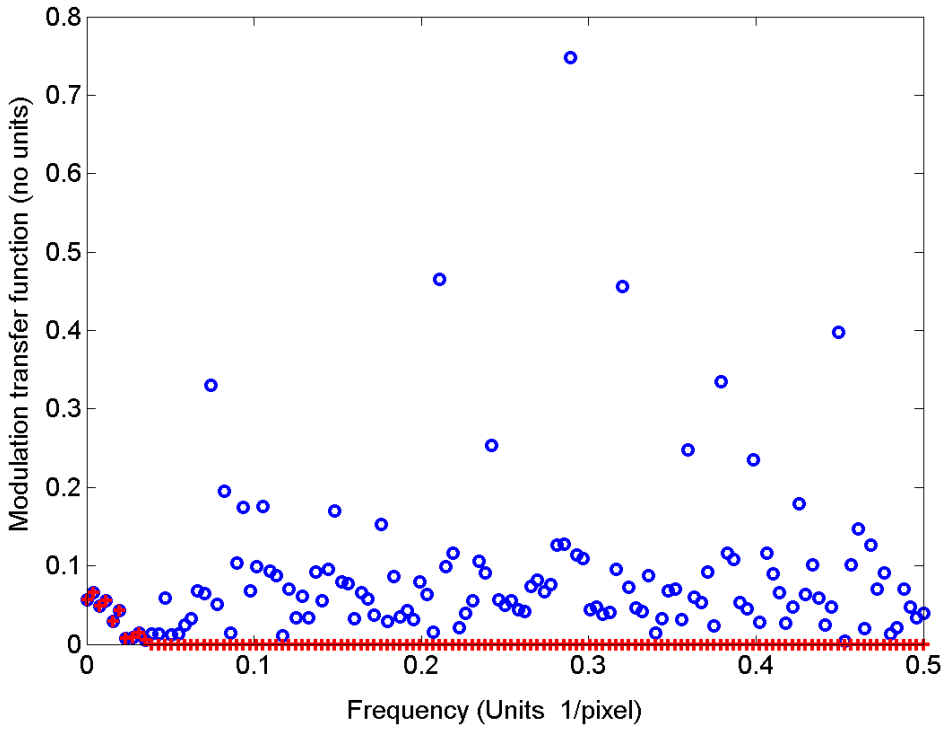

Fig. 8-2. Low-pass filtered and non-filtered discrete modulation transfer functions (red crosses and blue circles, respectively). The modulation transfer function is the modulus of the optical transfer function. Note, the maximum frequency is the Nyquist frequency 1/(2×1 pixels), where the sampling interval is one pixel.

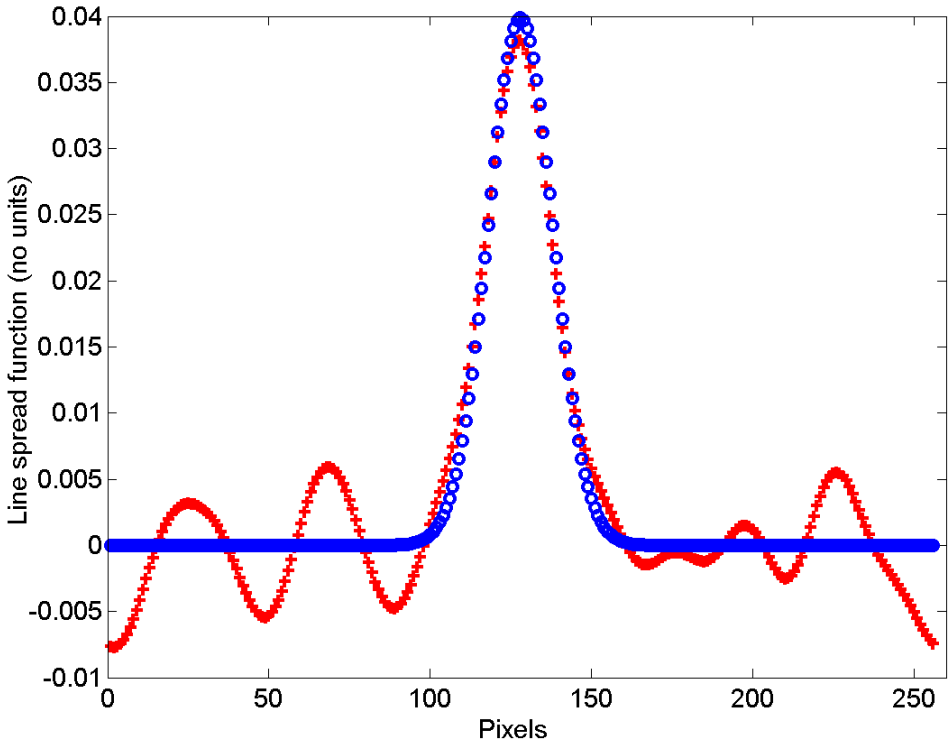

Fig. 8-3. Line spread functions. (Red: Line spread function from the expression Eq. 8.9. Blue: Pre-defined line spread function same as Fig. 8-1, bottom).

8.1 Experiment – water line spread function by de-convolution

The aim of this section is to find the water line spread function lsf(x) by the method of de-convolution described in the previous section. The input is a digital image of an optical slit, 1 mm wide and 5 mm high. The image is recorded in air. The distance from the slit to the front optics of the "Coherent" CCD camera is 215 cm, Fig. 8-4. The output image of the slit is recorded through 200 cm of water. The input and output windows of the water tube are thin optical glass windows. The experimental set-up is imaged in Fig. 8-5.

To get a better signal to noise ratio (SNR) in the output image the light source intensity is adjusted to near maximum of the eight bit scale, i.e. 255. Lateral resolution at 2 m range is about 1/20 mm/pixel with 480×640 pixels and 500 mm camera optics, i.e. the slit profile is about 20 pixels wide in the air corresponding to 1.3×20 = 26 pixels in water, because of refraction in the air-water interface (see Sec. 6.1 above).

The tube diameter is 10 cm. Donut shaped pieces of light absorbing material is fitted into the tube to avoid reflections from the inside of the tube. The input and the output slit images recorded through air and water respectively are shown in Fig. 8-6. These images are the set-out for the one dimensional de-convolution analysis. Several slit profiles are averaged to improve the signal to noise ratio. The averaged slit profiles are normalized such that the discrete profile values sum up to one. The air- and water slit profiles are

shown in Fig. 8-7, (blue and black curves, top display). The de-convolved water line spread function is shown in Fig. 8-7, (bottom display). The oscillation around zero is unphysical, because the negative values correspond to negative scattering.
To make a validation of the de-convolved water line spread function, it is convolved with the input slit profile (blue curve in Fig. 8-7, top display). The test-result is shown as the red curve in Fig. 8-7, (top display). Compare with the black output curve (Fig. 8-7, top display).

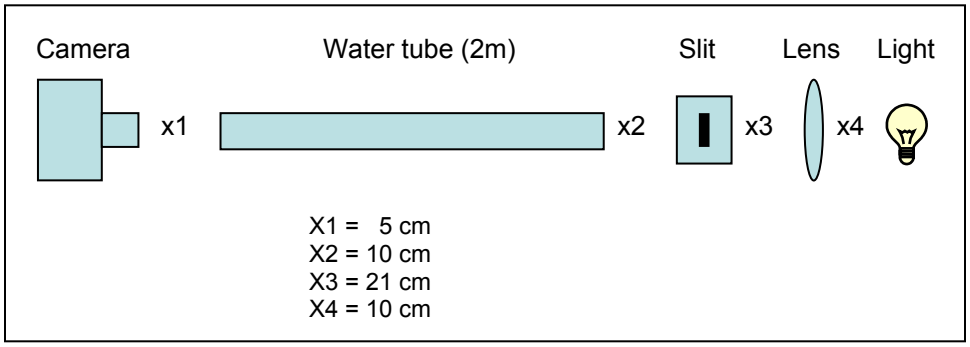

Fig. 8-4. Sketch of experimental set-up; Components and ranges for measuring water line spread function. The components are out of scale.

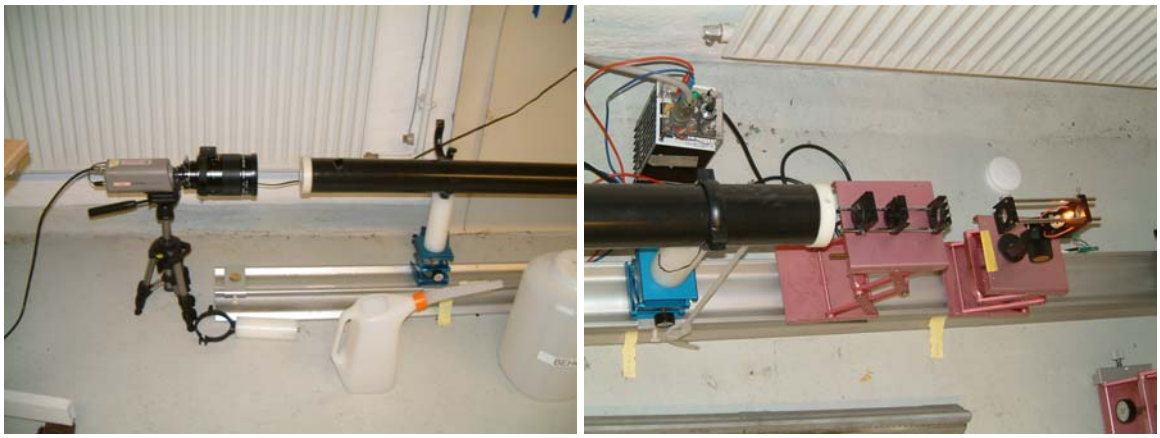

Fig. 8-5. Experimental set-up for measurement of water line spread function. Left: CCD camera with optics and the exit of the water tube. Right: Light source, lens, slit and entrance of the tube.

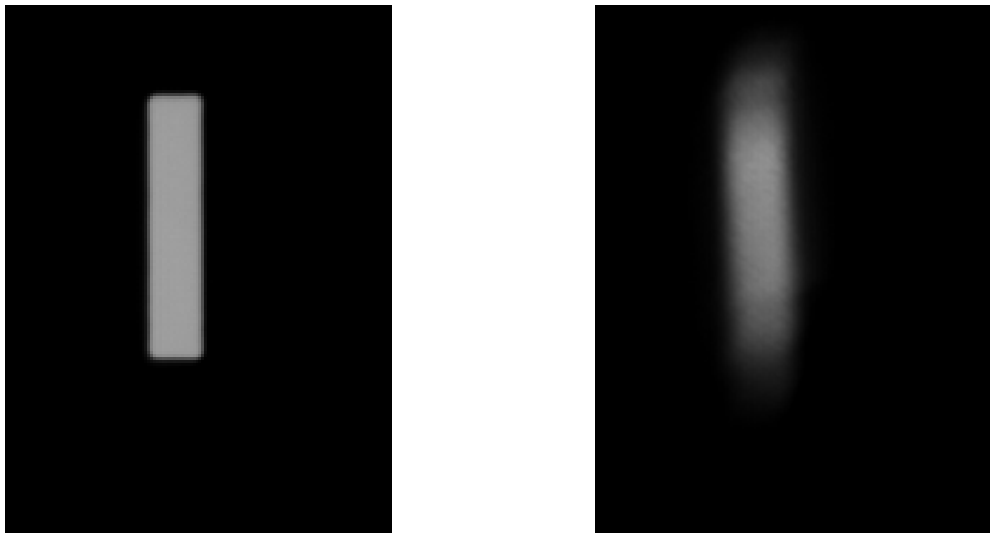

Fig. 8-6. Left and right: Slit images recorded through air and water respectively.

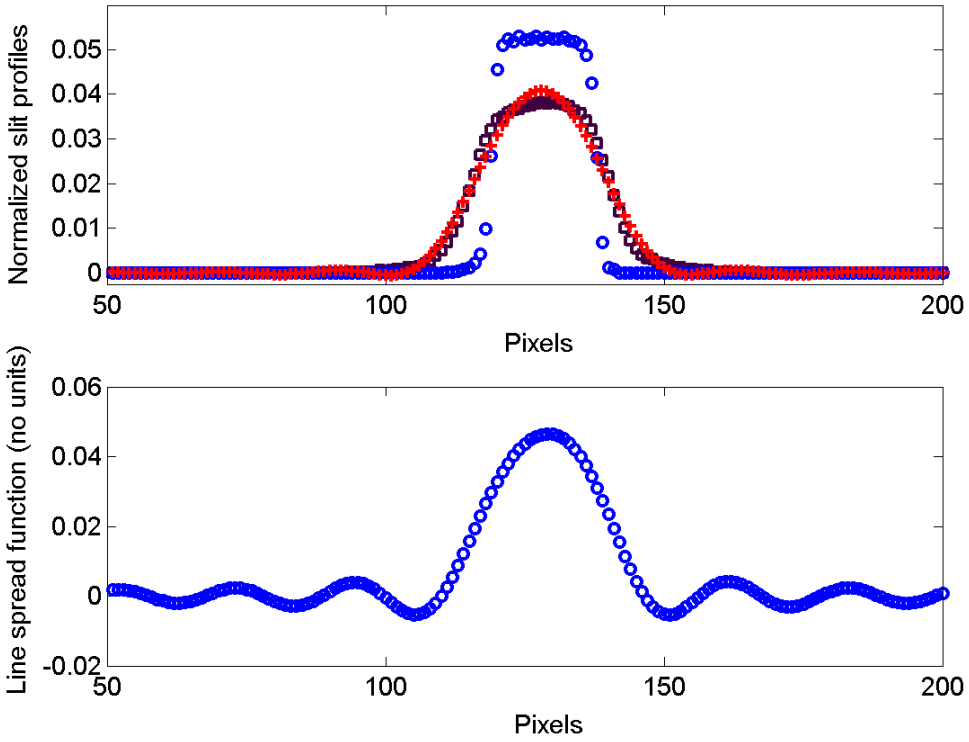

Fig. 8-7. Top: Air- and water slit profiles normalized (blue and black), together with the result of convoluting the water line spread function and input profile (red). Bottom: The normalized water line spread function derived from the images in Fig. 8-6.

Because of refraction in the air-water and water-air interfaces of the tube the slit profile is broadened when imaged through the water (Sec. 6.1 above). Therefore the determined line spread function is a composition of the broadening by refraction and the scattering by the water. One source of uncertainty is the focusing of the camera optics. The Spread

function due to de-focusing has been described [Ducharme, 2004]. It should be noted that the line spread function (or the point spread function) in principle can be found from images other than slit images as long as the basic expression Eq. 8.1 is valid for the applied images.

The two-dimensional point spread function has been determined by the two-dimensional equivalent to the line spread function determination method described in previous section. In general the two-dimensional determination of the point spread function does not reveal anything methodically new and is therefore omitted. Analogue to the oscillations around zero for the line spread function determination described above there are oscillations around zero has been observed. If the oscillations of the point spread function could be eliminated, then the point spread function could be applied for image enhancement leading to improved sea-mine identification.

The Wiener filter has been studied as a candidate for image enhancement with the knowledge of the point spread function. The Wiener filtered image is optimal in the sense of minimization of the variance between the filtered image and the true un-blurred image. The Wiener filter requires that the point spread function is known and it also needs some noise information as input. The Wiener filter can be replaced by the parametric Wiener filter, [Gonzalez et al. 2002, 1987; Jain, 1989]. In practice the image restoration is done by changing the noise parameter until the filtered image is optimal by visual inspection. It is concluded that the Wiener filter is not as good in practice as in principle. There are other image restoration filters that require the point spread function known, for example the Lucy-Richardson filter, [Matlab, 2002]. It is concluded that more time needs to be dedicated to find the optimal filter for image enhancement with knowledge of the point spread function.

Initial inspiration to Chap. 8 was found in the literature, [Zhishen et al. 2001]. During the work of Chap. 8 it is observed that image restoration by an estimated spread function is not strongly dependent on the exact knowledge of the blurring spread function. Thus reasonably good restoration can be made with a spread function that looks like the blurring spread function. More work is necessary to quantify what is meant by “looks like”, which is an obvious follow-up for future work.

Underwater images are degraded by scattering. An instrument for determination of the line spread function or the point spread function could be useful for restoration of the underwater images. If the point spread function could be measured directly and applied in an image enhancement filter to improve the recorded two- and three-dimensional images, it could improve the sea-mine identification. One challenge in image restoration by the measured point spread function is that the water spread function varies dependent on water type, time, and location. Natural waters are typically layered horizontally but can vary considerable with depth. The point spread function needs to be measured at the same time and place as the gated viewing laser radar imaging.

8.2 Summary and conclusion

A method of image enhancement for improved sea-mine detection has been proposed. The method was first evaluated by digital simulation and thereafter applied to a pair of recorded images. The method determines the water line spread function by a combination of de-convolution and low-pass frequency filtering of two slit images recorded in the air and water. The method shows promising results, but it is concluded that more time is

needed to improve the method and reduce the ringing or oscillation of the determined line spread function, before it can be applied in practice.

9 Gated viewing laser radar simulation

This chapter is a short introduction to a digital simulation tool of the gated viewing three-dimensional laser radar developed as part of the thesis. The aim is to get a deeper understanding of the variables of the gated viewing laser radar system and the environment that influences the performance. In general the knowledge gained by the development of the digital simulation can be used in the planning of future experiments and to understand the result of the present experiments. The chapter is strongly supported by the paper: "Simulation of gated viewing mono-static three-dimensional laser radar", [Busck, sub.2004]. The simulation considerations of the gated viewing three-dimensional laser radar are discussed. The digital image simulations have been compared with experimental three-dimensional underwater images and three-dimensional telescopic images, [Busck, sub.2004]. The simulated laser pulses and camera gate are considered rectangular in time, which give a piece-wise linear range gate of the reflected radiant pulse energy. The range gate is combined with a Gaussian laser beam, a medium point spread function, and a laser radar equation that governs the medium attenuation, surface scattering, and camera characteristics, to give the detected image signal. By changing the variables of absorption, scattering, refractive index, and the point spread function the digital simulation can be exploited for atmospheric as well as underwater applications. The presented computer model simulates the laser radar system and the surrounding environment and outputs a sequence of range gated digital images. The simulated output image sequence can be viewed directly or processed into a three-dimensional image by loading the image sequence into the laser radar image sequence analysis program, (Sec. 4.4 above). The interface of the gated viewing three-dimensional laser radar simulation is shown in Fig. 9-1. The interface is programmed in Labview, [Labview, 2003], while the computations are done in Matlab, [Matlab, 2002]. The interface is grouped into four basic modules: the laser, the camera, the medium, and the target.

An obvious follow-up in future is the incorporation and calibration of the logarithmic camera gain function described in App. A. The simulation can also be improved by incorporation of atmospheric turbulence and a point spread function, which is based on optical properties.

In future the three-dimensional target shape transfer function may be considered and explored by simulation and experiments. The relation between the overall point spread function and the three-dimensional target shape transfer function may be explored.

It is concluded that the digital gated viewing three-dimensional laser radar simulation has been a helpful tool to explore the variables of laser radar system and the environment. The development of the simulation tool and the knowledge acquired can be a help designing the optimal gated viewing three-dimensional laser radar for underwater sea-mine identification and other applications.

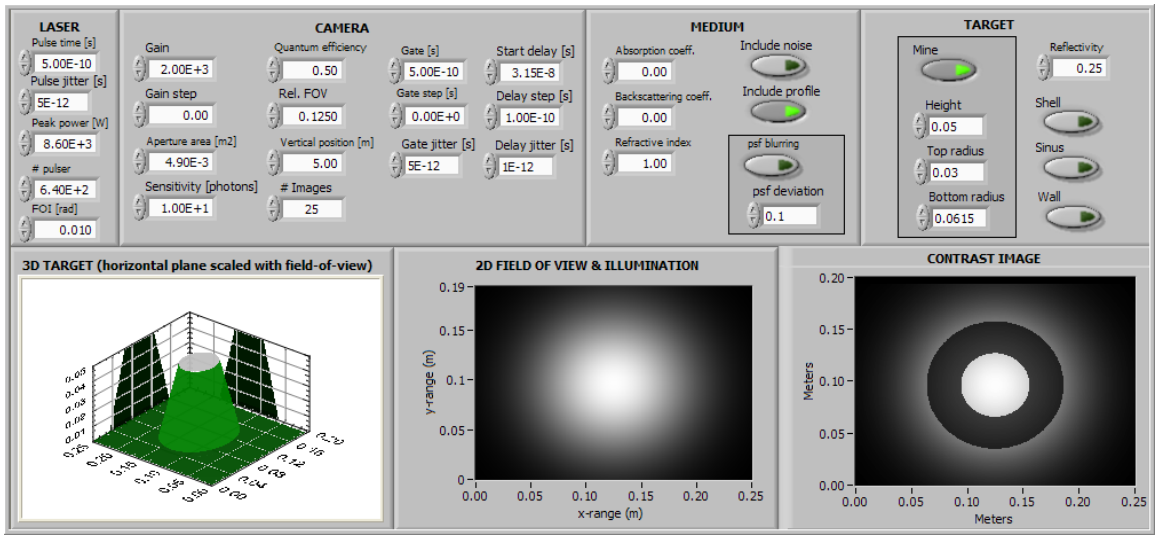

Fig. 9-1. Gated viewing laser radar simulation interface. The upper half of the interface is composed of four blocks concerned with (left to right) the laser, the camera, the medium, and the target. The lower part of the interface consists of three displays, from left to right, the simulated three-dimensional target, display of the simulated field of view and field of illumination, and the simulated contrast image of the target. The interface is made with Labview and the computations of the simulation is done in Matlab, [Labview, 2003; Matlab, 2002].

10 Summary and conclusion

A gated viewing high accuracy mono-static three-dimensional imaging laser radar system has been developed for the purpose of improving the underwater optical sea-mine identification handled by the Navy. Since the gated viewing laser radar system has been successfully proved to reduce underwater backscatter and provide high accuracy two- and three-dimensional images, it is concluded that the first part of the scope of the thesis: "*To develop an underwater laser radar, that applies the method of gated viewing for improved optical identification of sea-mines and objects on the sea bottom,*" has been carried out with success.

The laser radar system is based on a fast gating intensified CCD camera and an optical green pulsed laser. The innovation is a combination of the short laser pulses, the high laser pulse repetition rate providing a good signal to noise ratio, the fast gating camera, the fine control of the narrow range gate, the single mode optical fiber, and the algorithm for three-dimensional image formation. This innovative combination enables the gated viewing laser radar system to provide high-accuracy three-dimensional images. The novel algorithm developed for three-dimensional image formation, based on weighted average, has proved to be fast and simple, which is an obvious advantage. The disadvantage of the algorithm is that it is dependent on a correct image background subtraction. It is concluded that the second part of the scope of the thesis: "*To develop an algorithm that can be applied by the gated viewing laser radar for three-dimensional imaging, and to test and evaluate the algorithm acquiring knowledge of its advantages and disadvantages,*" has been accomplished with success.

Among the experiments and applications presented the innovation explicit related to sea-mine identification is the underwater three-dimensional images recorded with the gated viewing laser radar. For the first time gated viewing three-dimensional underwater images are presented, i.e. to the best of my knowledge nobody have reported on underwater three-dimensional images recorded by the laser radar configuration described and applied in the thesis. The gated viewing laser radar experiments and results presented in the thesis are static, i. e. neither the laser radar platform nor the target is moving. Thus if the same results are to be obtained by application of the gated viewing laser radar in an underwater remote operated vehicle, the remote operated vehicle is restrained to lay still for a few seconds while recording the three-dimensional image. This can be a disadvantage depending on the maneuverability of the remote operated vehicle and dependent on the underwater current and turbulence. It is beyond the scope of the thesis to answer how the gated viewing laser radar performs under dynamic recording, i.e. how the laser radar performs if either or both the laser radar and the target are moving during the three-dimensional image recording. In the present state the gated viewing laser radar allows for dynamic two-dimensional imaging in real-time and static three-dimensional imaging. It is an advantage that the gated viewing laser radar can be running in real-time gated viewing video mode and then record three-dimensional images in an interruption of only a few seconds. It is concluded that the third part of the thesis: "*To carry out stationary experiments with the laser radar under various conditions, starting in the laboratory and then in the open at successively longer ranges, to gain knowledge of the gated viewing three-dimensional imaging capabilities",* and the fourth part of the thesis:

"*To carry out experiments with objects submerged in water to gain knowledge of the gated viewing three-dimensional laser imaging performance in water,*" have been carried out with success.

Two new lines of approach have been taken to reach the goal of improved optical sea-mine identification by image enhancement based on knowledge and measurement of the optical properties of water. The first line of approach is founded in a scattering phase function model, which is utilized to analyze an underwater optical data set acquired by the Canadians at Halifax, Nova Scotia. The scattering phase function has been proposed by the Defense Research & Development Canada. The scattering phase function fitted to the data set could lead to a point spread function by Monte-Carlo simulation. The point spread function could then be applied in a digital image enhancement filter, thereby improving the underwater sea-mine identification. It is concluded that it has not been possible to fulfill the goal of improved sea-mine identification by image enhancement by this line of approach, because the variability of the determined variables has been estimated to be too large to be useful in practice, i.e. it has not been possible to determine the scattering phase function based on the underwater optical data set. The other line of approach to improved sea-mine identification by image enhancement is somehow more direct than the first line of approach, because the line spread function and the point spread function are determined directly from recorded images by digital processing. The approach has shown promising results, but it is concluded that more time need to be dedicated to improve the applied method before the determined line spread function can be applied in practice. In general it is concluded that fifth part of the scope of the thesis: "*To study the water as an optical medium, by a model scattering phase function and an underwater optical data set, for the purpose of image enhancement and improved laser radar performance,"* is partly fulfilled with success; i.e. valuable knowledge has been gained about the optical properties of water, and "partly", because more work has to be done before the proposed image enhancement algorithm can be proved successful in practice.

A digital gated viewing three-dimensional laser radar simulation tool has been developed, which has contributed to deepen the general understanding of imaging laser radars and the technique of gated viewing in particular, for example the location and depth of the gated range. The digital simulation tool applies to gated viewing three-dimensional laser radar imaging in the atmosphere and underwater. It is concluded that the sixth part of the scope of the thesis: "*To develop a digital simulation of the underwater gated viewing laser radar, to get a deeper understanding of the variables of the gated viewing laser radar system and the environment that influences the performance,*" has been successfully accomplished.

In future the gated viewing three-dimensional laser radar can be applied in an underwater remote operated vehicle and be an integrated part of the Navy's detection, classification and identification of underwater sea-mines and unexploded ordnance. On land the gated viewing high accuracy three-dimensional laser radar can become part of three-dimensional face recognition in airports for example.

Outlook

A NATO trial will be conducted in May-June, 2005, with focus on how turbulence affects active laser radar imaging, modeling issues, and underwater laser radar

applications. The gated viewing three-dimensional laser radar prototype will be one of the laser radars to be tested both underwater and under turbulent atmospheric conditions.
In future, further experiments will be done at the Danish Defence Research Establishment to explore the gated viewing three-dimensional laser radar potential for long range person identification.
The proposed prototype of the gated viewing three-dimensional laser radar can be improved in several ways:

- A more powerful laser will increase the imaging capabilities at longer ranges underwater and in the atmosphere.
- Shorter laser pulses and a faster camera will improve the range accuracy.
- A higher laser pulse repetition rate will decrease the recording time to a fraction of a second and make the gated viewing three-dimensional laser radar more suitable for imaging under dynamic conditions, i.e. where either or both the target and the laser radar is moving. Though, a higher repetition rate decreases the maximum non-ambiguity range of the laser radar.
- The internal camera electronics can be upgraded to give a shorter and more stable internal camera delay, which will improve the range precision.

To my knowledge no-one has reported on optical imaging through an underwater turbulent spring-layer created in the interface of two different water masses, e.g. water masses of different salinity and temperature. Turbulent spring-layers are often seen in the Danish belts, sounds, and straits all year around, because of the mixing of the brackish Baltic seawater and the more saline water from the North Sea. It is an obvious topic of research with relation to optical underwater sea-mine identification. Hopefully I may get the opportunity to present experimental documentation of the severity of the underwater spring-layer turbulence in underwater optical imaging. It could be of interest for researchers who work with underwater imaging and imaging through the air-water interface.

Appendix A - Camera gain

The aim of this appendix is to determine the functionality between the camera gain voltage and the camera gain, which is interesting to know in a laser radar simulation context.

An experiment was set up to investigate the gain function of the intensified CCD camera. A continuous-wave (cw) laser beam is attenuated and pointed directly into the camera optics. The laser is 5 mW at 543 nm and attenuated by 1000 to 5 μW to prevent damage to the camera. It is assumed that doubling the camera gate time doubles the image signal, i.e. the laser power is assumed stable and the 8-bit image value is linear in gate time. The linearity is without offset if the image background is subtracted, i.e. zero gate time gives an image value of zero.

The data of the experiment is summarized in Table A1. The camera gain voltage is increased in steps of 100 V except the last step of 50 V. The camera gate time is adjusted to avoid image saturation and to give a good signal to noise ratio. The third column is total laser spot signal. The image background is subtracted before calculating the total laser spot signal. The background values are determined by the average of 10×10 pixels in the upper right corner of the laser spot images. An optical filter is applied to suppress the ambient light.

Gain voltage (V)	Gate time (μs)	Image signal (8 bit)	Image background (8 bit)
200	1.00E+04	2800	22.8
300	400	2578	22.2
400	10	1510	21.7
500	2.5	2879	22.1
600	0.3	2361	21.8
700	0.07	2581	22.1
800	0.01	2173	21.8
900	2.50E-03	1477	22
950	1.50E-03	2113	22

Table A1. Data of the camera gain response characterization.

A first look at the data in Table A1 reveals that the camera gate time decreases by approximately a factor of 100 μs for each 300 V increase of gain voltage in the interval from 400-900 V. From 200 V to 500 V and from 300 V to 600 V the decrease in gate time is more like a factor of 1000.

When the background is subtracted, the ratio of camera gate time T_g to the laser spot image signal S is constant if the gain voltage is constant. Consider the camera gate time T_g versus image signal S as the function of gain voltage g

$$\frac{T_g}{S} = Ag^B, \qquad \text{(A1)}$$

where A and B are constants.

Taking the natural logarithm (ln) on both sides

$$\ln\left(\frac{T_g}{S}\right) = \ln(A) + B\ln(g). \qquad \text{(A2)}$$

The expression Eq. A2 is in the linear form y = ψ + ξ×x, where ψ = ln(A) and ξ = B are constants, ready for a linear regression analysis, (e.g. [Taylor, 1997]). Figure A1 shows the result of the linear regression. The constant B = –10 with an uncertainty of 2 %. The B is a camera characteristic constant that does not depend on external factors. The constant A depends on external factors, for example the transmission coefficient of the camera optics. It is concluded that the relation between the constant A and the external factors needs to be determined before the camera gain functionality can be incorporated into the digital gated viewing three-dimensional laser radar simulation tool.

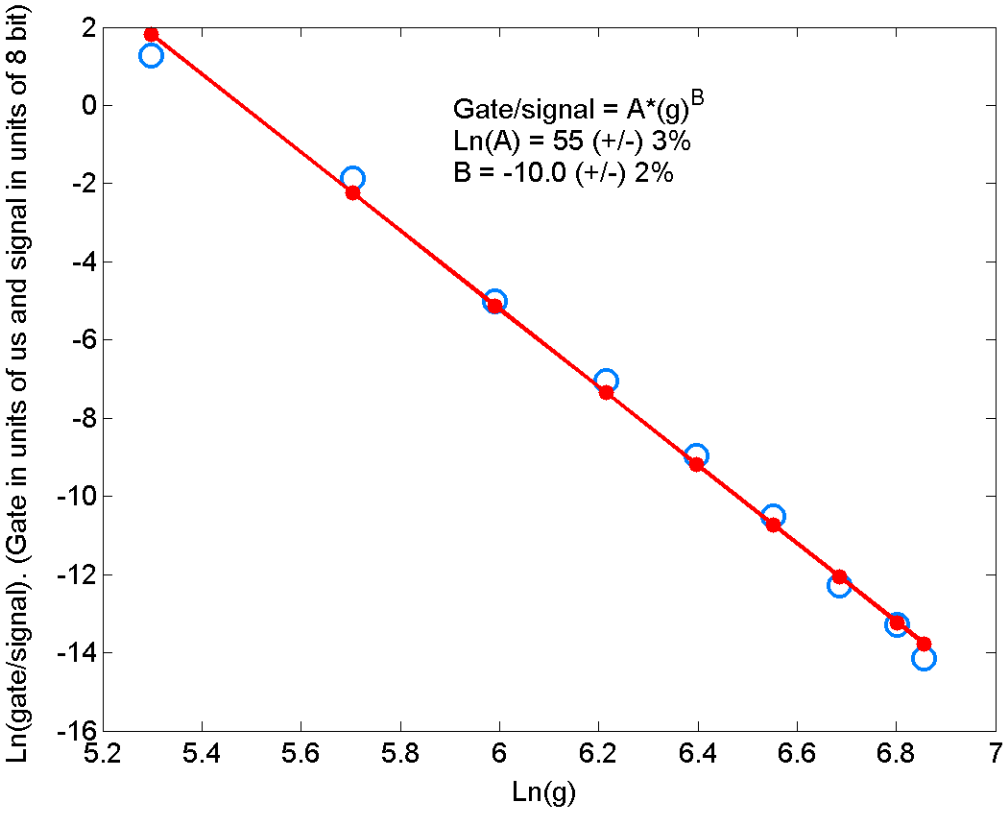

Fig. A1. Logarithmic camera gain response versus logarithmic gain voltage. The blue circles are the data points and the red line and dots are fitted by linear regression.

Appendix B - Noise background

If the image background is not properly eliminated the background can affect the range accuracy, the range precision and cause deformation of the three-dimensional image.
A background determination experiment has been done. 25 background images were recorded with the protection cap in front of the camera. No external light is input on the detector.
Figure B1 shows 450×650 pixels of one of the background images. The black/white scale is 8 bit pixel value. There are four features in the background noise image that can be seen explicitly. One is the four thin lines indicated by the letter A in the figure. Second is the horizontal "wave" indicated by the letter B. Third is the vertical "foot-ball field" pattern about 20 pixels wide all over the image. Fourth is an overall random noise with an offset of about 20 and a deviation about 1 unit 8 bit pixel value. The features A and B change from image to image. Figure B2 shows a computer rotated version of the image in Fig. B1, the four thin lines are easily seen.
Figure B3 shows the average of 25 background noise images. The single image features A and B are gone, the foot-ball field pattern is persistent, and the overall random noise mean offset is unchanged at about 20, while the deviation is reduced to about 0.25 unit 8 bit pixel value.

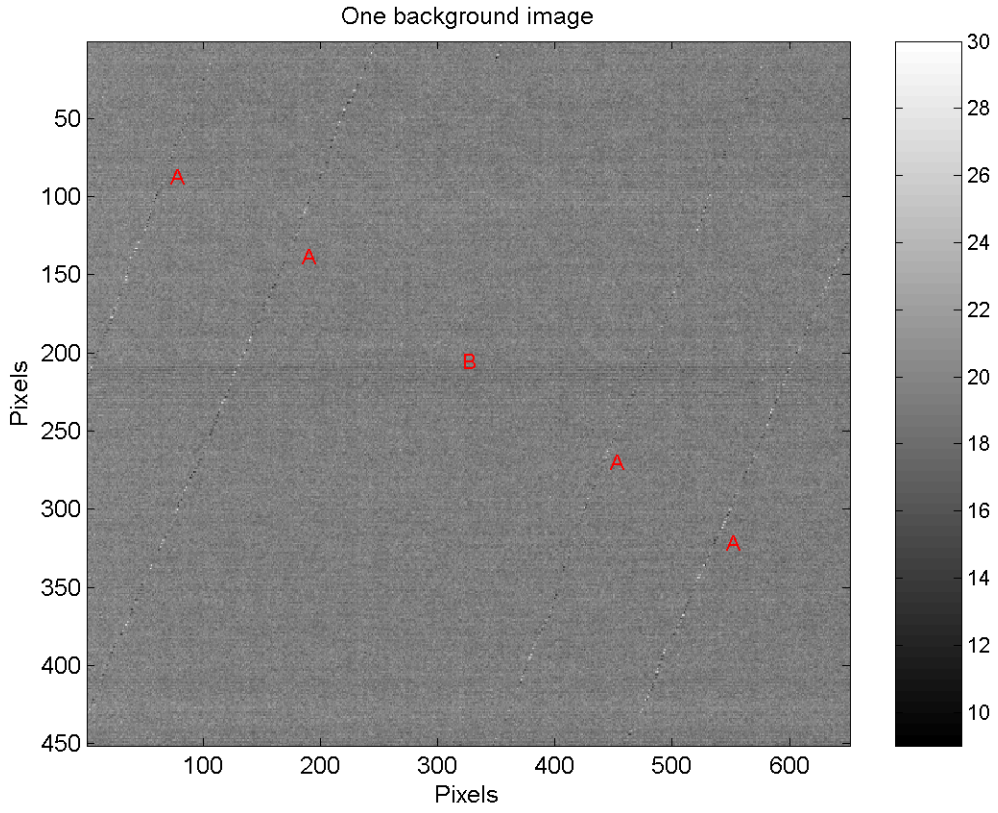

Fig. B1. Noise background image with black/white scale of 8 bit pixel values. Four lines are indicated by the letter A. A horizontal "wave" feature is indicated by the letter B. A weak vertical "foot-ball field" pattern can be recognized (see Fig. B3).

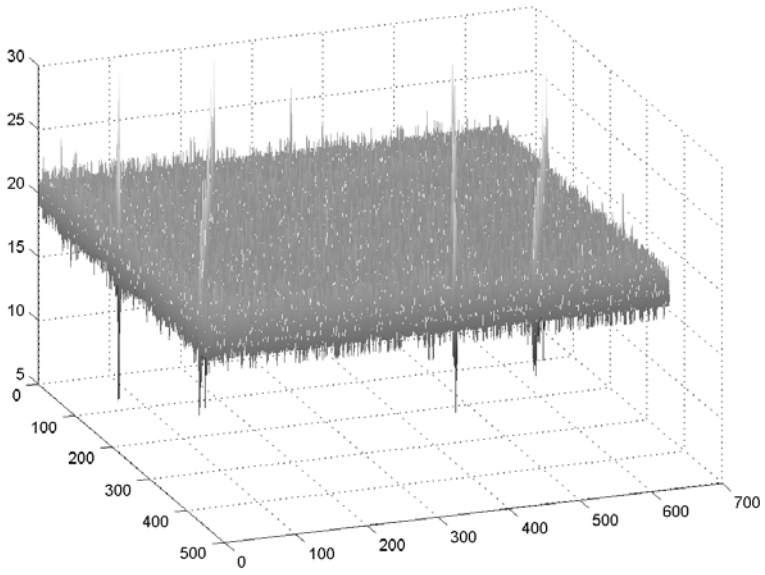

Fig. B2. Computer rotated noise background image of Fig. B1. The units of the x and y axes are pixels. The units of the z axis are 8 bit pixel intensity.

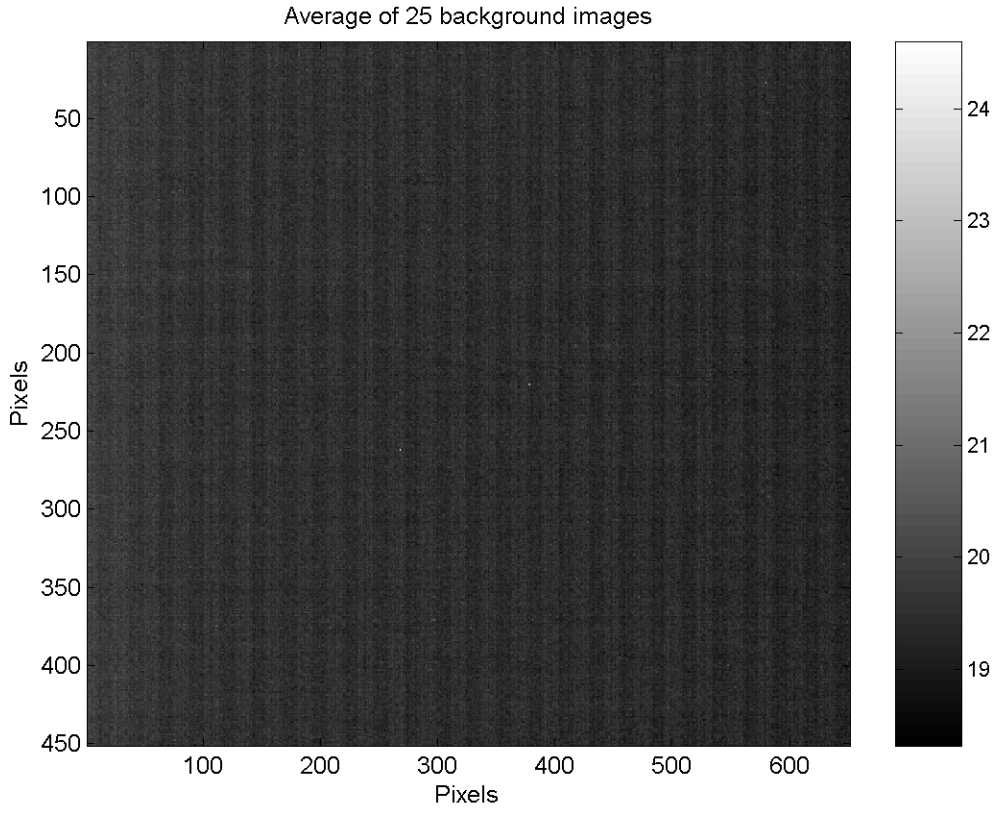

Fig. B3. Average of 25 noise background images. A persistent "foot-ball field" pattern can be seen.

The power spectrum of the single image noise background is shown in Fig. B4. The strong mean value signal has been forced to zero to enhance the nonzero frequency content of the spectrum. The square-root of the spectrum has been taken to enhance the low-value signals. The same power spectrum enhancement is applied to the power spectrum of the averaged 25 noise background images, see Fig. B5. Comparing Fig. B4 and Fig. B5, all of the major peaks are found in the two spectra. The maximum frequency of 0.5 (units 1/pixel) is the Nyquist frequency for a sampling interval of one pixel.
If the foot-ball field pattern is perfectly vertical with a period of 20 pixels, i.e. a square wave in the horizontal (x) direction, then the spectrum would contain five peaks at fy = 0 and fx = 0.05, 0.15, 0.25, 0.35, and 0.45 units 1/pixel.

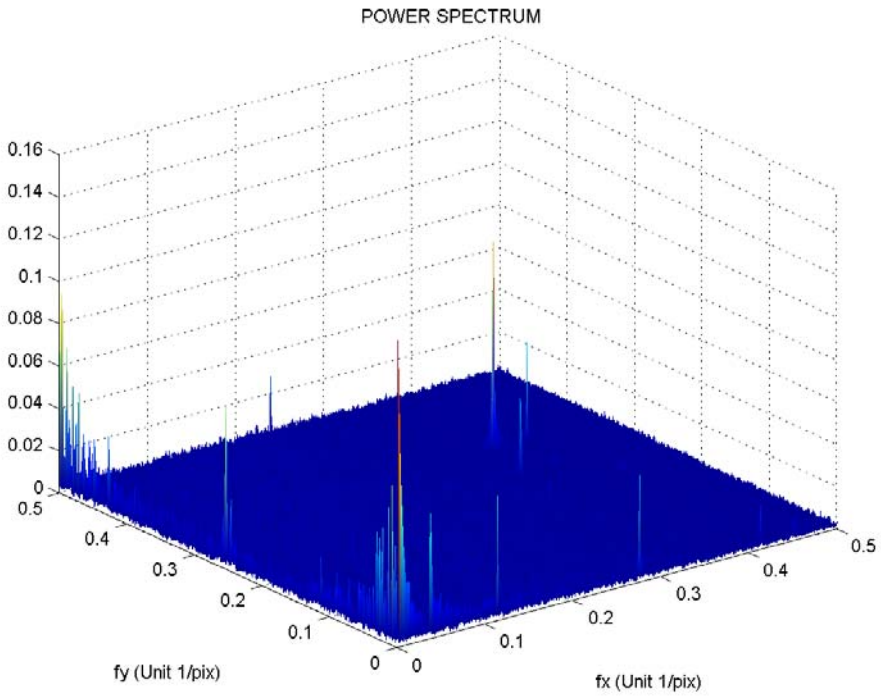

Fig. B4. Power spectrum of single image noise background.

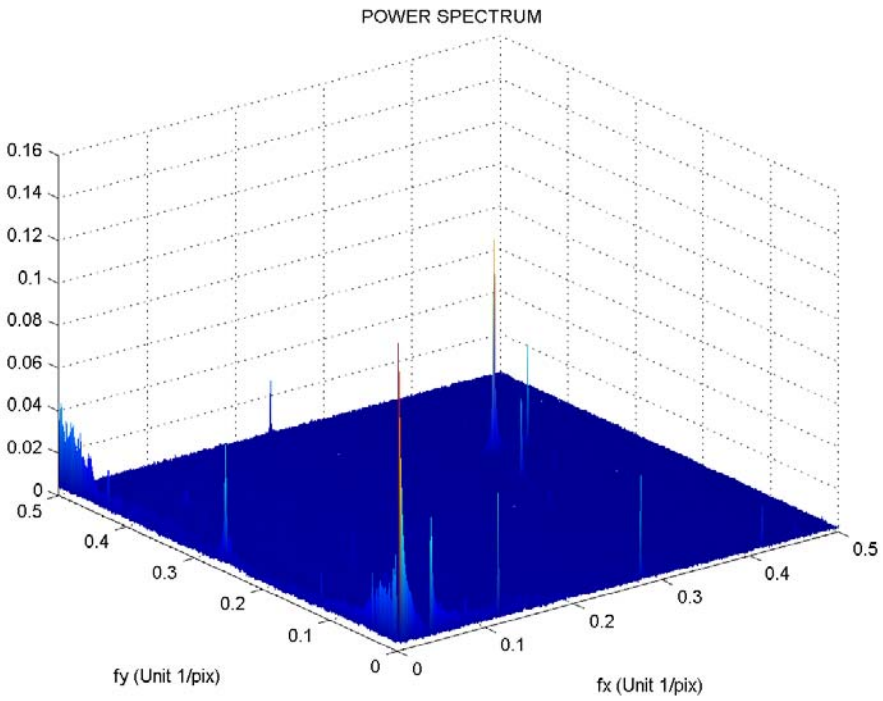

Fig. B5. Power spectrum of average of 25 noise background images.

The noise background elimination is done in the three-dimensional analysis program by digital image processing of a recorded image sequence. The noise offset of about 20 units 8 bit is subtracted from each image in the sequence of recorded two-dimensional images. The sum of the pixel profile is needed for the derivation of the range, see Eq. 5.2, Sec. 4.2, [Busck et al. 2004a-b]. After subtraction of the background the sum may be close to zero or zero, which cause a problem by division. Therefore a threshold value is introduced. If the sum of the pixel profile is smaller than the threshold the pixel is cut out of the analysis and can not contribute to the three-dimensional image.
Alternatively, the noise background offset subtraction does not have to be done by the analysis program. The black level of the frame-grabber can be raised to the voltage level of the noise background output from the camera, which would reduce program operations and speed up the image sequence processing. It has been observed that the noise background output from the camera is 0.1 V.

Appendix C - Scattering phase function model

The scattering phase function model proposed by the Canadians, [Forand et al. 1999], is presented with the remarkable outcome that the scattering coefficient is inversely dependent on the wavelength of light, (Eq. C5 below). In Chap. 7 the scattering phase function is utilized to analyze an underwater optical data set. With a scattering phase function fitted to the data set a point spread function can be determined by Monte-Carlo simulation. The point spread function can be applied in an image enhancement filter, which can improve the gated viewing laser images and therefore improve the sea-mine identification.

The model scattering phase function

$$\beta(\theta) = \beta_1(\theta) + \beta_1(\pi)\frac{3\cos^2(\theta)-1}{4}, \qquad \text{(C1)}$$

where θ is the angle of scattering from the direction of propagation, the second term on the right side arises from polarization effects and the first term is written

$$\beta_1(\theta) = \frac{1}{4\pi}\left(\frac{1}{(1-\delta)^2\delta^{\upsilon}}\right)\left(\upsilon(1-\delta)-(1-\delta^{\upsilon})+\frac{4}{u^2}\left[\delta(1-\delta^{\upsilon})-\upsilon(1-\delta)\right]\right) \qquad \text{(C2a)}$$

where

$$\upsilon = \frac{3-\mu}{2}, \qquad \delta = \frac{u^2}{3(n_r-1)^2}, \qquad u = 2\sin\left(\frac{\theta}{2}\right), \qquad \text{(C2b)}$$

where μ is the Junge coefficient of the particle size distribution, and n_r is the relative refractive particle index, i.e. relative to the refractive index of water. The value of the relative refractive particle index can be less than one, which means that the scattering phase function model does account for air bubbles.

Figure C1 shows a plot of the scattering phase function Eq. C1 for $n_r = 1.25$ and $\mu = 3.1$, 3.5, and 4.0. Figure C2 shows a surface color-plot of the scattering phase function at 100^o as function of the Junge coefficient μ, and relative refractive particle index n_r. When the Junge coefficient is close to three the scattering phase function is only weakly dependent on relative refractive particle index.

Notice the division by zero in Eq. C2a, when $\delta = 1$. This occurs at certain combined values of the relative refractive particle index n_r and the scattering angle θ

$$3(n_r-1)^2 = \left(2\sin\left(\frac{\theta}{2}\right)\right)^2 \qquad \Leftrightarrow \qquad \delta = 1, \qquad \text{(C3)}$$

for example, if $n_r = 2$ and $\theta = 120^o$ then $\delta = 1$.

It is observed that for certain combined values of the relative refractive particle index n_r and the Junge coefficient μ the scattering phase function is not valid. For example, if n_r = 1.25 and μ = 6, negative scattering values are predicted by the expression Eq. C1. In many cases the expression Eq. C1 predicts negative scattering if μ < 3.
The scattering coefficient

$$b(\lambda,\mu,n_r) = C\frac{\pi}{\cos(\pi\mu/2)}\left(\frac{2\pi(n_r-1)}{\lambda}\right)^{\mu-3}, \qquad \text{(C4)}$$

where C is a constant and λ is the wavelength.
Note the notation in this thesis is slightly changed from the notation of the reference [Forand et al. 1999]. The notation in this thesis is consistent with the very common use of "b" symbolizing the scattering coefficient.
Consider the scattering coefficient b in expression Eq. C4 divided by the scattering coefficient b_{ref} at a reference wavelength λ_{ref}

$$b(\lambda,\mu,n_r) = b_{ref}(\mu,n_r)\left(\frac{\lambda_{ref}}{\lambda}\right)^{\mu-3}. \qquad \text{(C5)}$$

The expression Eq. C5 is used to isolate the Junge coefficient, Sec. 7.3 above.

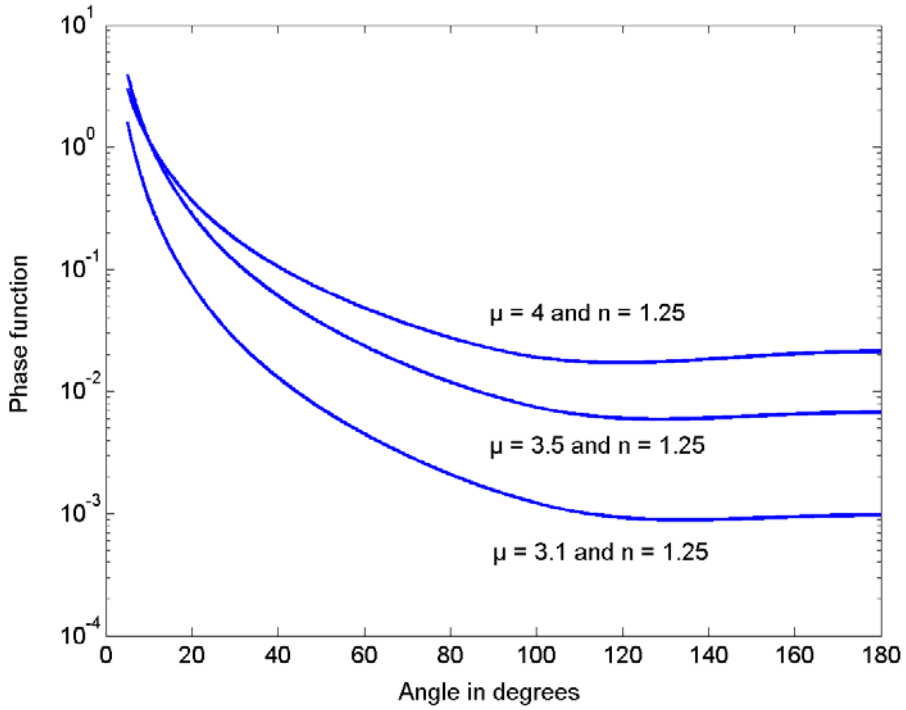

Fig. C1. Scattering phase function (Eq. C1) versus scattering angle 0°-180° for the values of relative refractive particle index n_r = 1.25 and the Junge coefficient μ = 3.1, 3.5, and 4.0. (Note that n should be n_r in the figure box).

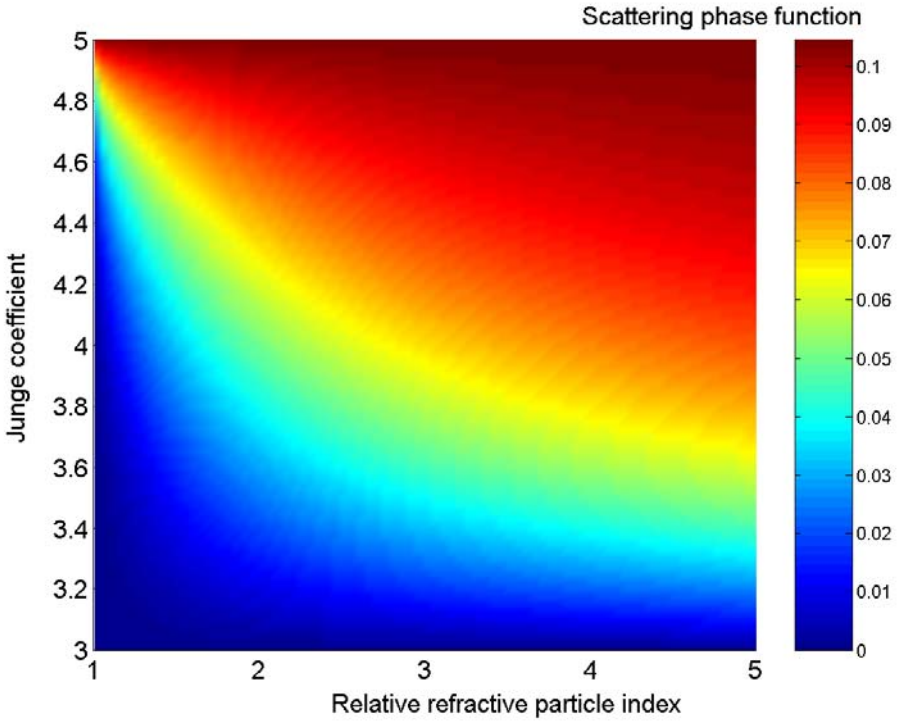

Fig. C2. Scattering phase function (Eq. C1) at θ = 100^{o} as function of the relative refractive particle index (n) and the Junge coefficient (μ). The color bar displays the scattering phase function values.

Appendix D – Sequence of 50 range gated images

This appendix displays a typical and complete sequence of 50 range gated images (Fig. D1), and the corresponding three-dimensional image (Fig. D2), recorded at 7 m range.

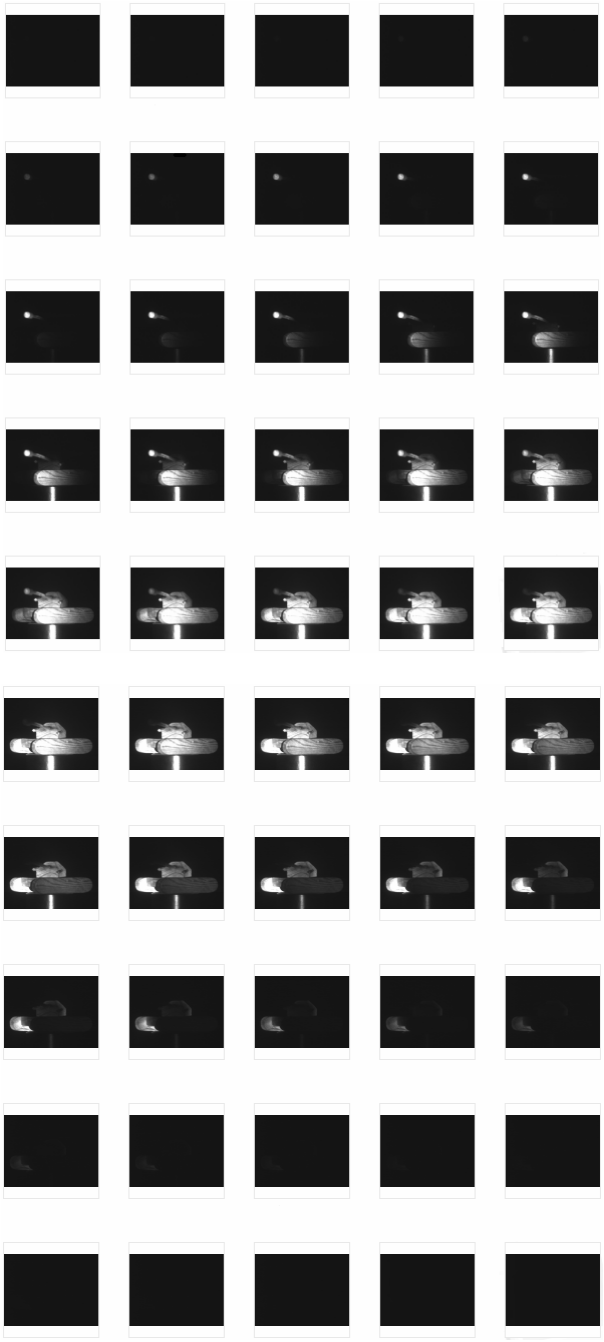

Fig. D1. Gated viewing three-dimensional laser radar image sequence of 50 range gated images. The camera gate time is 0.5 ns and the camera delay step is 0.1 ns. The range covered by the image sequence is approximately 50 × 0.1 ns × c/2 = 75 cm, where c is the speed of light. The range from the laser radar to the object is about 7 m.

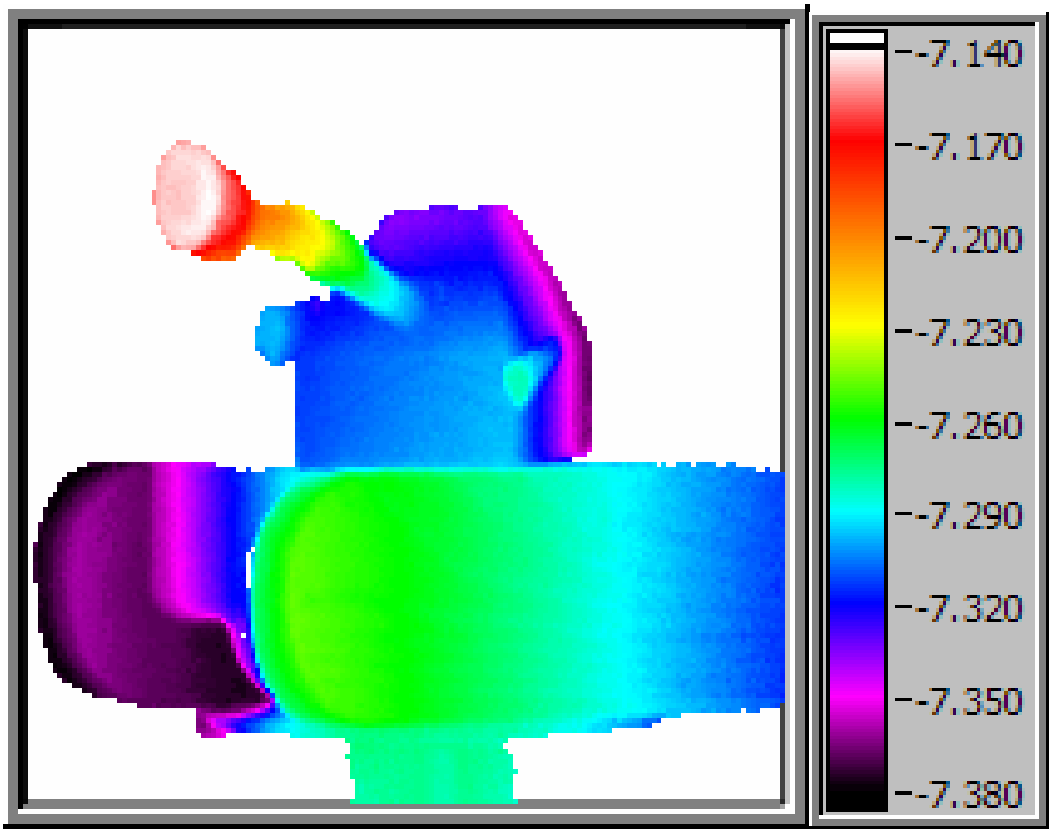

Fig. D2. Gated viewing three-dimensional laser radar image corresponding to the sequence of range-gated images in Fig. D1. The size of the object is about 20 cm. The color-coded range scale is in units of meters.

References

M. Acharekar, “Underwater laser imaging system (ULIS)”, Proc. SPIE, **3079**, 750-761, 1997.

G. P. Agrawal, “Non-linear fiber optics”, Academic Press, 3.edit. 2001.

M. A. Albota, R. M. Heinrichs, D. G. Kocher, D. G. Fouche, B. E. Player, M. E. O’Brien, B. F. Aull, J. J. Zayhowski, J. Mooney, B. C. Willard, and R. R. Carlson, “Three-dimensional imaging laser radar with a photon-counting avalanche photodiode array and microchip laser”, *Appl. Opt.*, **41**, 7671-7678, 2002.

K. Aliberti, W. Ruff, H. Shen, P. Newman, M. Giza, W. Sarney, M Stead, J. Damman, R. Mehandru, and F. Ren, “Characterization of InGaAs self-mixing detectors for chirp, amplitude modulated LADAR (CAML)”, Proc. SPIE, **5412**, 99-110, 2004.

R. L. Allwood and S. Tetlow, “Improvement of underwater viewing range by the use of a scanning laser-based illuminator”, 7th Int. Conf. Elec. Eng. Ocean. Proc. IEE, No. 439, 53- 61,1997.

J. F. Andersen, J. Busck, and H. Heiselberg, “Long distance high accuracy 3-D laser radar and person identification”, (submitted to SPIE Defense & Security Symposium, Orlando, USA, 2005).

R. W. Austin, S. Q. Duntley, R. L. Ensminger, T. J. Petzold, and R. C. Smith, “An underwater laser scanning system”, Proc. SPIE, **1537**, 57-73, 1991.

M. L. Bjarnar, J. O. Klepsvik, and J. E. Nilsen, “Modeling and experiments with a sub-sea laser radar system”, Proc. SPIE, **1537**, 74-88, 1991.

G. D. Boreman, and S. Yang, “Modulation transfer function measurement using three- and four- bar targets”, *Appl. Opt.*, **34**, 8050-8052, 1995.

J. Busck, “Simulation of gated viewing mono-static three-dimensional laser radar”, *Opt. Eng.*, submitted Dec. 2004.

J. Busck and H. Heiselberg, “Gated viewing and high-accuracy three-dimensional laser radar,” *Appl. Opt.*, **43**, 4705-4710, 2004(a).

J. Busck and H. Heiselberg, “High-accuracy three-dimensional laser radar,” Proc. SPIE, **5412**, 257-263, 2004(b).

K. Buskila, S. Towito, E. Shmuel, R. Levi, N. Kopeika, K. Kraples, R. G. Driggers, R. H. Vollmerhausen, and C. E. Halford, “Atmospheric modulation transfer function in the infrared”, *Appl. Opt.*, **43**, 471-482, 2004.

M. J. Chantler, J. Clark, and M. Umasuthan, “Calibration and operation of an underwater laser triangulation sensor: the varying baseline problem”, *Opt. Eng.*, **36**, 2604-2611, 1997.

B. W. Coles, W. Radzelovage, P. J. Laurant, and K. Reihani, “Processing techniques for multi-spectral laser line scan images”, IEEE, Proc. Oceans, 1766-1779, 1998.

J. C. Dries, B. Miles, and R. Stettner, “A 32×32 pixel FLASH laser radar system incorporating InGaAs PIN and APD detectors”, Proc. SPIE, **5412**, 250-256, 2004.

A. Ducharme, “MTF in optical and electro-optical systems”, short course notes (SC157), SPIE, 2004.

G. C. Ewing, “Oceanography from space”, WHOI Ref. No. 65-10, Woods Hole Ocean. Ins. USA, 1965.

J. L. Forand and G. R. Fournier, “Particle distributions and index of refraction estimation for Canadian waters”, Proc. SPIE, **3761**, 34-44, 1999.

G. R. Fournier and M. Jonasz, “Computer based underwater imaging analysis”, Proc. SPIE, **3761**, 62-70, 1999.

G. R. Fournier and J. L. Forand, “Analytic phase function for ocean waters”, Proc. SPIE, **2258**, 194-201, 1994.

G. R. Fournier, D. Bonnier, J. L. Forand, and P. W. Pace, “Range-gated underwater laser imaging system”, *Opt. Eng.*, **32**, 2185-2190, 1993.

C. S. Fox, (Ed.), “Active electro-optical systems”, IR/EO Systems Handbook, vol. 6, SPIE Press, 1996.

H. G. Gierloff-Emden, N. K. Højerslev, G. Krause, H. Peters, G. Siedler, G. Weichart, and P. Wille, “Oceanography”, Springer-Verlag, **3**, 1986.

A. Gleckler, and A. Gelbart, ”Three-dimensional imaging polarimetry”, Proc. SPIE, **4377**, 175-185, 2001.

A. D. Gleckler, “Multiple-slit streak tube imaging lidar (MS-STIL) applications”, Proc. SPIE, **4035**, 266-278, 2000.

A. Gleckler, “Underwater 3D imaging technique identifies bottom mines”, interview in OE Reports no.183, SPIE, 1999.

R. C. Gonzales, and R. E. Woods, “Digital image processing”, Prentice Hall, 2.edit. 2002.

R. C. Gonzales, and P. Wintz, “Digital image processing”, Addison Wesley, 2.edit. 1987.

D. M. He, and G. G. L. Seet, “Underwater lidar imaging scaled by 22.5 cm/ns with serial targets”, *Opt. Eng.*, **43**, 754-766, 2004.

D. M. He, and G. G. L. Seet, “Underwater lidar imaging in highly turbid waters”, Proc. SPIE, **4488**, 71-81, 2002.

A. K. Jain, “Fundamentals of digital image processing”, Prentice Hall, 1989.

L. Klasen, P. Andersson, H. Larsson, T. Chevalier, and O. Steinvall, “Aided target recognition from 3-D laser radar data”, Proc. SPIE, **5412**, 321-332, 2004.

J. L. Lagaye, L. Vinay, and J. Richou, ” Improvement of lidar system by modulation of an optical pulse laser for underwater detection”, Proc. SPIE, **3100**, 417-422, 1997.

R. Lange and P. Seitz, “Seeing distances – a fast time-of-flight 3D camera”, *Sensor Review*, **20**, 212-217, 2000.

D. Maddalena, M. Zampato, and M. Favaretto, “A stereovision system for underwater, remotely operated vehicles”, *Sensor Review*, **18**, 121-128, 1998.

M. Marchywka and D. G. Socker, “Modulation transfer function measurement technique for small-pixel detectors”, *Appl. Opt.*, **31**, 7198-7213, 1992.

J. W. McLean and J. T. Murray, “Streak-tube lidar allows 3-D ocean surveillance”, *Laser Focus World*, 171-176, Jan. 1998.

J. W. McLean and J. D. Freeman, “Effects of ocean waves on airborne lidar imaging”, *Appl. Opt.*, **35**, 3261-3269, 1996.

L. J. Mullen, A. Laux, B. Concannon, E. P. Zege, I. L. Katsev, and A. S. Prikhach, “Amplitude-modulated laser imager”, *Appl. Opt.*, **43**, 3874-3892, 2004.

L. J. Mullen, and V. M. Contarino, “Hybrid lidar-radar: Seeing through the scatter”, Microwave (IEEE), 42-48, Sept. 2000.

L. J. Mullen, V. M. Contarino, A. Laux, B. Concannon, J. Davis, M. Strand, and B. Coles, “Modulated laser line scanner for enhanced underwater imaging”, Proc. SPIE, **3761**, 2-9, 1999.

L. J. Mullen, V. M. Contarino, and P. R. Herczfeld, “Hybrid lidar-radar ocean experiment”, *IEEE Trans. Microwave Theory Tech.*, **44**, 2703-2710, 1996.

A. Nevis, R. J. Hilton, S. J. Taylor, B. Cordes, and J. W. McLean, “The advantages of three-dimensional electro-optic imaging sensors”, Proc. SPIE, **5089**, 225-237, 2003.

A. Nevis, “Automated processing for streak tube imaging lidar data”, Proc. SPIE, **5089**, 119-129, 2003.

A. Nevis, J. Bryan, J. S. Taylor, and B. Cordes, “An algorithm for detection of mine-like objects using streak tube imaging lidar data”, submitted to Ocean Optics, (personal paper without page numbers), 2002.

F. Pellen., P. Olivard, Y. Guern, J. Cariou, and J. Lotrian, “Radio-frequency modulation on optical carrier for target detection enhancement in seawater”, proc. SPIE, **4488**, 13-24, 2002.

F. Pellen., P. Olivard, Y. Guern, J. Cariou, and J. Lotrian, “Radio-frequency modulation on optical carrier for target detection enhancement in seawater”, *J. Phys. D: Appl. Phys.*, **34**, 1122-1130, 2001.

F. Pellen, Y. Guern, P. Olivard, J. Cariou, and J. Lotrian, “Loss of radio frequency modulation on optical carrier in high scattering medium: effects of multiple scattering and field of view selection”, *J. Phys. D: Appl. Phys.*, **34**, 49-51, 2001.

B. Redman, W. C. Ruff, and K. Aliberti, “Direct detection laser vibrometry with an amplitude modulated ladar”, Proc. SPIE, **5412**, 218-228, 2004.

G. L. Rogers, “Measurement of the modulation transfer function of paper”, *Appl. Opt.*, **37**, 7235-7240, 1998.

E. Saade, N. Estabrook, and D. Carey, ”Recent applications of laser line scan technology and data processing”, Science applications International Corporation (SAIC), 190-195, 1994.

H. Sakai, J. Akizono, S. Yasumura, and Y. Takahashi, “Underwater laser viewing system and its application”, IEEE, 161-167, 1998.

B. E. A. Saleh, and M. C. Teich, “Fundamentals of photonics,” Wiley Inter-Science, 1991.

B. W. Schilling, D. N. Barr, G. C. Templeton, L. J. Mizerka, and C. W. Trussell, “Multiple-return laser radar for three-dimensional imaging through obscurations”, *Appl. Opt.*, **41**, 2791-2799, 2002.

D. N. Sitter, J. S. Goddard, and R. K. Ferrell, “Method for the measurement of the modulation transfer function of sampled imaging systems from bar-target patterns”, *Appl. Opt.*, **34**, 746-751, 1995.

O. Steinvall, L. Klasen, C. Grönvall, U. Söderman, S. Ahlberg, Å. Person, M. Elmqvist, H. Larsson, D. Letalick, P. Andersson, T. Carlsson, and M. Henriksson, "3D laser sensing at FOI – overview and a system perspective", Proc. SPIE, **5412**, 294-309, 2004.

O. Steinvall, L. Klasen, T. Chevalier, P. Andersson, H. Larsson, M. Elmqvis, and M. Henriksson, "Grindad avbildning – fordjupad studie", (Gated viewing – preliminary study), FOI-R-0991-SE, Swedish Defence Research Agency, Linköbing, Sweden, 2003.

O. Steinvall, "Effects of target shape and reflection on laser radar cross section", *Appl. Opt.*, **39**, 4381-4391, 2000.

R. Stettner, H. Bailey, and R. Richmond, "Eye-safe laser radar 3-D imaging", Proc. SPIE, **5412**, 111-116, 2004.

R. H. Stolen, C. Lee, and R. K. Jain, "Development of the stimulated Raman spectrum in single-mode silica fibers", *J. Opt. Soc. Am.*, **1**, 652-657, 1984.

M. P. Strand, "Fluorescence imaging laser line scan (FILLS) for very shallow water mine countermeasures", IEEE, conf. Oceans, 2001.

M. P. Strand, "Imaging model for underwater range-gated imaging system", Proc. SPIE, **1537**, 151-160, 1991.

B. A. Swartz, and J. D. Cummings, "Laser range-gated underwater imaging including polarization discrimination", Proc. SPIE, **1537**, 42-56, 1991.

J. R. Taylor, "An introduction to error analysis", University Science Books, 2.edit. 1997.

S. Tetlow and J. Spours, "Three-dimensional measurement of underwater work sites using structured laser light", *Meas. Sci. Tech.*, **10**, 1162-1167, 1999.

A. D. Wiedemann, G. R. Fournier, J. L. Forand, P. Mathieu, and S. Mclean, "Laser underwater camera image enhancer for mine warfare applications: what is gained?", (Note: Personal unpublished paper).

L. Zhishen, Y. Yifan, Z. Kailin, and H. Hailong, "Underwater image transmission and blurred image restoration", *Opt. Eng*. **40**, 1125-1131, 2001.

Other references

"Den Store Danske Encyklopædi" (the large Danish Encyclopedia), digital version 1, Gyldendalske Boghandel, Nordisk Forlag, Denmark, 2004.

"Instructions for InstaSpec™ II Photodiode Array Detector Model 77112", Spectrometer instruction manual, Oriel Corporation, USA, 1994.

Matlab digital documentation, version 6.5.0.180913a, release 13, 2002.

Labview digital documentation, version 7.0, 2003.

Gated viewing and high-accuracy three-dimensional laser radar

Jens Busck and Henning Heiselberg

We have developed a fast and high-accuracy three-dimensional (3-D) imaging laser radar that can achieve better than 1-mm range accuracy for half a million pixels in less than 1 s. Our technique is based on range-gating segmentation. We combine the advantages of gated viewing with our new fast technique of 3-D imaging. The system uses a picosecond Q-switched Nd:Yag laser at 532 nm with a 32-kHz pulse repetition frequency (PRF), which triggers an ultrafast camera with a highly sensitive CCD with 582 × 752 pixels. The high range accuracy is achieved with narrow laser pulse widths of approximately 200 ps, a high PRF of 32 kHz, and a high-speed camera with gate times down to 200 ps and delay steps down to 100 ps. The electronics and the software also allow for gated viewing with automatic gain control versus range, whereby foreground backscatter can be suppressed. We describe our technique for the rapid production of high-accuracy 3-D images, derive performance characteristics, and outline future improvements.

OCIS codes: 010.3640, 100.0100, 110.6880, 150.0150, 280.3420, 280.3640.

1. Introduction

Remote sensing in electro-optics has developed rapidly owing to ultrafast lasers, cameras, detectors, and electronics. An important application is fast and high-accuracy gated viewing, which is used for accurate laser ranging and for the removal of backscatter from such obscurants as fog, camouflage[1–3] or water.[4–6] In addition, three-dimensional (3-D) imaging that improves target recognition and detection is now possible.

Recent techniques exploiting these technologies have produced an increase in pixels and timing resolution, resulting in a much-improved resolution in (x, y) and range, respectively. Typically, they apply nanosecond lasers and gigahertz electronics and therefore have range resolutions of a few centimeters to meters.[1–6] The speed of 3-D imaging depends on the number of pixels, but typically 10^3–10^5 pixels take seconds to minutes to process. Generally, one obtains better 3-D resolution by collecting light over a longer time, and at shorter distances, with larger optics, more powerful laser illumination, and sensitive detectors. Lasers and detectors cover a wide range of wavelengths, from UV to optical to IR. High-speed detectors exist in optical and near-IR regions, and recently the United States Army and Air Force have developed a high-speed electron-bombarded CCD detector at the eye-safe IR wavelength around 1.5 μm (Ref. 2).

We have developed a fast and high-accuracy 3-D imaging laser radar with better than 1-mm range accuracy in half a million pixels. We present a novel processing approach to convert a sequence of two-dimensional (2-D) images into 3-D imagery. The 3-D laser radar concept is based on gated viewing and employs a picosecond pulsed laser that illuminates a 3-D scene. Each laser pulse triggers a camera with a highly sensitive microchannel plate (MCP). The MCP acts as both an amplifier and a shutter, so that a number of laser pulses are integrated on a CCD. Sequences of range-gated 2-D images are then recorded from which 3-D images are constructed (see Fig. 1).

We describe our equipment in Section 2 and our sequential range-gating technique for the rapid production of high-accuracy 3-D images in Section 3, where also the performance characteristics are discussed and are compared with images taken with our laser radar. Range gating is described in Section 4. Conclusions and predictions of future improvements are given in Section 5.

The authors are with the Electro-Optical Section, Danish Defense Research Establishment, Ryvangs Alle 1, DK-2100 Copenhagen Ø, Denmark. J. Busck (jb@ddre.dk) is also with Electronics and Signal Processing, Technical University of Denmark, Ørsteds Plads, Building 349, DK-2800, Lyngby, Denmark.

Received 29 October 2003; revised manuscript received 2 April 2004; accepted 21 May 2004.

0003-6935/04/244705-06$15.00/0

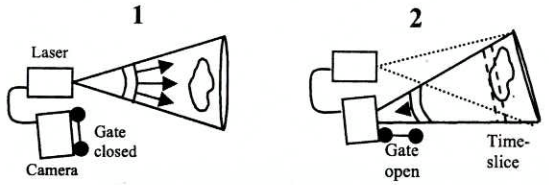

Fig. 1. Gated viewing technique. The laser emits a pulse and triggers the camera with a delay and a gate time, which determine when and how long the camera gate opens. Approximately 650 laser pulses are integrated in each time slice after the delay is changed [sliding, as given by Eq. (1)]. Each time slice is read out within 50-Hz video mode, i.e., the pulse repetition frequency is equal to 50 time slices per second × 650 laser pulses per time slice, or 32.5 kHz.

2. System Description

We have designed the system, electronics, and software to maximally exploit the picosecond pulsed laser that triggers an equally fast camera. We exploit the PRF by collecting a large number of pulses on an MCP, thereby improving the signal to noise ratio (SNR). The wavelength of 532 nm is chosen for later studies under water, where transmission is maximal in the green part of the optical spectrum, and it allows for testing above water, although it is not eye safe at short distances. Also, standard detectors have high quantum efficiency in the green part of the optical spectrum.

A. Laser

The laser is a diode-pumped passively Q-switched Nd:Yag microchip laser at 532 nm with a narrow pulse width of ~200 ps and a high PRF of 32.4 kHz. The average energy per pulse is 4.3 μJ, which provides an average power of 140 mW.

B. Camera

The high-speed 8-bit camera has gate times down to 200 ps and delay step times down to 100 ps. The photocathode material S20Q spectral response is from 110 to 800 nm. The camera contains a CCD chip with 582 × 752 pixels, 4.5 mm × 6.0 mm, and a highly sensitive MCP with a quantum efficiency around 20% in the green region. The optics used to capture the figures below (Figs. 3–6), includes a reflector with an 8-cm-diameter lens and a focal length of 500 mm. Generally, we adjust various optics in the camera as well as in front of the laser to match the target field of view and field of illumination, respectively.

C. Trigger Electronics

The camera is triggered by each individual laser pulse through a direct laser-to-camera connection. The MCP acts as a shutter, and a number of pulses can be integrated on the CCD, thereby utilizing the high PRF. Owing to a delay of ~85 ns in the camera trigger electronics, the laser pulses are sent through a 30-m optical fiber so that range gating is also possible at short distances. A series of pulses are then integrated on the MCP before a 2-D image (one gated viewing time slice) is read out. Typically, the interval between readout times is ~20 ms, i.e., a 50-Hz read-out frequency. When PRF = 32.4 kHz the number of pulses integrated on each time-slice image is $N_{\text{puls}} = 650$. Before each new time slice, the camera is fed with the new delay within a few milliseconds. During this period, the camera gate is closed, and the emitted laser pulses are ignored. Gain and other settings can be changed, which is very useful for suppression or enhancement of certain time slices.

D. Data Acquisition and Software

The prestorage data processing is done in LABVIEW. The 2-D images are weighted with image number and are summed in order to obtain the range, as explained in detail in Subsection 3.A. To save time and disc space we have set a default option to save only the 2-D images and the range image to disk. A typical sequence of ~50 gated time slices thus takes ~1 s to record, analyze, and produce a 3-D image. If the target or the laser radar platform moves more than the 3-D resolution within this time, the pictures will be dynamically smeared. This may be compensated for with shorter and fewer time slices (however, with corresponding reduced intensities) or by postprocessing for image reconstruction.

3. Time-Slicing Technique

In the standard setup the camera is gated such that it is open for a time t_{gate} and with a time delay after pulse emission of

$$t_i = t_0 + i\Delta t. \tag{1}$$

Here t_0 is the initial delay, and the sequence of delays runs $i = 1, 2, \ldots, N$, where N is the number of 2-D images, or time slices, in the sequence. Δt is the delay step time, which can be chosen independently of the time the camera is open, t_{gate}. For our fast camera the minimal delay step time is $\Delta t = 100$ ps, corresponding to a minimal step distance $c\Delta t/2 = 1.5$ cm. For example, a readout of a sequence of $N = 50$ time slices (within 1 s) and step of 200 ps per step covers a range of 1.5 m in depth. The minimal gate time possible in the camera is $t_{\text{gate}} = 200$ ps, but a larger gate time of order of the pulse width is optimal, because the laser pulse width limits the time-step resolution.

The laser pulse is approximately given by a Gaussian form

$$P(t) = \frac{P_0}{\sqrt{2\pi}\sigma_{\text{pulse}}} \exp(-t^2/2\sigma_{\text{pulse}}{}^2). \tag{2}$$

The pulse width σ_{pulse} has been measured to be approximately 2–300 ps, and P_0 is the maximum radiant pulse energy received in a given pixel in the camera. It is given by the standard laser radar range equation[7] and depends on the total laser pulse energy, the beam divergence, the distance to the object and its laser cross section, the atmospheric trans-

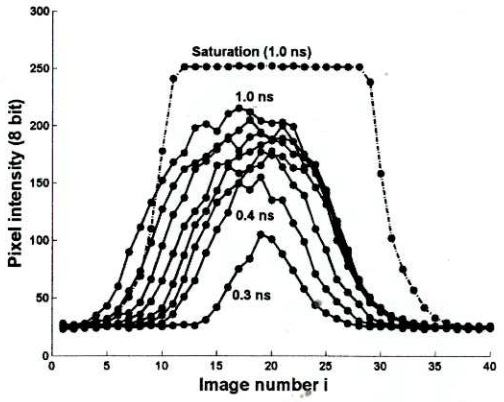

Fig. 2. Measured curves I_i [from Eq. (3)], with time step $\Delta t = 100$ ps but different camera gates: $t_{\text{gate}} = 0.3, 0.4, \ldots, 1.0$ ns. The amplitude of the 0.3-ns curve is relatively small, because the camera gate starts to close before it is fully open. When the gate time is increased the laser pulses can make it back in earlier time slices, and therefore the intensity curves extend to a smaller image number. The background value is ~25 and will be subtracted in further analysis.

mission, the receiver aperture and focal length, the CCD and MCP chip size and sensitivity, etc.

Ideally, the gate opening is a step function; $G(t) = 1$, for $|t| < \Delta t/2$, and zero otherwise. However, owing to jitter in the shutter and trigger delays, the gate opening function $G(t)$ averaged over many pulses is a smeared version of the ideal gate function. However, the gate function and the pulse form are individually required to make a 3-D image. The curves in Fig. 2 from which we extract the range (3-D) information are the convolution of the gate function and the pulse form. Note that the convolution is a result of range grating the reflected laser pulses and not a result of mathematical processing.

The radiant energy of light received from the laser pulse is the incident radiant energy of the pulse integrated during the gate time where the camera is open:

$$I_i = \int P(t - 2r/c)G(t - t_i)\mathrm{d}t. \tag{3}$$

Here, the pulse is delayed by the round-trip travel time $2r/c$ at a range where $r = (x^2 + y^2 + z^2)^{1/2} \approx z$, as seen in pixel (x, y). The camera gate is delayed by the time t_i sequentially, as given in Eq. (1). The sequence of time slices or range gates I_i is recorded for all (x, y) pixels, and each I_i is a 582×752 matrix. Typical curves are shown in Fig. 2 for a single pixel. The curves differ only by gate width, except the curve that is a result of pixel saturation. The absolute range derived by the technique from the laser radar to the target is dependent on delay step size and gate width. For example, the range decrease with gate time as $ct_{\text{gate}}/4$, as can also be seen in Fig. 2. Such corrections are not necessary for the relative 3-D image but are necessary for obtaining the accurate absolute distance to the target.

Fig. 3. Image of $I(x, y)$ at the range of 13.55 m of a 15-cm-high doll's head.

A. Summation of 2-D Images

By summing the 2-D images $i = 1, 2, \ldots, N$, we obtain the (2-D) summed image $I(x, y) = \Sigma I_i(x, y)$. When the delay-time steps are much smaller than the pulse width or the gate opening time, we can replace the sum over segments by an integral over delay times: $\Sigma I_i \rightarrow \int \mathrm{d}t_i/\Delta t$. It then follows from Eqs. (1)–(3) that

$$I = \sum_i I_i \cong \frac{t_{\text{gate}}}{\Delta t} P_0.$$

This illustrates that the summed image pixel values are proportional to the integrated pulse energy and the gate time and are inversely proportional to the time step.

In Fig. 3 we show a 2-D image I of a doll taken from a distance of ~13.5 m. The doll's head is 15 cm high. The gain has been adjusted so that only a few pixels in the eyes and at the lower face are saturated.

B. Range

The average two-way travel time $\langle t \rangle$ to an object point within the field of view of a pixel is given by the weighted average

$$\langle t \rangle = \frac{2r}{c} = I^{-1} \sum_i I_i t_i, \tag{4}$$

where $I_i = I_i(x, y)$ is the x, y pixel value in the ith image in a sequence of 2-D images. Note that in general $\langle t \rangle = \langle t(x, y) \rangle$, $I = I(x, y)$ and $r = r(x, y)$ depend on the pixel (x, y), whereas t_i does not. The range $r = \langle t \rangle c/2$ corresponding to the image of Fig. 3 is shown in Figs. 4–5.

A background is automatically subtracted in all pixels. This background consists of dark current and light deflection from aerosols. A good part of both deflection and backscatter within each range-gated image are removed by adjusting the back-

Fig. 4. The image of Fig. 3 wrapped onto a 3-D image recorded by the time-slicing technique described in the text. The 3-D image is then computer rotated by 60° to the side. Camera gate time is 400 ps, and delay step is 100 ps. Note: the range deviation of the eye pixels is strongly related to the pixel SNR, the subtracted background, the noise, and the timing of the 2-D image sequence.

ground to the conditions. In media with large backscatter, e.g., fog or water, the background is varied with distance and thus a larger fraction of deflected light is removed.

C. Variance

Higher moments of the travel time also contain important information. For example, the second moment

$$\langle t^2 \rangle = I^{-1}\left(\sum_i I_i {t_i}^2 \right) \tag{5}$$

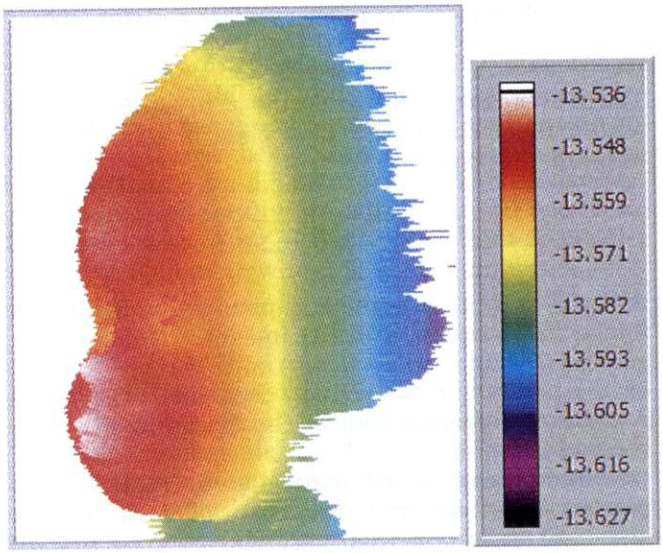

Fig. 5. Rotated range (r) image. The range in meters is color coded.

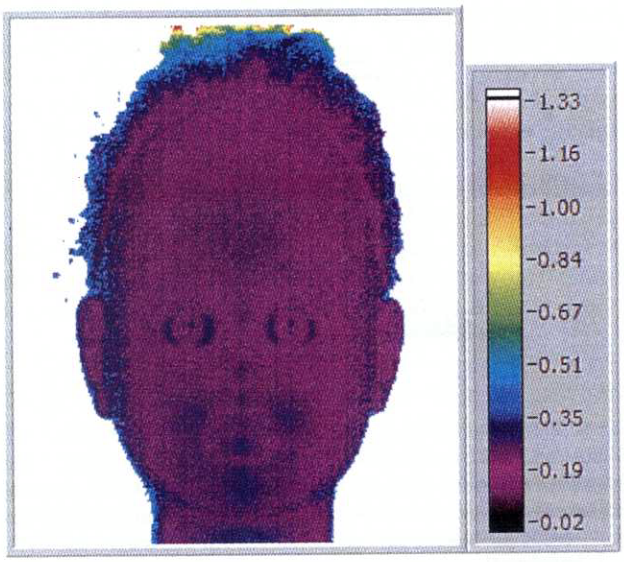

Fig. 6. Variance (σ^2) image. The variance is color coded in units of square nanoseconds.

gives a very useful quantity, namely the variance of the travel time, which is the variance of the curves of Fig. 2:

$$\sigma^2 = \langle t^2 \rangle - \langle t \rangle^2 = (\Delta t)^2(\langle i^2 \rangle - \langle i \rangle^2), \tag{6}$$

where i is the image number, Δt is the delay step, and $\langle i^n \rangle = (\Sigma I_i i^n)/(\Sigma I_i)$ is the weighted average analogous to Eq. (5).

When the delay-time steps are sufficiently small so that we can replace the sum by an integral, we obtain

$$\sigma^2 = \langle t^2 \rangle - \langle t \rangle^2 \cong {\sigma_{\text{pulse}}}^2 + {\sigma_{\text{gate}}}^2. \tag{7}$$

Equation (7) shows that the variance in the delay times is simply the sum of variances of the pulse and the gate function ${\sigma_{\text{gate}}}^2$. For the ideal step gate function its variance is $(\sigma_{\text{gate}})^2 = \int t^2 dt / \int dt = (t_{\text{gate}})^2/12$, where the integrations run between $\pm t_{\text{gate}}/2$. In practice, the gate variance is larger because the gate function is wider owing to jitter and noise. The measured variance σ^2 is shown in Fig. 6. It takes its minimal value of $\sigma^2 \approx (400\ \text{ps})^2$ at the bright surfaces but is larger in dark areas where background noise is significant.

Narrow laser pulses, short gate times, and good control of trigger and camera gating, which reduce jitter, are all responsible for the small σ of ~400 ps. One also observed in Fig. 6 that the variance is larger in saturated pixels, e.g., in the white part of the eyes. This follows from the saturated curve in Fig. 2, which has a much wider distribution of time slices.

An important range and variance effect occurs when the summed pixel value $I(x, y)$ drops down into the background noise level. This typically occurs in the pixels near the edge of rounded objects, where $I(x, y)$ drops down. Dividing by small values of $I(x, y)$, which can be a small number that is positive, negative or zero after subtraction of background, causes an obvious problem in Eqs. (4) and (5). To

avoid dividing by a small number we introduce a threshold value of $I(x, y)$ below which the distance cannot be reliably determined, and the pixels are simply removed from the 3-D image. However, these threshold pixels can also be included in the images whereby the contours are emphasized, because of the large range and variance deviation induced by dividing with a small number. By varying the threshold value, various contour lines in range can be plotted. These contours can in turn be exploited for detection, classification, and identification in 2-D as well as 3-D. Note that in the figures presented in this paper the threshold pixels are all removed automatically.

D. Range Accuracy

As deduced from Fig. 2 the accuracy in determining the mean travel time $\langle t \rangle$ from the sequence of $I_i(x, y)$ is much better than the width σ of the curve of $I_i(x, y)$ when the SNR is high. The width of the distribution gives a resolution of approximately $c\sigma/2 \approx 6$ cm in each pixel, but by taking a sequence of $I_i(x, y)$ we shall now demonstrate that the range accuracy becomes better than 1 mm.

Define the average SNR as $\mathrm{SNR} \approx I/[\Sigma\ (\Delta I_i)^2]^{1/2}$. If the noise ΔI_i is random, i.e., $(\Delta I_i)^2 \approx I_i$, then we find that

$$\mathrm{SNR}^2 = I = \frac{\sigma}{\Delta t} \max(I_i), \tag{8}$$

where the factor $\sigma/\Delta t$ is simply the number of time slices that contribute to the sum I. For example, near saturation $\max(I_i) = 2^8$ and with $\sigma = 400$ ps and $\Delta t = 100$ ps, we obtain $\mathrm{SNR} = 32$.

The uncertainty in $\langle t \rangle$ can be calculated from its definition, Eq. (4), by standard error analysis. The corresponding range accuracy in determination the range $r = \langle t \rangle c/2$ becomes

$$\Delta r \cong \frac{1}{2} \frac{c\sigma}{\mathrm{SNR}}, \tag{9}$$

where $\Delta r \approx 2$ mm, with the above parameters. The fact that the corresponding uncertainty in the range $r = \langle t \rangle c/2$ is less than ~1 mm under optimal conditions with high SNR has been experimentally verified.

It should be emphasized that the SNR generally increases proportionally to the square root of the number of pulses that are integrated on the MCP for each I_i in each pixel. In Fig. 2, each time-slice pixel value is a sum over ~650 laser pulses. The high PRF and the resulting large number of pulses summed are essential for the high SNR and the range accuracy.

In the range accuracy of Eq. (9), only the SNR depends on the distance to the object. The speed of light is given by the medium, e.g., air or water, in which the light propagates. The variance σ^2 is a system parameter that depends on the camera gate time and the laser pulse width. The SNR, however, generally decreases with the square root of the detected light. For a fixed field of view and field of illumination the detected light drops as r^{-2}, and thus SNR drops as approximately r^{-1}. The range accuracy of 1 mm at a distance of 10 m therefore drops to ~1 cm at 100 m. We can, however, compensate by increasing the detector gain or the camera gate times by taking a longer sequence or by narrowing the field of view and field of illumination.

E. Higher Moments and Saturation

Sequences with higher moments of the travel time contain additional information on the details of the laser pulse and the gate function. For example, the third moment $\Sigma\ I_i(t_i)^3/I$ is related to the asymmetry of the curves in Fig. 2. When a pixel saturates, its range moves relative to the true range by an amount proportional to the skewness and the degree of saturation, and the error can be corrected for. Therefore saturation does not necessarily degrade the range determination, although the 2-D images are degraded.

4. Range Gating and Resolution

The range-gating technique can fully separate objects that are a distance of approximately $c\sigma/2 \approx 6$ cm apart (see Fig. 1). This allows for accurate range gating that effectively can remove obscuring objects such as camouflage or backscattering from aerosols or a water column. Furthermore, an automatic control of the gain in the camera has been introduced such that it can vary between time slices. Therefore certain ranges are suppressed, and others are enhanced. For example, by increasing the gain with range one can suppress the foreground and enhance vague objects in the background. Compensation can be automated for decreasing reflection with range as r^{-2}, or an exponential damping of the light in an absorbing media as in the atmosphere, fog, water, etc.

5. Summary and Outlook

The sequential range gating technique presented above gives fast and high-accuracy range-gated 2-D and 3-D imaging. A prototype was built consisting of a picosecond pulsed green laser triggering an equally fast camera and electronics containing a sensitive MCP. It was shown to produce a 3-D image with range accuracy down to 1 mm in half a million pixels in less than 1 s, which places it at the forefront of current laser radar techniques. There are no moving parts, as there are in, e.g., scanning techniques. Our 2-D and 3-D gating technique is automated, i.e., the system settings are varied automatically.

The disadvantages of our technique are lack of eye safety and that the 3-D gated viewing does not make maximum use of the reflected light. The first problem will be solved in air with a new MCP at eye-safe IR wavelengths.[2] The second may be solved by further developments of avalanche photodiodes.[3] However, by optimizing the range coverage, gate times,

and steps for a given scenario we make nearly optimal use of the reflected light.

The performance characteristics point toward obvious improvements of our technique. Enhancing the quantum efficiency of the MCP toward 100% will improve our sensitivity by almost 1 order of magnitude. A more powerful laser and higher PRF will increase the SNR. Narrower laser pulses and shorter gating times will reduce the variance and thus further increase the range accuracy and resolution.

Our technique can be used for accurate gated viewing through aerosols and camouflage. Backscatter can be effectively removed by varying the gating, the gain, and the background as needed. The enhanced 2-D and 3-D images improve the detection and recognition of objects such as faces and mines. With small adjustments the technique can be applied in bad weather conditions and at short and long range, and to covert 3-D night vision with an IR-pulsed laser, underwater 3-D imaging, unmanned underwater vehicles, and robotic vision.

In the future, we will further process the time slices $I_i(x, y)$ in order to correct for blurring from atmospheric turbulence, underwater scattering, etc. We are currently working on measuring the medium transfer functions for water, aerosols, turbulence, etc., and subsequently incorporating them into inverse Wiener filtering. From the resulting enhanced image sequence we can produce and optimize filtered 2-D and 3-D images.

Appendix A

We here prove Eq. (7), that the total variance σ^2 is equal to the sum of the variances of the camera gate $(\sigma_G)^2$ and laser pulse $(\sigma_P)^2$. As mentioned in Subsection 3.A we assume the time steps are small so that we can replace the sum, $\Sigma_i \rightarrow \int dt_i/\Delta t$, by an integral over time slices. Without loss of generality we can normalize the camera gate and laser pulse to unity, such that $I = \int dt_i \int dt P(t)G(t_i - t) = 1$, where the integrations are unlimited. Also, we can translate $t - 2r/c \rightarrow t$.

The weighted average time is then

$$\langle t_i \rangle = \int dt_i \int dt P(t)G(t_i - t)t_i, \qquad \text{(A1a)}$$

where P is laser pulse power distribution and G is camera gate as function of time.

Next we substitute the new variable $\tau \equiv t_i - t$, into Eq. (A1a) and obtain

$$\langle t_i \rangle = \int d\tau \int dt P(t)G(\tau)(\tau + t) = \langle t \rangle_P + \langle \tau \rangle_G, \qquad \text{(A2a)}$$

where the indexes of the brackets indicates that the average is weighted with laser pulse shape (index P) or the camera gate form (index G), i.e., $\langle t^n \rangle_P = \int t^n P(t)dt$, and $\langle \tau^n \rangle_G = \int \tau^n G(\tau)d\tau$.

In similar fashion, we get the average of the time square

$$\langle t_i^2 \rangle = \int d\tau \int dt P(t)G(\tau)(\tau + t)^2$$
$$= \langle t^2 \rangle_P + \langle \tau^2 \rangle_G + 2\langle t \rangle_P \langle \tau \rangle_G. \qquad \text{(A3a)}$$

Subtracting the square of Eq. (A2a), we obtain the variance

$$\sigma^2 \equiv \langle t_i^2 \rangle - \langle t_i \rangle^2$$
$$= \langle t^2 \rangle_P - \langle t \rangle_P^2 + \langle \tau^2 \rangle_G - \langle \tau \rangle_G^2$$
$$= \sigma_P^2 + \sigma_G^2. \qquad \text{(A4a)}$$

Equation (6) is derived in a similar manner by substitution of $\tau = t - t_i = t - (t_0 + i\Delta t)$, where t_0 is start delay, i is the image number, and Δt is the delay step.

References

1. B. W. Schilling, D. N. Barr, G. C. Templeton, L. J. Mizerka, and C. W. Trussell, "Multiple-return laser radar for three-dimensional imaging through obscurations," Appl. Opt. **41,** 2791–2799 (2002).
2. R. G. Driggers, R. H. Vollmerhausen, N. Devitt, C. Halford, and K. J. Barnard, "Impact of speckle on laser range-gated shortwave infrared imaging system target identification performance," Opt. Eng. **42,** 738–746 (2003).
3. M. A. Albota, R. M. Heinrich, D. G. Kocher, D. G. Fouche, B. E. Player, M. E. O'Brien, B. F. Aull, J. J. Zayhowski, J. Mooney, B. C. Willard, and R. R. Carlson, "Three-dimensional imaging laser radar with a photon-counting avalanche photodiode array and microchip laser," Appl. Opt. **41,** 7671–7678 (2002).
4. G. R. Fournier, D. Bonnier, J. L. Forand, and P. W. Pace, "Range-gated underwater laser imaging system," Opt. Eng. **32,** 2185–2190 (1993).
5. J. W. McLean, "High resolution 3-D underwater imaging," in *Airborne and In-Water Underwater Imaging*, G. D. Gilbert, ed., Proc. SPIE **3761,** 10–19 (1999).
6. R. Stettner and H. Bailey, "Staring underwater laser radar (SULAR) 3-D imaging," in *Laser Radar Technology and Applications VI*, G. W. Kamerman, ed., Proc. SPIE **4377,** 57–64 (2001).
7. C. S. Fox, "Active electro-optical systems," in *IR/EO System Handbook* (SPIE Press, Bellingham, Wash., 1993), Vol. 6.

PROCEEDINGS OF SPIE REPRINT

SPIE—The International Society for Optical Engineering

High-accuracy 3D laser radar

J. Busck, H. Heiselberg

Reprinted from

Laser Radar Technology and Applications IX

From the conference on:

3D Laser Radar

13 April 2004
Orlando, Florida, USA

SPIE P PROCEEDINGS SERIES

Volume 5412

SPIE paper # 5412-33

High accuracy 3-D laser radar

Jens Busck[*ab] and Henning Heiselberg[a]. [a]Danish Defense Research Establishment, Ryvangs Alle 1, DK-2100 Copenhagen, Denmark. [b]Technical University of Denmark, Ørsteds Plads, bldg. 349, DK-2800 Kgs. Lyngby, Denmark.

ABSTRACT

We have developed a mono-static staring 3-D laser radar based on gated viewing with range accuracy below 1 mm at 10 m and 1 cm at 100 m. We use a high sensitivity, fast, intensified CCD camera, and a Nd:YAG passively Q-switched 32.4 kHz pulsed green laser at 532 nm. The CCD has 752×582 pixels. Camera shutter is controlled in steps of 100 ps. Camera delay is controlled in step of 100 ps. Each laser pulse triggers the camera delay and shutter. A 3-D image is constructed from a sequence of 50-100 2-D reflectivity images, where each frame integrates ~700 laser pulses on the CCD. In 50 Hz video mode we record a 2-D sequence in a second and process a 3-D image in few seconds. We compare 3-D images with a system performance model.

Keywords: Laser radar, 3-D imaging, gated viewing.

1. INTRODUCTION

Recently, there have been experimental studies focused on the advantage of the additional range information in the process of identifying objects[1]. A contrast or reflectivity image does not uniquely identify an object. The range information helps discriminating objects. New active electro-optical 3-D imaging sensors with laser illumination have developed within the last ten years, e.g. gated viewing high accuracy 3-D laser radar[2], scanning streak tube imaging lidar (STIL)[3], scanning 1.06 nm infrared 3 kHz laser and avalanche photodiode detector[4], 532 nm pulsed laser, CCD camera and photomultiplier tube[5], scanning pencil beam 532 nm pulsed laser and time-of-flight detector[6], staring underwater laser radar (SULAR)[7], and staring 532 nm pulsed laser and avalanche photodiode array[8]. The widely used wavelength of 532 nm gives optimal underwater transmission, whereas the infrared is preferable in the atmosphere.
The active electro-optical imaging sensor with laser illumination that is presented in this paper is based upon gated viewing with a 32.4 kHz pulsed green laser and a fast high sensitivity charge coupled device (CCD) camera, capable of producing high accuracy 3-D imagery from a sequence of 2-D reflectivity images. System specifications are outlined in section 2, the method of producing 3-D images is described in section 3, 2-D and 3-D images are presented and compared with computer model in section 4 and 5, summery and future work in section 6.

2. SYSTEM SPECIFICATIONS

The laser is a 532 nm diode pumped solid state dual-chip Nanolaser. Pulse width less than 500 ps, pulse energy of 4.3 μJ, pulse repetition frequency (PRF) of 32.4 kHz, average power of 140 mW, and peak power of 8.6 kW. The laser operation is simply connecting power and turning the on-key. From the laser a single trigger line is connected directly to the camera. The camera is an intensified (dual stage) CCD camera. The light entering the camera is transformed to electrons by a photocathode and focused onto the intensifier. The intensifier micro channel plate (MCP) is made up of numerous independently working photomultipliers in the form of narrow hollow glass cylinders, forming a plate. The MCP diameter is 25 mm. The intensified secondary electrons are delivered with high resolution onto a phosphor screen. The intensified image is transferred through a relay lens from the phosphor screen of the MCP intensifier to the CCD. The CCD consists of 752×582 detector elements. The size of the CCD is 6×4.5 mm^2. Camera shutter is controlled externally by the trigger signal from the laser. From time of receiving the trigger signal the camera spends 85 ns before it is ready to gate in light. To compensate for this internal delay in low range applications (<10 m), the laser pulses is fed into an optical fiber. An advantage of the fiber is that the laser will be left at the surface in future underwater experiments, with only the camera and fiber going down. The laser operates at 15-35°C and the camera at 0-50°C. Camera spectral response is 110-800 nm. Minimum camera gate time is 200 ps and the delay (in excess of the internal 85

* E-mail: jb@ddre.dk; phone: +45 39151742; fax: +45 39291533.

Laser Radar Technology and Applications IX, edited by Gary W. Kamerman, Proceedings of SPIE Vol. 5412 (SPIE, Bellingham, WA, 2004) 277-786X/04/$15 · doi: 10.1117/12.545397

ns) is controlled to a minimum of 100 ps. Both camera gate and delay step can be varied in steps of 100 ps. The optics used is 8 cm diameter reflector with focal length 500 mm. The system operates in 50 Hz video mode.

3. METHOD

Every 31 μs the laser emits a pulse. The pulse travels with ~30 cm/ns in air and is reflected at any point of reflection in the path of propagation. While the laser light photons are reflected the camera gate is kept closed to avoid reflections and backscatter from unwanted ranges. At the predefined delay time the camera gate opens the predefined gate time. Typically, the gate is same length as the laser pulse. With a PRF of 32.4 kHz and the camera in 50 Hz video mode, 648 laser pulses are integrated in a single 2-D reflectivity image. The 648 integrated laser pulses improve the signal to noise ratio (SNR) with a factor of 25 compared to a single pulse system. The first 648 laser pulses are gated with a fixed start delay and integrated in the first 2-D image in a sequence. The next image integrates a new set of pulses gated at a new delay 100 ps longer than the previous delay. In one second 50 range intervals are gated and the reflectivity recorded in 50 images, see Fig. 1. To create a 3-D image the 2-D image sequence is processed as described below.
The depth of range is the length of pulse plus the length of gate, times the speed of light. The depth of range illuminated with a 500 ps pulse and a 500 ps gate is 30 cm, if the pulse and gate are assumed rectangular. The gate and the pulse both deviate from rectangular-shape and with jitter in gate, pulse and delay, the depth of range increases. The illumination versus range profile results from convolution of the camera gate and reflected laser pulse

$$Q_i = \int G(t - t_i) P\left(t - \frac{2nr}{c}\right) dt ,$$

where Q_i is radiant energy, G camera gate, P laser pulse flux, t_i camera delay, n refractive index and c speed of light. The range r versus image number i, delay step Δt and start delay t_0 is

$$r = \frac{c}{2n} t_i = \frac{c}{2n}(t_0 + i\Delta t),$$

where n is refractive index. We insert the image number mean value

$$< i >= \frac{\sum_i i \times Q_i}{\sum_i Q_i},$$

where Q_i is the pixel value of radiant energy in the i'th image. The range to a target point in the field of view

$$< r >= \frac{c}{2n}(t_0 + < i > \Delta t).$$

This is the expressions used to create a high accuracy 3-D laser radar image by a sequence of full scene gated viewing 2-D reflectivity images.

3.1 Range accuracy

Noise in the sequence of 2-D reflectivity images induces range noise in the corresponding 3-D image. The range accuracy is dependent on signal to noise ratio SNR. The signal to noise ratio squared is

$$SNR^2 \approx \frac{\sigma \times \max(Q_i)}{\Delta t},$$

where Δt is the delay step, and $\sigma = \sqrt{(\sigma_p^2 + \sigma_g^2)}$, where σ_p^2 is the variance of the laser pulse, and σ_g^2 is the variance of the camera gate.

The range accuracy is

$$\Delta r \approx \frac{c}{2n}\frac{\sigma}{SNR}.$$

For example, if σ = 400 ps, max(Q_i) = 256 (8 bit scale), and Δt = 100 ps, then SNR = 32. Assuming n = 1, we get range accuracy Δr = 1.9 mm. We have experimentally found an optimal range accuracy of less than 1 mm under ideal conditions.

3.2 Range correction

There is a minor range correction to be applied to get the absolute range r_{abs}. The correction is caused by the camera gate time.

The pixel values versus image number are a discrete set of values, each being a convolution of the camera gate and the reflected laser pulse. Figure 2 shows pixel value versus image number for different settings of camera gate time. The curves represent camera gates of 0.3, 0.4,…,1.0 ns. The curves result from identical image sequences settings except the gate time has been changed. The curves represent the reflection from a common point at the target. The saturation curve is from another target point where the reflection saturates the detector element. What can be seen from the curves is that the weighted average image number shifts towards lower image numbers with longer gate time. The maximum of a curve occurs when

$$t_0 + < i > \Delta t + \frac{t_g}{2} = \frac{2nr_{abs}}{c},$$

where t_g is camera gate time.

According to the previous section the average range is calculated by

$$< r >= \frac{c}{2n}(t_0 + < i > \Delta t) = r_{abs} - \frac{ct_g}{4n},$$

where the last equality is by substitution. Thus the average range is corrected by additional 7.5 cm/ns to get the absolute range assuming n=1. For example, with a gate time t_g = 0.5 ns, the range correction is 0.5 ns × 7.5 cm/ns = 3.75 cm.

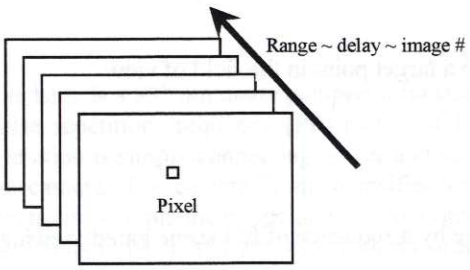

Fig. 1. 2-D reflectivity image sequence.

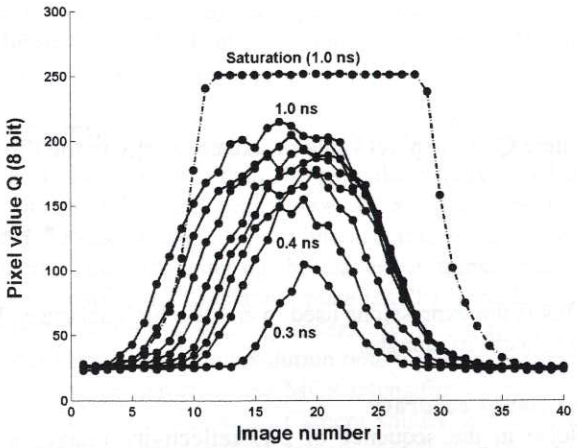

Fig. 2. Experimental pixel values versus image number.

3.3 Background

To make successfully 3-D images it is important that the right background level is subtracted from the sequence of 2-D reflectivity images. The background affects different pixels differently dependent on the signal to noise ratio SNR in the pixels and the actual range to the corresponding target points. The background itself drags the range towards the middle of the 2-D sequence, see Fig. 2. Therefore, points closer than the corresponding range of the middle image is dragged

towards longer range and points further away than the middle image are dragged towards closer range. If the background is fixed for all pixels and the entire image sequence, it can be subtracted in an instant with no 3-D distortion.

3.4 Skewness

In general, the set of pixel values above the background in a single pixel sequence is not symmetric about their weighted mean. Part of the asymmetry is either because the camera gate closes faster than it opens, or the laser pulse rises faster than it drops, or a combination of both. Part of the asymmetry is caused by square root noise (Poisson statistics). This asymmetry or skewness shifts the range. If a pixel is saturated and therefore truncates the set of pixel values at the eight bit maximum value, the pixel is skewness-shifted in range differently than if it is not saturated.

4. GATED VIEWING 3-D LASER RADAR MODEL

Part of the gated viewing and 3-D laser radar project is to develop a system performance computer model. A model has been developed based on ideal step camera gate and rectangular laser pulse, see Fig. 3. The 3-D gated viewing laser radar model combines a suitable laser radar equation, with the convolution of camera gate and laser pulse, and object scattering. The advantage of gated viewing is the elimination of medium backscatter. Though, the backscatter contributes to medium attenuation. Medium forward scatter is modeled by a Gaussian point spread function.

Among the features that can be varied are gate time, gate jitter, delay, delay jitter, delay step, camera sensitivity, laser pulse length, jitter in pulse length, number of pulses, pulse energy, linear gain, reflectivity, field of view, field of illumination with Gaussian laser beam, range, targets, target size, standard deviation of Gaussian medium point spread function, medium refraction coefficient, medium absorption coefficient and medium backscatter coefficient. The surface scattering is assumed diffuse following the Lambert cosine rule for a mono-static source and receiver system.

The computer model outputs a sequence of 2-D reflectivity images. The image sequence of a model run is processed by our 3-D software as an image sequence output from the real laser radar system. Figure 4 shows 3-D images by post-processing of 2-D reflectivity image sequences and compares experiment with computer model. The target in Fig. 4 is a truncated cone 5 cm high, 6 cm top diameter, 12.3 cm bottom diameter and painted in dark and low reflecting army green. The target is a miniature model of a sea mine.

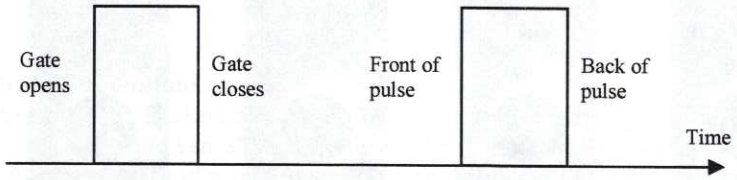

Fig. 3. Time line with rectangular camera gate and laser pulse. Increasing the camera delay in steps results in a discrete convolution of camera gate and laser pulse.

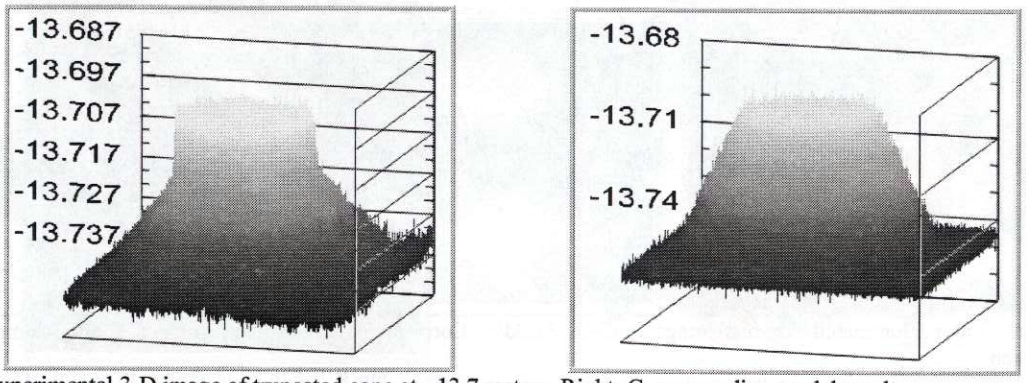

Fig. 4. Left: Experimental 3-D image of truncated cone at ~13.7 meters. Right: Corresponding model result.

5. RESULTS

Trials and experiments were performed in the laboratory at 10-15 meters and in the field at ~100 meters under different conditions such as daylight, night time, fog, snow and sand storm. Results of high and low contrast 3-D imaging is presented in section 5.1, preliminary results for 3-D face recognition application in section 5.2, and bad weather field trial in section 5.3.

5.1 High and low contrast 3-D imaging

Figure 5 shows image numbers 25 to 34 of a 2-D reflectivity sequence of 50 images and delay step of 100 ps. The range is ~13.7 meters. Both targets are miniature models of sea mines 5 cm high, top diameter 6 cm and bottom diameter 12.3 cm. The bottom target is painted dark army green and the upper target is camouflaged by a sandy surface. The background is sandy with dark painted spots and tilted from direction perpendicular to the line of sight. The contrast image of the scene is shown in Fig. 6 (left). The corresponding range image is shown in the middle, and the 3-D image to the right. The 2-D and 3-D range images are gray scale with white being closer range than dark.

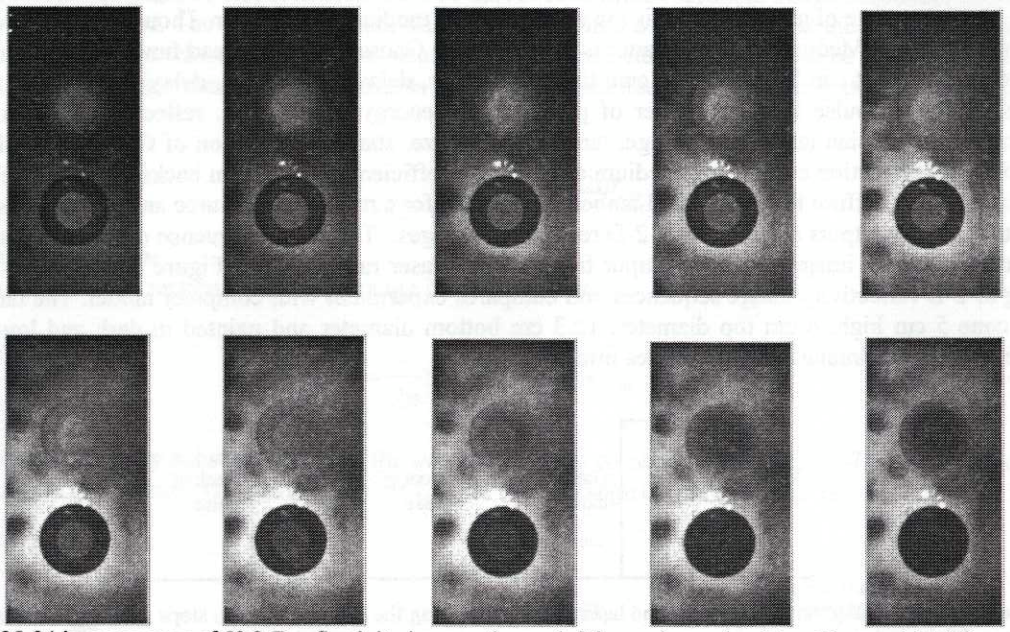

Fig. 5. Images 25-34 in a sequence of 50 2-D reflectivity images, (upper left image is number 25 and lower right 34).

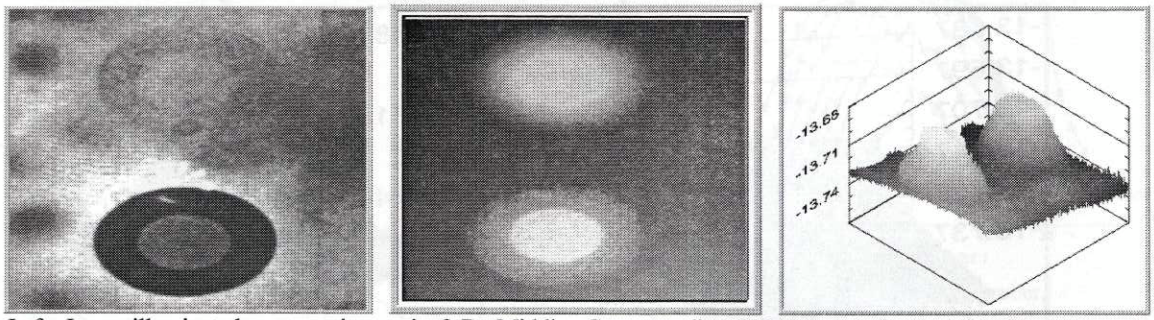

Fig. 6. Left: Laser illuminated contrast image in 2-D. Middle: Corresponding 3-D range image. Right: Computer rotated 3-D representation.

Figures 5 and 6 clearly show the difficulty of detecting a camouflaged target such as the sand colored mine from a 2-D image alone. In comparison, the camouflaged mine stands out almost as clear as the non-camouflaged one in our 3-D pictures. The only difference is that the sand cover smears the edges slightly.

That the non-camouflaged mine has sharp edges implies that the range and the (x,y) pixel resolution is better in our gated viewing system than the smearing caused by the sand cover.

5.2 Face recognition

Our gated viewing 3-D laser radar method can be applied for high accuracy face recognition. Because of wavelength and eye-safety we chose a 25 cm high doll. The range to the doll is 13.5 meters. Figure 7 shows, from left to right, the laser illuminated contrast image of the doll, the 2-D contrast image on top of the 3-D range image, and the color coded range image. The middle and right images are computer rotated by ~60 degrees.

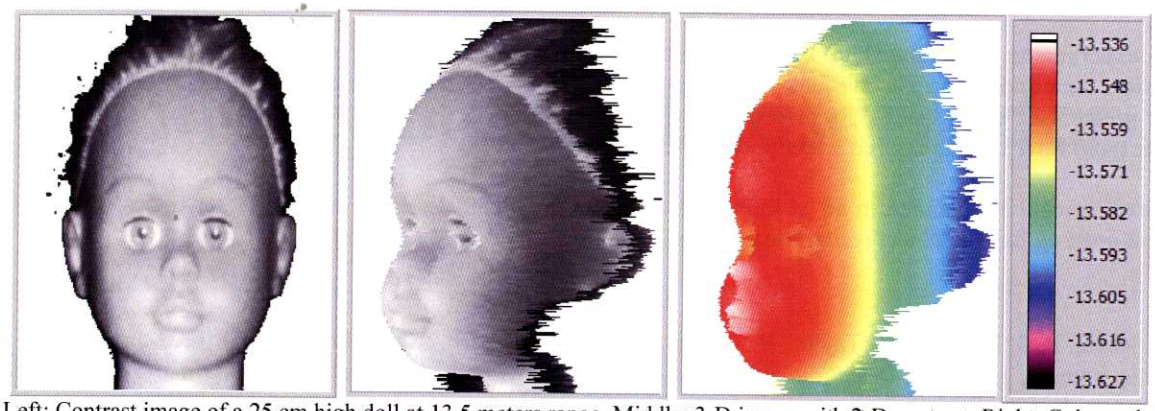

Fig. 7. Left: Contrast image of a 25 cm high doll at 13.5 meters range. Middle: 3-D image with 2-D contrast. Right: Color coded range image with color scale in meters. Settings: camera gate 400 ps and delay step 100 ps. Note: the sticky eyes range-deviation is strongly related to pixel SNR, subtracted background, noise and the timing of the 2-D reflectivity image sequence.

Our prototype system can also produce pictures with sub-millimeter range accuracy at longer distances. At very long distance, the SNR is lower due to reduced reflected intensities, which go as r^{-2}, and the range accuracy decreases correspondingly.

5.3 Long range under bad weather conditions

We did field trials at the south-west coast of Denmark in April 2003. The gated viewing 3-D laser radar was set-up in a van with laser and camera pointing out of the van. Power supply, cables, computers, ect. were fitted into the van, and the 3-D images recorded on side. An image taken of a vehicle at 93 meters range under good weather conditions is shown in Fig. 8. Usually it is possible to see through car windows and record details inside the car, but a layer of ice crystals made it impossible as seen in Fig. 8.

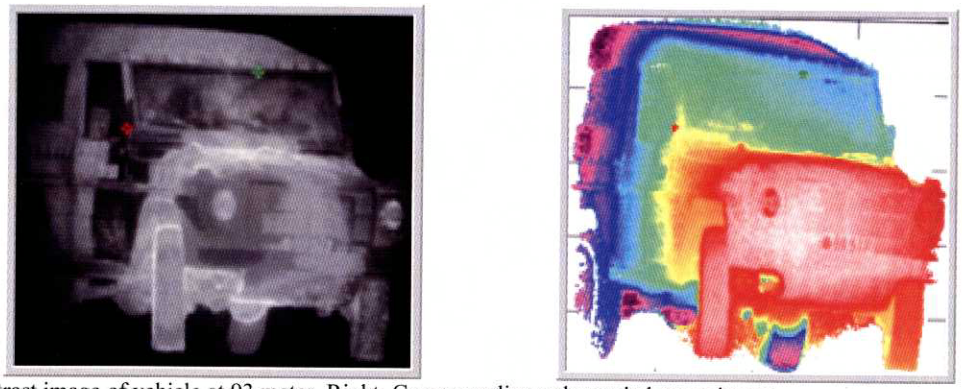

Fig. 8. Left: Contrast image of vehicle at 93 meter. Right: Corresponding color coded range image.

Bad weather conditions as fog and snow generally decrease the viewing range. However, the gated viewing technique does improve images relative to standard 2-D images. Gated viewing allow us to gate at certain distances thereby removing backscattered light from fog, snow, smoke, etc. This was demonstrated in the field trial.

6. SUMMERY AND FUTURE

We have developed a gated viewing 3-D laser radar using a CCD camera and a pulsed laser. The system is compact, easy to use, and delivers fast and high accuracy 3-D images. Our gated viewing 3-D laser radar computer model is a well working tool for planning new experiments under various conditions and system settings. .

The current system has two disadvantages at present. The green laser is neither eye-safe at short distances nor is it covert. The covertness issue can readily be solved by employing a near IR laser and replacing the detector in our prototype. The eye-safety problem could be solved by moving to IR wavelengths, where lasers are common. Unfortunately, no high sensitive IR CCD detectors exist at present that is sufficiently fast for our high accuracy 3-D imaging.

Future experiments are planned to bring the gated viewing 3-D laser radar underwater. We want to investigate absorption, back and forward scatter, and subsequently optimize our gated viewing 3-D imaging. Absorption is minimal for our green laser. Back scatter can be reduced be proper gating. Forward scatter can be reduced by a de-convolution (Wiener type) filter from measured water point spread functions.

Other experiments are planned in air at kilometer distances or longer. For that purpose larger optics will be installed. This will open up for 3-D object recognition and 3-D turbulence studies at long distances.

REFERENCES

1. A. Nevis, R. J. Hilton, S. J. Taylor, B. Cordes, and J. W. McLean, "The advantages of three-dimensional electro-optic imaging sensors", *Detection and Remediation Technologies for Mines and Mine-like Targets VIII*, R. S. Harmon, J. H. Holloway, Proc. of SPIE, 5089, 225-237, 2003.
2. J. Busck and H. Heiselberg, "Gated viewing and high accuracy 3-D laser radar", submitted to Applied Optics, Nov. 2003.
3. J. W. McLean, "High resolution 3-D underwater imaging", *Airborne and In-Water Underwater Imaging*, Proc. of SPIE, 3761, 10-19, 1999.
4. B. W. Schilling, D. N. Barr, G. C. Templeton, L. J. Mizerka, and C. W. Trussel, "Multiple-return laser radar for three-dimensional imaging through obscurations", *Applied Optics*, **41**, 2791-2799, 2002.
5. N. Cadalli, P. J. Shargo, D. C. Munson, and A. C. Singer, "3-D tomographic imaging of ocean mines from real and simulated lidar returns", *Ocean Optics: Remote Sensing and Underwater Imaging*, G. D. Gilbert and R. J. Frouin, Proc. of SPIE, 4488, 155-166, 2002.
6. P. M. Evans, J. O. Klepsvik, and M. L. Bjarnar, "New technology for subsea laser imaging and ranging system for inspection and mapping", *Sensor Review*, **18**, 97-107, 1998.
7. R. Stettner and H. Bailey, "Staring underwater laser radar (SULAR) 3-D imaging", *Laser Radar Technology and Applications VI*, G. W. Kamerman, Proc. of SPIE, 4377, 57-64, 2001.
8. M. A. Albota, R. M. Heinrichs, D. G. Kocher, D. G. Fouche, B. E. Player, M. E. O'Brien, B. F. Aull, J. J. Zayhowski, J. Mooney, B. C. Willard, and R. R. Carlson, "Three-dimensional imaging laser radar with a photon-counting avalanche photodiode array and microchip laser", *Applied Optics*, **41**, 7671-7678, 2002.

Simulation of gated viewing mono-static three-dimensional laser radar

Jens Busck, Danish Defense Research Establishment, Ryvangs Alle 1, DK-2100, Copenhagen, Denmark, and Technical University of Denmark, Ørsteds Plads, building 349, DK-2800, Lyngby, Denmark. E-mail jb@ddre.dk, phone +45 39151742, fax +45 31291533.

Abstract

Simulation of a gated viewing mono-static pulsed three-dimensional laser radar system is presented. The simulated images are compared with experimental telescopic image records at 207 m range in air and through 4 m of clear tap-water. The laser pulses and camera gate are assumed rectangular in time, which gives a piece-wise linear range gate of the reflected radiant laser pulse energy. The range gate is combined with a Gaussian laser beam, a medium point spread function, and a laser radar equation that governs the medium attenuation, surface scattering, and camera characteristics, to give the detected image signal.

Subject terms: pulsed laser radar; gated viewing; range gating; image simulation.

1 Introduction

Gated viewing laser radar systems with a pulsed laser and a fast intensified CCD camera are being developed and tested throughout the world.[1-5] The laser radar systems have been tested on long range (10 km) performance with telescopic camera optics for two- and three-dimensional imaging capabilities.[1] High accuracy short range (10 m) two- and three-dimensional performance has been proved.[2-3] An underwater system has been developed for enhanced video imaging applications.[4] Underwater performance has been tested with bar tagets.[5]

The presented computer model simulates the laser radar system and the surrounding environment and outputs a sequence of range gated digital images. The output image sequence can be viewed directly or loaded into a laser radar image sequence analysis program for three-dimensional imaging. The simulated laser radar system specifications and the method of three-dimensional image processing are described elsewhere.[2-3]
The laser beam, the camera, and the target are described in Sec. 2-4, the medium scattering and absorption in Sec. 5, and gated viewing in Sec. 6. Sections 2-6 are leading to the laser radar equation in Sec. 7. Experiment and simulation results are compared in Sec. 8-9, followed by the discussion and conclusion in Sec. 10-11.

2 Laser

The simulated laser pulses are rectangular in time, i.e. they are rectangular along the axis of propagation. Jitter in the pulse time is simulated as small Gaussian-distributed variations. The laser beam is single mode TEM_{00} and rotationally symmetric around the axis of propagation. The laser beam wave front is approximated by a spherical wave.[6]
The deviation of the laser beam in the digital output images of the laser radar simulation depends on the ratio of the laser's field of illumination FOI to the camera's field of view FOV. The deviation of the Gaussian laser beam

$$s = \frac{FOI}{FOV}, \tag{1}$$

where it should be noted that s is not dependent on range.
The transversal profile of the pulsed laser beam is Gaussian

$$g(r_{xy}) = K \times \exp\left(-\frac{1}{2}\left(\frac{FOV}{FOI} r_{xy} \right)^2 \right), \tag{2}$$

where $r_{xy} = x^2 + y^2$, and K is a normalization constant.
The laser beam is normalized to conserve energy. The normalization constant has to be determined for each new setting of the Gauss-beam deviation s .

3 Camera

The simulated camera gate is rectangular in time, i.e. the process of opening or closing the camera gate is momentary. Gaussian distributed jitter applied to the gate time is optional. The gated viewing camera delay is initiated when the center of the laser pulse leaves the laser. Jitter can be applied to the camera delay. The camera gain is linear without offset. The gain can be stepped up or down through an image sequence.

4 Target

The target and the surface are digitized by the field of view of each detector element of the camera's CCD. The target and surface are digitized by the projection of the two-dimensional detector element array onto the target and surface scene. The projection is defined by the camera optics. The target and the surface are defined as a matrix with the number of entries equal to the number of detector elements of the simulated CCD camera. The entries in the target matrix are the height values of the target. The image resolution is the camera field of view divided by the number of detector elements.

5 Environment – scattering and absorption

Diffuse surface scattering for a mono-static laser radar system is given by Lambert's cosine law

$$k \int_0^{2p} dj \int_0^{p/2} \cos^2(q)\sin(q)dq = 1, \tag{3}$$

where a laser radar system is mono-static when the light source (laser) and the receiver (camera) are co-located, k = 3/2p is the energy conserving normalization constant, f is the surface normal azimuth angle, and ? is the angle between the incident light and the surface normal.
The light reflected at the target propagates towards the laser radar system as a spherical wave and attenuated by the inverse square of the range $1/(2pr^2)$ from the reflecting point to the laser radar. The loss of light due to backscattering of the medium of propagation is described by the backscattering coefficient b_b. Backscattered light is scattered at angles from 90 to 180 degrees from the direction of propagation. The bulk of the light is forward scattered in small angles. It is assumed that the forward scattered light can be described by a Gaussian point spread function (psf). A Gaussian point spread function has been modeled before.[7] The point spread scattering causes a blurring of the un-scattered image signal. The absorption of light of the medium of propagation is described by the absorption coefficient a. The medium attenuation due to back-scattering and absorption is exponential with range. The surface absorption is implicitly described by a surface reflectivity coefficient R. Due to energy conservation the sum of the surface reflectivity coefficient and the surface absorption coefficient is one.

6 Gated viewing

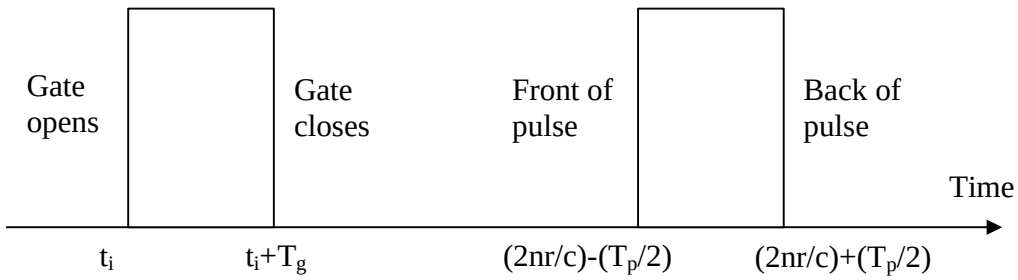

Fig. 1 Time line at the laser radar system with camera gate and reflected laser pulse. The laser pulse two-way travel time is 2nr/c from the laser to the reflecting point at the range r and back to the camera. Camera delay is t_i, gate time is T_g, laser pulse time is T_p, refractive index is n, and c is the speed of light.

Consider the laser pulse and the camera gate on a time line (Fig. 1). The laser pulse is reflected at a range r from the laser radar. The camera delay t_i is triggered by the emission of the laser pulse, i.e. the camera delay is onset by the time the center of the laser pulse is emitted from the laser. The sub-script i number discrete delay steps of the recorded images in a sequence.[2] At the delay time t_i the camera opens for exposure T_g the camera gate time. If c is the speed of light and n is the refractive index, it takes time 2nr/c for the center of the laser pulse to reach the reflecting target point at the range r and return to the camera. If T_p is the pulse time, then the front of the laser pulse reaches the camera at time (2nr/c) – (T_p/2) after laser pulse emission and delay triggering. In order to range gate the point at the range r the camera delay t_i is adjusted

$$\frac{2nr}{c} - \frac{T_p}{2} - T_g < t_i < \frac{2nr}{c} + \frac{T_p}{2}. \tag{4}$$

The length of the range gate depends on T_g and T_p. The amount of light received from the individual reflection points within the range gate depends on whether the camera gate time is longer, shorter, or equal to the laser pulse time (Sec. 6.1 below).

The range gated radiant energy Q_i in the i'th image is a convolution of the laser pulse radiant flux F (units: Js^{-1}) and the camera gate

$$Q_i(r) = \int_{-\infty}^{\infty} \Phi\left(t - \frac{2nr}{c}\right) G(t - t_i)\, dt, \tag{5}$$

where G is the camera gate, and $r = (x^2 + y^2 + z^2)^{1/2}$, where x and y are defined in the object plane.
The range gated radiant energy Q_i is computed for each pixel's field of view and the radiant flux thus varies dependent on the reflectivity of the points in the range gated volume.
In general the expression Eq. (5) applies to all F 's and G's.

6.1 *Gated viewing with rectangular laser pulse and camera gate*

This section describes the maximum reflected laser pulse radiant energy that can be received from the reflection points within the range gate and applied in the laser radar equation (Sec. 7 below).
Consider the flux F of the reflected rectangular laser pulse at the laser radar system

$$\Phi(t - \frac{2n}{c} r) = \begin{cases} \Phi_p & for \quad -\frac{T_p}{2} \le t - \frac{2n}{c} r \le \frac{T_p}{2} \\ 0 & otherwise \end{cases}, \tag{6}$$

where r and t are greater than zero, T_p is the laser pulse time, $F_p = Q_p/T_p$, and Q_p is the total laser pulse energy.
Define the rectangular camera gate

$$G(t - t_i) = \begin{cases} 1 & for \quad 0 \le t - t_i \le T_g \\ 0 & otherwise \end{cases}, \tag{7}$$

where T_g is camera gate time and t_i is camera delay initiated at (r,t) = (0,0), when the center of the laser pulse leaves the laser.

By substitution of the rectangular laser pulse and camera gate into Eq. (5)

$$Q_i(r) = \int_{t_i}^{t_i+T_g} \Phi\left(t - \frac{2n}{c} r\right) dt \,. \tag{8}$$

Define the range $r_i = ct_i/2n$, then

$$Q(r'+r_i) = \int_{0}^{T_g} \Phi\left(t - \frac{2n}{c} r'\right) dt \,, \tag{9}$$

where r' = r - r_i is the range between the reflection point at the range r and the delay point at the range r_i, and $Q(r'+r_i) = Q_i(r)$.
The radiant laser pulse energy Q received from a reflected laser pulse is the laser pulse radiant flux F integrated over the camera gate time.
The three expressions Eq. (6), (7), and (9) lead to the range gated maximum radiant energy Q (App. A) used in the laser radar image simulation. A graphical representation of the range gate of appendix A is given in Fig. 2. The length of the range gate is $(c/2n)(T_g+T_p)$. Given a camera delay range $r_i = (c/2n)t_i$, a laser pulse time T_p, and a camera gate time T_g, the closest gated point from the laser radar system is $r = r'+ r_i = (c/2n)(t_i - T_p/2)$, independent on camera gate time. The farthest gated point is $r = r'+ r_i = (c/2n)(t_i + T_g + T_p/2)$, dependent on both the pulse time and the camera gate time. When camera gate T_g is equal to the laser pulse time T_p, the two range gated profiles merge into a single profile (Fig. 2).

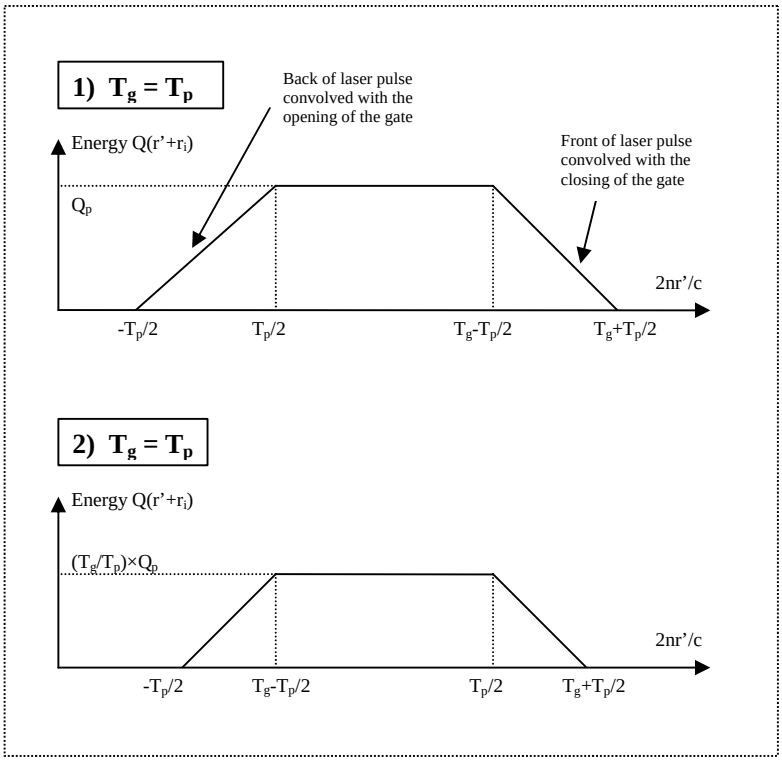

Fig. 2 Maximum reflected radiant energy Q of a range gated rectangular laser pulse, given camera delay t_i, rectangular camera gate time T_g, and laser pulse time T_p. Q_p is the total laser pulse energy. The range from the laser radar to the reflection point is r, the range corresponding to the camera delay is $r_i = ct_i/2n$, and r' is the range from the reflection point r to the delay point r_i, (i.e. $r = r' + r_i$). Note: If $T_g = T_p$ the two profiles merge into a single profile.

7 Laser radar equation

The maximum reflected radiant laser pulse energy Q for the range gate of the rectangular laser pulse and camera gate is incorporated into the laser radar equation of the system and the environment. The laser radar equation for the amplified radiant energy incident on the detector

$$Q_{GV} = psf * \left\{ Q \times g \times \exp(-2rc) \times \left(\frac{3\cos^2(q)}{2p} \right) \times \frac{F \times T \times A \times N \times R \times QE}{2pr^2} \right\}, \qquad (10)$$

where

*	convolution in x and y,
Q_{GV}	amplified radiant energy incident on a detector element,
Q	the maximum reflected radiant laser pulse energy,
psf	point spread function,
r	(= r'+ r_i), range from laser radar system to reflecting point,
g	Gaussian beam,
a	absorption coefficient,
b_b	backscattering coefficient,
?	angle between incident beam and the local surface normal,
F	gain value,
T	transmission of camera optics,
A	camera optic aperture,
N	number of laser pulses per image,
R	coefficient of reflectivity, and
QE	quantum efficiency of intensified camera.

The expression Eq. (10) is calculated for each detector element and divided by an overall system resolution unit to get the image pixel bit-values, simplifying the analog-to-digital simulation. For example the resolution unit could be the energy of 10 photons of 532 nm. Additive Gaussian noise with a standard deviation equal to the square-root of the noiseless pixel value is optional.

8 Three-dimensional laser radar simulation compared with real system measurements

A three-dimensional laser radar recording event was performed in August 2004. Figure 3 shows the laser radar system setup with the 14 inch telescope. The focal length is 4 m.

Fig. 3 Laser radar set-up with the 14 inch telescope.

One of the goals was to record an image sequence of a target that could be simulated by the three-dimensional laser radar computer model. For this purpose the target in Fig. 4 was chosen. The shape of the target is that of a truncated cone, height 5 cm, bottom diameter 12.6 cm, and top diameter 6 cm. The reflectivity of the target is 12 % at the wavelength of 532 nm.

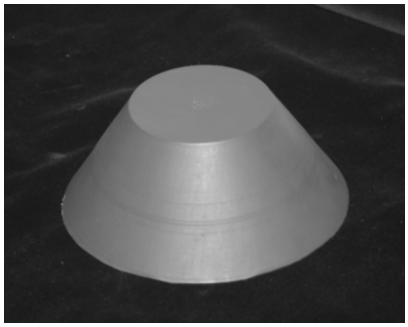

Fig. 4 Digital image of miniature sea mine with 12 % reflectivity at 532 nm, height is 5 cm, bottom diameter is 12.6 cm, and top diameter is 6 cm.

The target was placed on the ground at a range of 207 m. The laser beam was focused on the target in the white box (Fig. 5). The camera gate was set to 1 ns and delay step was set to 0.1 ns. The analysis program setting of camera internal delay offset is adjusted to 86.5 ns to fit the simulated range with the range of the experimental recording. The internal delay offset is an inherent property of the camera that varies over time.

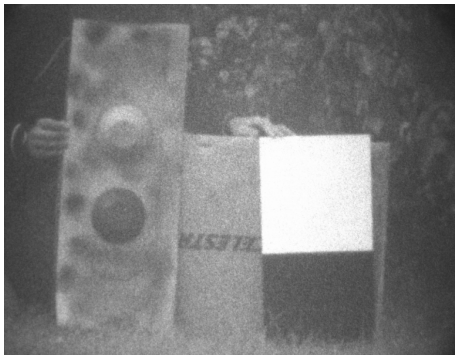

Fig. 5 Contrast image of two truncated cone targets and a contrast (black/white) target at about 207 meters range. The target in the white box is shown in Fig. 4.

Part of the recorded image sequence and part of the simulated image sequence are shown in Figs. 6-7. In Figs. 8-9, the corresponding three-dimensional images are shown. The overall shape and size of the target is well preserved in both experiment and simulation.

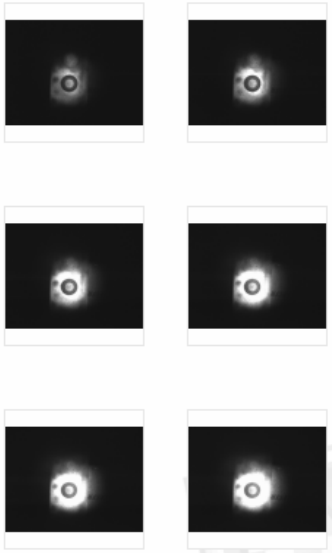

Fig. 6 Target images 18-23 of a sequence of 50 range gated contrast images, the sequence is taken at about 207 meters with the telescope. The camera delay step is 0.1 ns and the gate is 1 ns. The ambient light is range gated out. Only the laser illuminated range gated target is seen.

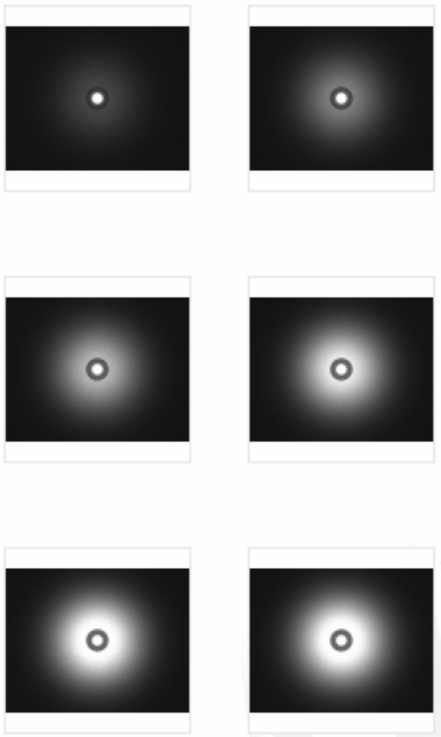

Fig. 7 Simulated target images 9-13 of a sequence of 30 range gated contrast images. The camera delay step is 0.1 ns and the gate is 1 ns.

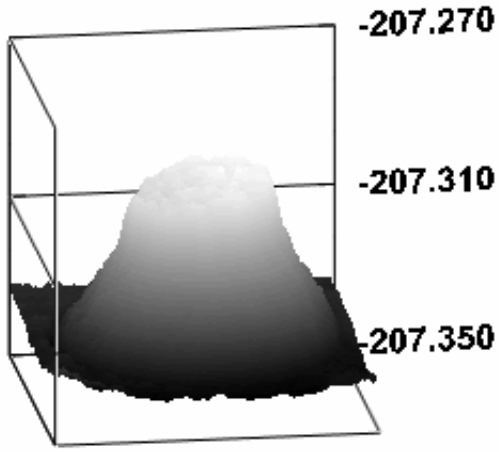

Fig. 8 Three-dimensional representation of the target in Fig. 4 by processing of the corresponding experimental image sequence in Fig. 6. Laser radar system settings, 0.5 ns camera gate time, 0.1 ns camera delay step, and 4 m focal length of telescope. The range scale is in meters.

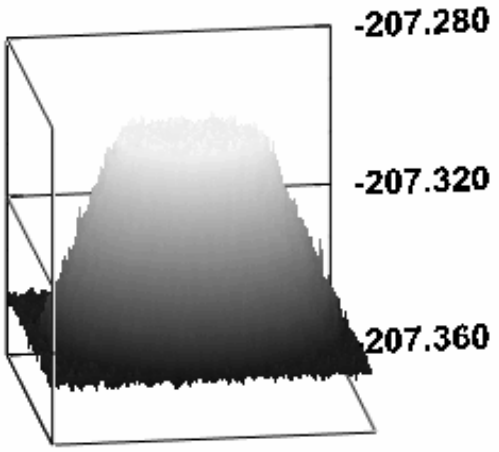

Fig. 9 Three-dimensional representation of the target in Fig. 4 by processing of the corresponding laser radar computer simulated image sequence in Fig. 7. Simulated laser radar system settings, 0.5 ns camera gate time, and 0.1 ns camera delay step. The range scale is in meters.

9 Three-dimensional underwater imaging and simulation

This section presents preliminary three-dimensional underwater imaging and simulation. A three-dimensional laser radar underwater imaging experiment was set-up in November 2004. The full underwater experimental analysis, results and conclusion is beyond the scope of this paper and will be reported in another paper.

One of the aims of the underwater simulation and experiment is to find out what effect the water point spread function will have on the three-dimensional image of the target.

For the underwater three-dimensional imaging a 10 m long and 0.4 m diameter tube is filled with clear tap-water. One end of the tube is fitted with a glass window. The distance from the target to the window is about 4 m. The diameter of the camera optics is 5 cm and the focal length is 85 mm. To balance the camera's internal delay the laser pulses are focused into a single mode optical fiber. The fiber is utilized as an optical delay necessary for the short range application. The length of the fiber is 25 m. The average output power of the fiber is about 30 mW, about 1/5 of the average laser output. The power reduction is due to a major reduction by coupling the laser pulses into the fiber, and a minor reduction caused by attenuation

in the fiber. The pulse time broadening in the fiber is negligible for the three-dimensional imaging and is verified experimentally. The underwater images are recorded with a camera gate of 0.5 ns and delay steps of 0.1 ns. The target is described in section (8). The experimental three-dimensional representation of the target is shown in Fig. 10. The corresponding simulation result is shown in Fig. 11. The simulation of clear tap-water was done with realistic absorption and backscattering coefficients for fresh water.[8] The results of both experiment and simulation show that the target edges are rounded by the point spread effect of the water. The 5 cm target height is well preserved.

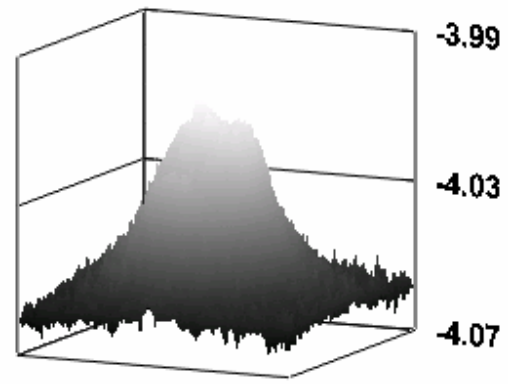

Fig. 10 Experimental underwater three-dimensional miniature sea mine. Laser radar system settings, 0.5 ns camera gate time, 0.1 ns camera delay step, and 85 mm focal length camera optics. The range scale is in meters.

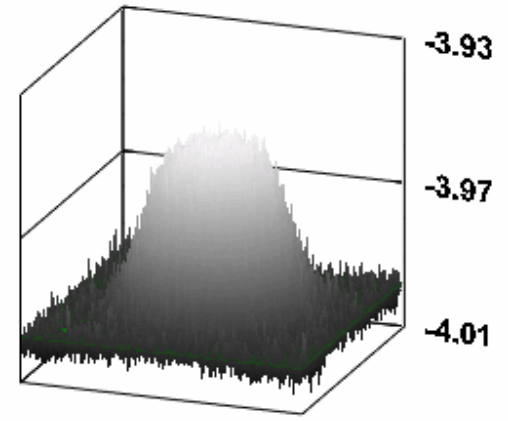

Fig. 11 Simulation of underwater three-dimensional miniature sea mine. Simulated laser radar system settings, 0.5 ns camera gate time, and 0.1 ns camera delay step. The range scale is in meters.

10 Discussion

The laser radar set-up with the telescope is for long range applications and successful three-dimensional imaging over 1 km has been achieved with the system. The smaller and handier 85 mm focal length optics is for short range underwater imaging. The atmospheric attenuation is low compared with absorption and scattering in water. The presented atmospheric three-dimensional image is recorded at a range of 207 m. In water the image is taken at 4 m. The target shape and edges are reasonably well preserved in both cases.
There is a trade-off between the detected signal and the image resolution. The target signal is shared by the number of detector elements that covers the target. In low signal conditions a camera optic with shorter focal length can be chosen on behalf of image resolution to increase the target signal in a fewer number of image pixels. In general the optimal choice of optics may depend on the application, the environment, and available target signal.

11 Conclusion

Imaging by gated viewing has been simulated with success under a set of simplifying assumptions about the environment and the laser radar system. The presented simulations are based on a laser radar equation incorporating environmental scattering, attenuation and the maximum reflected radiant laser pulse energy of the range gate. The simulated images have been compared to the experimental laser radar system images in two- as well as three-dimensional representations. The preliminary results of the underwater gated viewing laser radar imaging verify that three-dimensional images can be produced through 4 m of clear tap water. The experiment and simulation of three-dimensional imaging in water shows that the edges of the target are rounded by the water point spread effect. Ideally, the simulated point spread function would be based on measurements of the scattering characteristics of the medium. In future the three-dimensional target shape transfer function can be defined and explored by experiment and simulation.

The gated viewing laser radar simulation computer model can be expanded and improved on analog-to-digital conversion, gain function, and for example by incorporation of atmospheric turbulence.

12 Appendix A: Maximum range gated radiant energy (Q)

Eq. A1

$$Q(r'+r_i) = \frac{Q_p}{T_p}\left(\frac{2n}{c}r'+\frac{T_p}{2}\right),$$

for $-\frac{T_p}{2} \le \frac{2n}{c}r' < \frac{T_p}{2}$ if $T_g \ge T_p$,

for $-\frac{T_p}{2} \le \frac{2n}{c}r' < -\frac{T_p}{2}+T_g$ if $T_g < T_p$.

Eq. A2

$$Q(r'+r_i) = Q_p,$$

for $\frac{T_p}{2} \le \frac{2n}{c}r' < -\frac{T_p}{2}+T_g$ if $T_g \ge T_p$,

or

$$Q(r'+r_i) = Q_p\left(\frac{T_g}{T_p}\right),$$

for $-\frac{T_p}{2}+T_g \le \frac{2n}{c}r' < \frac{T_p}{2}$ if $T_g < T_p$.

Eq. A3

$$Q(r'+r_i) = -\frac{Q_p}{T_p}\left(\frac{2n}{c}r' - \frac{T_p}{2} - T_g\right),$$

$$\text{for} \quad -\frac{T_p}{2} + T_g \le \frac{2n}{c}r' \le \frac{T_p}{2} + T_g \quad \text{if} \quad T_g \ge T_p,$$

$$\text{for} \quad \frac{T_p}{2} \le \frac{2n}{c}r' \le \frac{T_p}{2} + T_g \quad \text{if} \quad T_g < T_p.$$

Otherwise $Q(r'+r_i) = 0$.

When the camera gate T_g is equal to the pulse time T_p, then Eq. (A2) vanishes and Eq. (A1) and (A3) simplify.
The range from the laser radar to the reflection point is r, the range corresponding to the camera delay is $r_i = ct_i/2n$, and r' is the range from the reflection point r to the delay point r_i, i.e. $r = r' + r_i$.

References

1. L. Klasen, P. Andersson, H. Larsson, T. Chevalier, and O. Steinvall, "Aided target recognition from 3-D laser radar data", *Proc. SPIE*, **5412**, 321-332 (2004).
2. J. Busck and H. Heiselberg, "Gated viewing and high-accuracy three-dimensional laser radar," *Appl. Opt.* **43**, 4705-4710 (2004).
3. J. Busck and H. Heiselberg, "High-accuracy three-dimensional laser radar," *Proc. SPIE*, **5412**, 257-263 (2004).
4. G. R. Fournier, D. Bonnier, J. L. Forand, and P. W. Pace, "Range-gated underwater laser imaging system", *Opt. Eng.*, **32**, 2185-2190 (1993).
5. D. M. He, and G. G. L. Seet, "Underwater lidar imaging in highly turbid waters", *Proc. SPIE*, **4488**, 71-81 (2002).
6. B. E. A. Saleh, and M. C. Teich, "Fundamentals of photonics," *Wiley Inter-science Publication*, New York (1991).
7. G. R. Fournier, and M. Jonasz, "Computer based underwater imaging analysis", *Proc. SPIE*, **3761**, 62-70 (1999).
8. H. G. Gierloff-Emden, N. K. Højerslev, G. Krause, H. Peters, G. Siedler, G. Weichart, and P. Wille, "Oceanography", *Springer-Verlag*, vol. 3, Germany (1986).

Long distance high accuracy 3-D laser radar and person identification

J.F. Andersen [a], J. Busck [ab] and H. Heiselberg [*a].
[a]Danish Defense Research Establishment, Ryvangs Alle 1, DK-2100 Copenhagen, Denmark.
[b]Technical University of Denmark, Ørsteds Plads, bldg. 349, DK-2800 Kgs. Lyngby, Denmark.

ABSTRACT

Results from our fast and high accuracy 3-D laser radar are given at distances up to 500m. The system is based on gated viewing with range accuracy below 1 mm under optimal circumstances. It consists of a high sensitivity, fast, intensified CCD camera, and an Nd:YAG passively Q-switched 32.4 kHz pulsed green laser at 532 nm. The CCD has 752×582 pixels. Camera shutter and delay steps are controlled in steps of 100 ps. Each laser pulse triggers the camera delay and shutter. A 3-D image is constructed from a sequence of 50-100 2-D reflectivity images, where each frame integrates ~700 laser pulses on the CCD. In 50 Hz video mode we record a 2-D sequence in a second and process a 3-D image in a few seconds. We compare 3-D images at short to long distances and quantify the degree of person identification in 3-D. Turbulence, vibrations and system errors are found to limit a successful PID to distances shorter than ~500m for our prototype system.

Keywords: Laser radar, 3-D imaging, gated viewing, person identification, face recognition.
SPIE Code: 5791-2.

1. INTRODUCTION

Range information is useful for identifying objects in addition to ordinary reflectivity images. 3-D laser radar imaging has been greatly improved in the last decade by technologies based on gated viewing laser radars [1,2,3], scanning streak tube imaging laser radars [4,5,6], avalanche photodiode detector [7] and array [8], time-of-flight phase detectors [9], self-mixing detectors [10], single pulse flash laser radars [11], etc. The techniques vary in range accuracy, resolution, recording time, spectral coverage, etc., with a clear trend towards faster and better accuracy and resolution. Typical accuracies of laser range finders are a few centimeters at distances up to 100m [12].

The purpose of this work is to demonstrate a millimeter accuracy in 3-D of our laser radar system at longer distances. Specifically, we shall show results on 3-D imaging on small targets as human faces at distances up to 500m. By comparison between images we quantify the degree of 3-D face recognition and person identification (PID). The advantages of fast high accuracy 3-D active imaging and quantitative PID by comparisons to a 3-D mug shot archive as well as applications to defense against terrorism will be discussed at the end.

2. LASER RADAR PROTOTYPE AND 3-D METHOD

Our laser radar prototype system has been described in detail in Refs. [2,3]. It consists of a picosecond pulsed green laser triggering a fast intensified camera. The laser is a 532 nm diode pumped solid state dual-chip Nanolaser. Pulse width is less than 500 ps, pulse energy of 4.3 μJ, pulse repetition frequency (PRF) of 32.4 kHz, average power of 140 mW, and peak power of 8.6 kW. Beam divergence is 1.5 mrad. From the laser a single trigger line is connected directly to the

[*] E-mail: hh@ddre.dk; phone: +45 39151732; fax: +45 39291533.

CCD camera so that the timing of each individual pulse is known to picosecond accuracy. The camera contains an intensified micro channel plate (MCP) of diameter 25 mm. The CCD consists of 752×582 detector elements. The size of the CCD is 6×4.5 mm^2. Camera shutter is controlled externally by a trigger signal from the laser for each individual pulse. The spectral response of the detector is 110-800 nm. Minimum camera gate time is t_{gate} =200 ps. Both camera gate and delay step t_{delay} can be varied in steps in excess of Δt=100 ps. For high accuracy imaging at long distances we use for optics a 14 inch Celestron telescope with focal length of 4 m. Daylight is much reduced by the small field of view and short gating time, and is further reduced by inserting a narrow filter with a bandwidth of 530-540 nm.

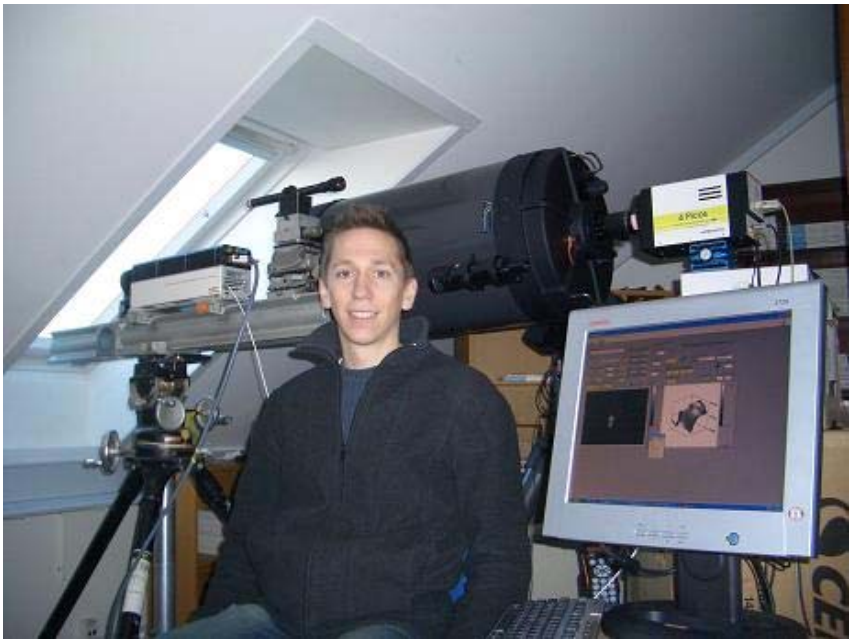

Fig. 1. In front the first author and screen displaying the 3-D software. Behind the picosecond laser (left), 14" telescope (middle) and camera (right) are seen.

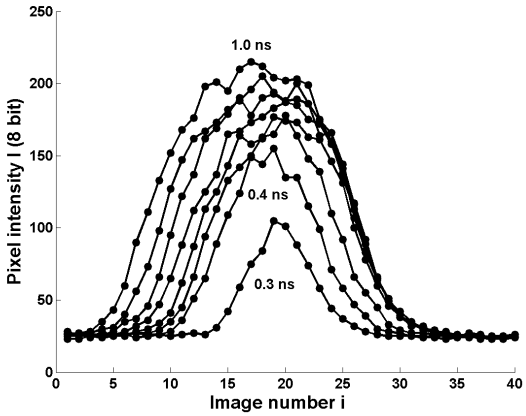

Fig. 2. Experimental values I_i in one pixel versus image number for delay step Δt=100ps and various gate times t_{gate} =300, 400, … 1000 ps.

The total intensity in each pixel is the sum over frames

$$I(x,y)=\sum_{i=1}^{n} I_i(x,y), \tag{1}$$

where I_i is the pixel value of intensity in the i'th frame, see Fig. 2. The number n of images is typically 50 - 100, so that a range of a few meters is covered around the target. The distance z to a target point in any pixel is

$$z(x,y)=\frac{c}{2}\left[t_{delay} + \Delta t \frac{\sum_{i=1}^{n} i \times I_i(x,y)}{I(x,y)} \right], \tag{2}$$

where Δt is the delay step and t_{delay} is the initial delay time. Both are preset in the laser-camera triggering. The pixel coordinates (x,y) are related to the 752×582 pixel numbers by multiplying by the focal length and range and dividing by detector size. We refer to Refs. [2,3] for further details on background subtraction, threshold settings, saturation effects, etc.

The accuracy and resolution in distance Δz is an important quantity for 3-D imaging. As described in detail in Ref. [2] the uncertainty in distance is proportional to the timing accuracy (σ) and inversely proportional to the signal-to-noise ratio (SNR) in the following way

$$\Delta z \approx \frac{c}{2}\frac{\sigma}{SNR}. \tag{3}$$

Here, c = 30 cm/ns is the speed of light, and σ^2 is the sum of the variance of the laser pulse time plus the variance of the camera gate time (each are around $(200\ \text{ps})^2$ for our system [2]). The SNR is typically 10-100 for our 8-bit camera but can be lower at poor light conditions at long distances, where we apply maximal gain in the camera. It is important to realize that the accuracy of our system is not just $\sim c\sigma$ but much smaller, because we sum over a large number of frames I_i each containing a large number of laser pulses (~700) resulting in a large SNR. The resulting range accuracy in each pixel is around $\Delta z \sim 1$ mm under optimal conditions.

The advantage of our system is that the timing accuracy inherent in σ is a system parameter depending only on the laser pulse width and the camera gate time. It is therefore independent of the range[†] to first approximation, and does not get worse at long ranges as do, e.g., triangulation methods. The SNR does generally decrease with increasing range for our system but we can compensate for that by using larger optics (smaller field-of-view), decreasing the field of illuminations and increasing the camera gain. Therefore, the system accuracy Δz remains small even at longer distances. The real limitations to our technique are found to be turbulence, vibrations of telescope and target, drift in laser-to-camera triggering, etc. The resulting total distance accuracy for our system therefore increases gradually to $\Delta z_{system} \sim 5$ mm at a range of 500 m as shown in Fig. 5.

[†] By "range" we mean the average distance z over the pixel's in the image.

3. 3-D IMAGING RESULTS AT LONG DISTANCES

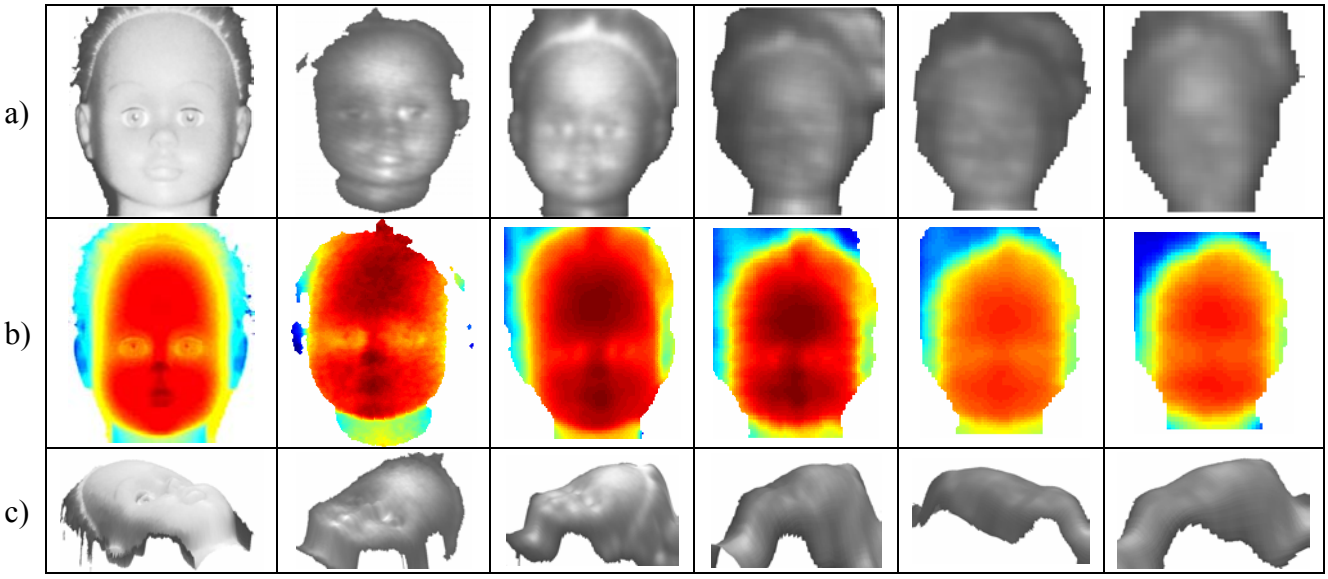

Fig. 3. a) Front view of the target images I(x,y) recorded at distances: 6m, 100m, 200m, 275m, 370m and 485m. b) range images z(x,y) where colors represent distance. c) range images z(x,y) rotated in various directions.

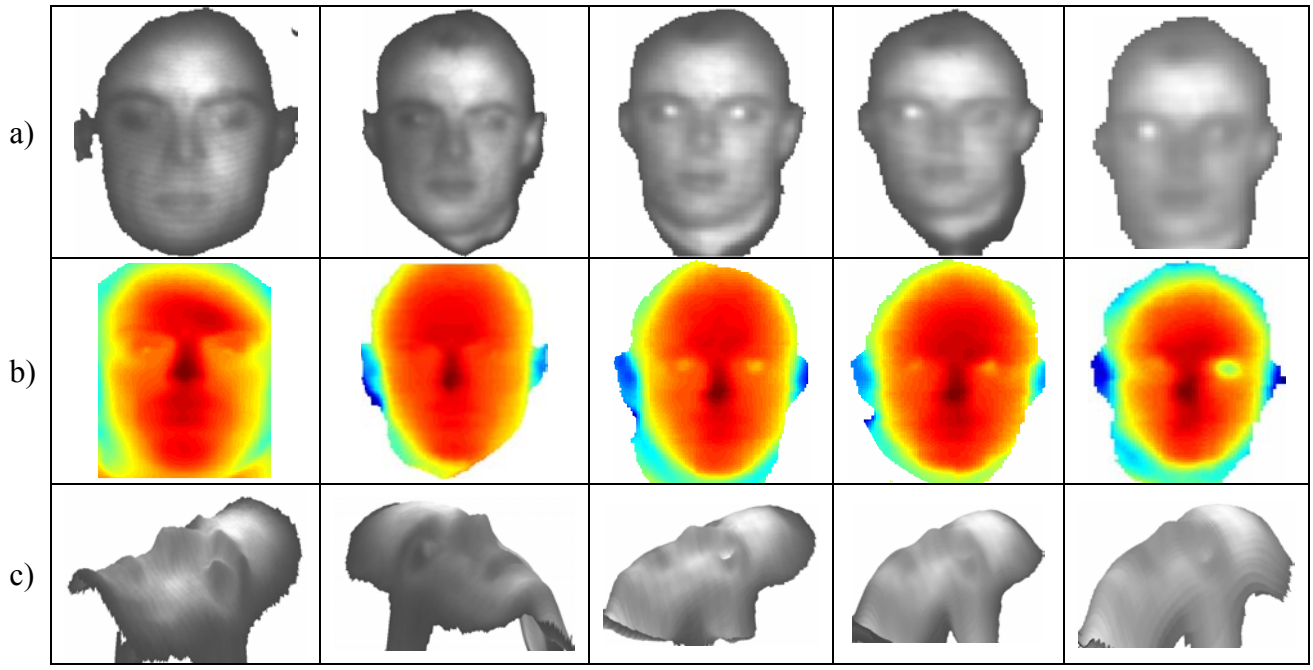

Fig. 4. a) Front view of the target images I(x,y) recorded at distances: 135m, 200m, 275m, 370m and 485m. b) range images z(x,y) where colors represent distance. c) range images z(x,y) rotated in various directions.

In Figs. 3 and 4 images of two persons are shown at various ranges. The top rows are 2-D intensity images I, the second rows are the range z(x,y) images, and in the third rows we have computer-rotated the images in various directions. Both 2-D and 3-D images become worse at longer distances. By asking third parties, whether they recognize the persons or not, we find that PID is unsuccessful from 2-D images alone already at a few hundred meters. In contrast we shall below claim that the 3-D information can discriminate persons by calculating a distance measure.

4. PERSON IDENTIFICATION

As described above we have recorded high-accuracy 3-D images at various ranges as a matrix z(x,y), where the (x,y) coordinates are related to the pixel numbers. We can, however, not directly compare a 3-D target image z(x,y) at range r_1 to another image at range r_2. The latter could, e.g. exist in a mug shot archive of 3-D images taken at a few meters distance. Before comparison we must translate, scale and rotate the target image (x,y,z) coordinates such that it has the right size and orientation as those taken in the archive. This is done in the following way:

1. The images are rotated to face the front using the center of the 3-D target image as the point of rotation.
2. The translation is done by locating the nose in the 3-D target image which usually is the closest point. The image is now translated in (x,y) so that the nose is located in the center of the image.
3. The coordinates (x,y) are subsequently scaled up by a factor given by the ratio of the ranges r_1/r_2 .
4. Finally, a central area of the target with good SNR is used to determine the average range r_1 of the area. This range is then subtracted from the z values in all pixels.

The resulting target 3-D image, which we will denote $z_1(x,y)$, can now be compared to an image $z_2(x,y)$ in, e.g., a 3-D mug-shot archive. Alternatively, if one is searching for a particular suspect $z_2(x,y)$ in the archive and want to compare to a number of targets z_1 , it is faster to transform $z_2(x,y)$ once instead of all $z_1(x,y)$.

For a quantitative comparison we now define the RMS measure of two such 3-D images by

$$RMS(1,2) = \left\{ \frac{1}{N} \sum_{x,y}^{N} \left[z_1(x,y) - z_2(x,y) \right]^2 \right\}^{1/2} \tag{4}$$

Here, it is implicitly assumed that the coordinates of $z_1(x,y)$ and $z_2(x,y)$ are transformed properly to the same distance as described above. The sum is chosen to run over most of the pixels covering the face, however, not including dark areas of the image which generally has low SNR and thus poor range accuracy. N is the number of pixel summed over. Consequently, RMS is a root mean square of the differences in z-value between the two faces 1 and 2. Implicitly, it depends on the ranges r_1 and r_2 at which they are recorded.

If 1 and 2 are the same person the resulting RMS value reflects the uncertainty in range accuracy, Δz_{system}, at the two ranges. A typical example is shown in Fig. 5 where we take the 3-D images of Fig. 3 at various ranges and compare to a 3-D image of the same target taken in the lab at 6 m range. The RMS values are calculated from Eq. (4) and are seen to increase from Δz =1 mm to 5 mm at 500 m range due to turbulence, vibrations, camera drift, etc. as discussed above.

When 1 and 2 are two different persons the RMS reflects in addition to system noise, the biometric differences Δz_{face} in facial topology between 1 and 2 as

$$RMS(1,2) = \left\{\Delta z_{system}^2 + \Delta z_{face}^2\right\}^{1/2} \quad . \tag{5}$$

In Fig. 5 we have plotted the calculated RMS values vs. range r. As target 1 the images given in Figs. 3+4 as well as a third person have been used. As 2 an archive image of the same head used in Fig. 3 taken at 6 m has been used. Thus the archive image 2 is compared both to a series of images of the same person and to two series of images of different persons. As seen in Fig. 5. a large difference in RMS of >1cm is found when the target is different from the archive. In contrast a small difference of 1-5 mm is found when the target is the same as the archive. From this we can conclude that these images can be clearly discriminated at ranges up to at least 500 m.
In the case of look-a-likes or twins, of course Δz_{face} ~0, and the RMS method cannot discriminate.

Also shown in Fig. 5 are the RMS values vs. range for 3-D images of Fig. 4 compared to the head of a third person taken at 135 m. At this range the 3-D image $z_2(x,y)$ is somewhat smeared and for that reason the RMS values are slightly smaller.

We are currently building a database of 3-D images at a range of a few meters. For eye-safety reasons they are taken by stereoscopy or using structured white light. From this database we can calculate a large number of RMS values. The result will be a more quantitative PID depending on biometric differences and range. For a general survey of 3D face recognition see Ref.: [13].

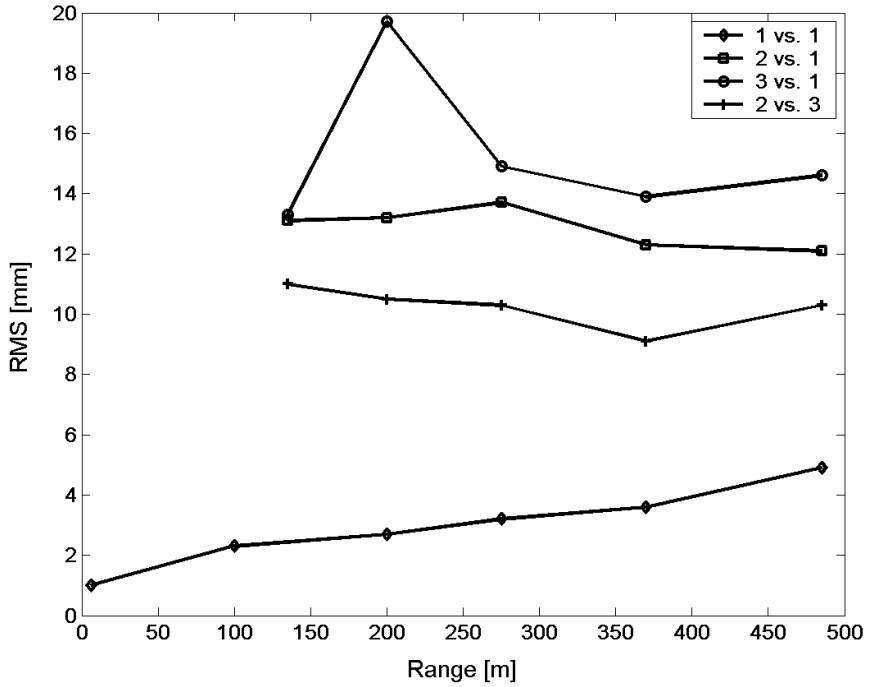

Fig. 5. Plot of measured RMS values vs. range r. Person 1 and 2 refer to the 3-D images of Figs. 3 and 4 respectively (see text). That the RMS is substantially smaller when comparing the same person (1 vs. 1, lower curve) supports the 3-D PID at ranges up to ~500 m.

5. PRECISION OF LASER RADAR GPS COORDINATES

The 14 inch astronomical telescope employed has the additional advantage that it can be controlled and steered by computer. Its orientation (inclination and declination angles) can thus be read-off once properly calibrated. Furthermore, our laser radar system determines the precise distance to the target. The target coordinates vector (x,y,z) between target and our laser radar system can then be calculated to an accuracy of a few cm for ranges up to several km. To calculate the corresponding GPS coordinates of the target we must add the GPS coordinates of our laser radar, which typically has an uncertainty of a few meters. Using differential GPS the accuracy can be reduced to about 1m, which then also will be the final uncertainty of the target coordinates.

The GPS coordinates of the target can then be transmitted along side the 3-D image to our high command in a few seconds. Conversely, if the GPS coordinates of a suspect target is received electronically, our prototype system can automatically orient the telescope to point at the target and set the camera delay and gate times in order to record a 3-D image within a few seconds.

6. SUMMARY AND OUTLOOK

It has been demonstrated that our laser radar system can take high accuracy 3-D images at long distances. The technology can be pressed to take 3-D images of relatively small objects as faces with down to an accuracy of 1 mm at ranges up to ~500 m with successful PID using only the 3-D

information. PID can be further improved by exploiting traditional methods utilizing the 2-D reflectivity images. For that purpose the 3-D method has the additional advantage that the objects can be rotated and the faces can be turned from angles between -90 and +90 degrees in all directions. Also the active imaging removes shadows.

The detector is sensitive into the red and near IR spectrum but not in IR at wavelengths above 800nm. By using a pulsed laser in the near IR as illumination, the system can therefore be made invisible and covert. Similar range accuracy is expected in near IR as in green.

Further improvements of the present prototype will be implemented and analyzed in the near future. These are camera upgrade to reduce trigger drift, additional optical zoom, stabilization of telescope and camera to reduce vibrations, and reduction of turbulence at the wide telescope aperture. Tests of turbulence effects at target, in the intermediate range, and at telescope aperture will be studied in future trials where the system also will be tested at longer distances.

REFERENCES

1. O. Steinvall, L. Klasen, C. Grönvall, U. Söderman, S. Ahlberg, Å. Person, M. Elmqvist, H. Larsson, D. Letalick, P. Andersson, T. Carlsson, and M. Henriksson, "3D laser sensing at FOI – overview and a system perspective", Proc. SPIE, **5412**, 294-309, 2004.
2. J. Busck and H. Heiselberg, "Gated viewing and high-accuracy three-dimensional laser radar," *Appl. Opt.*, **43**, 4705-4710, 2004.
3. J. Busck and H. Heiselberg, "High-accuracy three-dimensional laser radar," Proc. SPIE, **5412**, 257-263, 2004.
4. D. Gleckler, "Multiple-slit streak tube imaging lidar (MS-STIL) applications", Proc. SPIE, **4035**, 266-278, 2000.
5. J. W. McLean and J. T. Murray, "Streak-tube lidar allows 3-D ocean surveillance", *Laser Focus World*, 171-176, Jan. 1998.
6. A. Nevis, R. J. Hilton, S. J. Taylor, B. Cordes, and J. W. McLean, "The advantages of three-dimensional electro-optic imaging sensors", Proc. SPIE, **5089**, 225-237, 2003.
7. W. Schilling, D. N. Barr, G. C. Templeton, L. J. Mizerka, and C. W. Trussel, "Multiple-return laser radar for three-dimensional imaging through obscurations", *Appl. opt.*, **41**, 2791-2799, 2002.
8. M. A. Albota, R. M. Heinrichs, D. G. Kocher, D. G. Fouche, B. E. Player, M. E. O'Brien, B. F. Aull, J. J. Zayhowski, J. Mooney, B. C. Willard, and R. R. Carlson, "Three-dimensional imaging laser radar with a photon-counting avalanche photodiode array and microchip laser", *Appl. Opt.*, **41**, 7671-7678, 2002.
9. R. Lange and P. Seitz, "Seeing distances – a fast time-of-flight 3D camera", *Sensor Review*, **20**, 212-217, 2000.
10. K. Aliberti et al., "Characterizaton of InGaAs self-mixing detectors for chirp, amplitude-modulated LADAR, Proc. SPIE, **4377**, 99-110, 2001.
11. R. Stettner, H. Bailey, and R. Richmond, "Eye-safe laser radar 3-D imaging", Proc. SPIE, **5412**, 111-116, 2004.
12. G. S. Cheok and W. C. Stone, "Performance evaluation facility for LADARS", Proc. SPIE, **5412**, 54-65, 2004.
13. K. W. Bowyer, K. Chang, and P. Flynn, "A survey of approaches to three-dimensional face recognition", Proc. 17'th Int. Con. Pattern Recogn. (ICPR'04), IEEE, 2004